



TOR VERGATA
UNIVERSITÀ DEGLI STUDI DI ROMA

DOTTORATO DI RICERCA IN FISICA

CICLO DEL CORSO DI DOTTORATO XXXIII

**Search for the FCNC decay of top-quark in
c-quark and Z boson using the ATLAS detector**

LORENZO MARCOCCIA

A.A. 2020/2021

DOCENTE GUIDA: Prof. LUCIO CERRITO

COORDINATORE: Prof. ROBERTO BENZI

A dissertation submitted to the University of Rome Tor Vergata in accordance with the requirements of the degree of DOCTOR OF PHILOSOPHY in the Faculty of Physics.

32 NOVEMBER 2184

*'The wrong view of science
betrays itself in the craving to be right;
for it is not his possession of knowledge,
of irrefutable truth, that makes the man of science,
but his persistent and recklessly critical quest for truth.'*

(Karl Popper, The Logic of Scientific Discovery)

Ringraziamenti

Merci, merci, merci.

Abstract

Blablabla.

Contents

Abstract	iii
Contents	v
Introduction	1
1 The theory framework	3
1.1 The gauge principle in quantum field theory	3
1.1.1 Quantum Chromodynamics	5
1.1.2 The electro-weak sector	6
1.1.2.1 GIM mechanism	7
1.1.2.2 CKM matrix	8
1.2 Top quark physics	9
1.2.1 Production	9
1.2.2 Decay channels	10
1.3 Theories for physics beyond the Standard Model	11
1.3.1 Quark singlets	13
1.3.2 Two Higgs Doublet Model	13
1.3.3 Minimal Supersymmetric Standard Model	14
2 The LHC accelerator and the ATLAS experiment	16
2.1 The LHC accelerator	17
2.2 The ATLAS detector	21
2.2.1 Magnet System	22
2.2.2 Inner Detector	22
2.2.3 Calorimetric System	23
2.2.4 Muon Spectrometer	25
2.2.5 Trigger and Data Acquisition	27

3 The Trigger system upgrade for High-Luminosity LHC	28
3.1 ATLAS Barrel Muon Trigger	29
3.2 BI upgrade for Phase-II	32
3.2.1 RPC upgrade	35
3.2.2 Trigger scheme	37
3.3 Hit digitization in the BI region	39
3.3.1 The cluster size model	39
3.3.2 Timing	45
3.4 L0 barrel trigger efficiency	46
3.4.1 BM and BO retrofitting	47
3.4.2 Dropping BIR and BIM chambers	50
3.5 Summary and considerations	52
4 Data modeling and object reconstruction	53
4.1 Event simulation	53
4.2 Object reconstruction	55
4.2.1 Electrons	55
4.2.2 Muons	55
4.2.3 Soft muons	57
4.2.4 Jets	57
4.2.5 Soft Muon Tagging	57
4.2.6 Recurrent Deep-Learning DL1r	57
4.2.6.1 b -tagged jets	58
4.2.6.2 c -tagged jets	58
4.2.7 Missing transverse momentum	58
4.2.8 Overlap removal	58
5 Search for the FCNC decay of top-quark in c-quark and Z boson	59
5.1 Physics motivation	59
5.2 Analysis strategy	63
5.3 Data and Monte Carlo samples	64
5.3.1 Data sample	64
5.3.2 Monte Carlo simulated samples	65
5.3.2.1 Signal samples	65
5.3.2.2 Background samples	66
6 FCNC tZc with charm-tagging	70
6.1 Event selections and reconstruction	70
6.1.1 Top quarks reconstruction	71
6.1.2 Signal Region with SMT definition	72
6.1.3 Reconstruction of the soft muon decay chain	75
6.2 Background estimation	77
6.3 Separation of signal from background events	77
6.3.1 Input variables	77
6.3.2 GBDT training and evaluation	78
6.3.3 GBDT performance and overtraining checks	79
6.4 The alternative c-tagger DL1r _c	83

7 FCNC tZc with charm-tagging veto	86
7.1 Event selections and reconstruction	86
7.1.1 Top quarks reconstruction	87
7.1.2 SR1 selections	87
7.1.3 SR2 selections	87
7.1.4 Event yields in the Signal Regions	90
7.2 Background estimation	91
7.2.1 Control Regions definition	91
7.2.2 Event yields in the Control Regions	92
7.3 Separation of signal from background events	94
8 Statistical analysis for tZc coupling	95
8.1 Systematic uncertainties	95
8.1.1 Sources of systematic uncertainties	95
8.1.1.1 Object energy scale/resolution and efficiencies	95
8.1.1.2 Monte Carlo modelling	97
8.1.1.3 Background rate uncertainty	98
8.1.1.4 Luminosity and Pile-up reweighting	99
8.1.2 Acceptance and shape uncertainties	99
8.1.2.1 Symmetrization of shape uncertainties	99
8.1.2.2 Smoothing and Pruning	99
8.2 Strategy	100
8.3 Summary of fits	101
8.4 Signal + Background fit in SRs+CRs with realistic Asimov	102
8.5 Results	114
9 Conclusions	115
Appendix A Monte Carlo samples	116
Appendix B Mass Resolution	119
Appendix C Charm tagging using DL1r	121
Appendix D BDT optimization	123
D.1 Input variables	124
D.2 Hyper-parameters optimisation	130
Appendix E Kinematic distributions in the Signal Regions	131
E.1 SR1tZc	132
E.2 SR2tZc	134
E.3 SR3tZc	136
Appendix F Kinematic distributions in the Control Regions	138
F.1 tt CR	139
F.2 ttZ CR	141
F.3 Side-band CR1	143
F.4 Side-band CR2	145

CONTENTS

Appendix G Background only fit in CRs

147

References

155

Introduction

CONTENTS

CHAPTER 1

The theory framework

The construction of the Standard Model is the result of a long series of experiments and brilliant ideas in both theoretical and experimental fields. Towards the end of the 1960s, knowledge of what we consider to be the constituent elements of nature and the fundamental interactions among them, was organized in the so-called Standard Model (SM).

More recently, a missing piece towards the completion of the SM, the Higgs boson, was discovered by the ATLAS and CMS collaborations.

The ambition is to find a theoretical representation of all phenomena experimentally accessible. Since particle physics is characterized by phenomena that are both relativistic than quantistic, the description of the Standard Model relies on the formalism of *Quantum Field Theories* (QFT), synthesis of quantum mechanical and relativistic theory. In these terms, the concept of field is associated both to material particles and to forces. Particles are mere manifestations of fields: they are identified with the quanta of the material fields and force fields and the interaction among particles is determined by the exchange of virtual quanta of the field.

To search for extensions of the SM, it is possible to postulate a scale of the new physics high enough to manifest itself through deviations of known observables, usually at high energies.

In this chapter, a concise description of the SM will be presented, from the gauge principle to the description of several theories of physics beyond the Standard Model which are crucial for the search of FCNC decay of the top quark.

1.1 The gauge principle in quantum field theory

The mathematical framework of the SM is based on a quantum field theory description of the particles and their interactions. The structure is a consequence of the invariance of physics under certain general symmetries: these invariances are called *gauge* because there is freedom in the choice of a certain number of parameters that can precisely "calibrate" the model. Each symmetry

is therefore associated with a set of transformations that frame the "gauge group of the theory". The theory is introduced starting from the Lagrangian formalism developed in the classical mechanism, extending this formalism to classical field theory and finally to quantum field theory.

Lagrangian is defined as the difference between the kinetic energy and the potential energy of the system, as below:

$$\mathcal{L}(q, \dot{q}) = \frac{m}{2}(\dot{q})^2 - V(q) \quad (1.1)$$

where q is a set of generalized coordinates and m is the mass of the particle.

The *action* is defined as $S = \int dt \mathcal{L}(q, \dot{q})$.

Using a variational approach it can be shown that for any possible variation of the path of the particle, $\partial(q)$, the equation of motion of the system is the one that minimizes the *action*. The results are the so called *Euler-Lagrange* equations:

$$\frac{\partial \mathcal{L}}{\partial q} - \frac{d}{dt} \left(\frac{\partial \mathcal{L}}{\partial \dot{q}} \right) = 0 \quad (1.2)$$

The next step is the extension of the classical mechanics formalism to field theory. One possible way is to generalize the path of a particle which is a function of time $q(t)$, into a function of space-time coordinates $\phi(x)$ which is the vectorial (or tensorial) representation of the field with Lorentz invariance properties of the space-time.

The sub-set of dimension-four vectorial representations used in particle physics is called spinors and they can be decomposed into left-handed and right-handed components, depending on their chirality: ψ_L and ψ_R . The usual representation for Lorentz and parity transformations is the *Dirac* spinor $\Psi = (\psi_L, \psi_R)$, which allows describing properly the dynamics of relativistic particles.

At this point, the Lorentz-invariant Lagrangian is the following:

$$\mathcal{L}_D = \bar{\Psi}(i\gamma^\mu \partial_\mu - m)\Psi \quad (1.3)$$

where γ are an extension of the Pauli matrices into a four dimension space and they are called Dirac matrices.

The QFT is also built on the *Noether's* theorem that relates symmetries of the system to conserved observables.

Through this theorem, symmetries become a fundamental building block of the physical theory. A particular set of transformations, called gauge transformations, which by construction leave invariant the Lagrangian of the SM, constitute a building principle of the SM itself.

Let us now consider the global $U(1)^1$ transformation of the form:

$$\Psi \rightarrow e^{i\theta}\Psi \quad (1.4)$$

It can be easily demonstrated that \mathcal{L}_D is invariant under such a transformation and the related conserved observable is the current $\bar{\Psi}\gamma^\mu\Psi$.

¹ $U(1)$ is the one-dimensional unitary group, i.e. any of its elements can be expressed as a 1×1 matrix whose inverse is equal to its transpose conjugate ($U^{-1} = \bar{U}^*$).

However, the Lagrangian is no longer invariant under the transformation: $\theta \rightarrow \theta(x)$ which means that the gauge invariance is required in each point of the space-time.

The inclusion of an additional field, the photon, which mediates the forces, makes the Lagrangian explicitly invariant and it allows to choose a *gauge* of the theory, in fact the action of free electromagnetic field is invariant under $A_\mu \rightarrow A_\mu - \partial_\mu \theta$, with A_μ being the four-vector of the electrostatic and magnetic potential: (V, \vec{A}) .

The above example is useful to understand how the SM is constructed. It is a gauge theory which, analogously to what described in this section, is invariant under:

$$SU(3)_c \otimes SU(2)_L \otimes U(1)_Y \quad (1.5)$$

The $SU(3)_c$ describes the strong force (see next section) while $SU(2)_L \otimes U(1)_Y$ term describes the electro-weak sector (see Section 1.1.2). A more detailed discussion follows.

1.1.1 Quantum Chromodynamics

The strong interaction between quark and gluons is described by the *Quantum Chromodynamics* (QCD). It is a gauge theory based on non-abelian $SU(3)_c$ ² and associated to the three colour charges (red, green and blue). A total number of 8 generators T^a of the group, also called Gell-Mann matrices, represent bosons mediating the force, called *gluons*. They are massless, in contrast with the weak mediators.

The QCD Lagrangian, can be expressed as:

$$\mathcal{L}_{QCD} = \bar{\psi}(i\gamma^\mu D_\mu - m)\psi - \frac{1}{4}G_{\mu\nu}^a G_a^{\mu\nu} \quad (1.6)$$

where the index a represents the 8 $SU(3)_C$ generators, $\frac{1}{4}G_{\mu\nu}^a G_a^{\mu\nu}$ is the kinetic term of the gluons (G^a is the gluon field strength tensor) and the covariant derivative D_μ is defined as

$$D_\mu = \partial_\mu - ig_s T_a G_\mu^a \quad (1.7)$$

The coupling constant α_s ($\frac{g_s^2}{4\pi} \sim 1$), is dependent on the transferred momentum Q^2 that corresponds to a dependence on the separation between quarks:

$$\alpha_s(Q^2) = \frac{33 - 2n_f}{12\pi} \ln \left(\frac{Q^2}{\Lambda_{QCD}^2} \right) \quad (1.8)$$

where n_f is the number of quark flavours and Λ_{QCD}^2 is the QCD scale parameter, measured to be ~ 200 MeV that sets the scale between different regimes of the theory.

In fact one can discern two cases:

$$\alpha_s(Q^2) \xrightarrow[Q^2 \gg \Lambda_{QCD}^2]{} 0$$

²S stands for "special", meaning that the group matrices have determinant 1. C stands for "colour", which is the conserved quantity associated with the symmetry

$$\alpha_s(Q^2) \xrightarrow[Q^2 \ll \Lambda_{QCD}^2]{} \infty$$

In the first case, the quark coupling is asymptotically cancelled, in the limit $Q^2 \rightarrow \infty$, quarks can be considered as free particles and this phenomena is called *Asymptotic Freedom*. On the contrary, when the separation becomes relevant, the coupling is so strong to confine quarks in hadronic structures and this different phenomena is called *Confinement*. The only bound states that occur are completely antisymmetric in the colour variables (the colour singlets), which is equivalent to saying that the possible compositions of quarks must be "white".

Interaction between particles that carry charges of colour, takes place through the exchange of gluons of the octet, therefore, not only between quarks and gluons but also between gluons and gluons. This is a very important difference between QED (*Quantum Electrodynamics*) and QCD. In QED, in fact, photons have no charge and cannot couple with each other.

1.1.2 The electro-weak sector

The first model of the weak interaction was proposed by Fermi in 1933, who proposed an effective field theory at low energies. According to this theory, charged current interactions are approximated by a point-like interaction with a coupling called G_F [1, 2]. At energies $\mathcal{O}(100 \text{ GeV})$ the theory breaks and the real propagator of the interaction is the W^\pm boson.

In 1957, a famous experiment conducted by Wu [3] proved that parity is maximally violated by the charged weak interaction: it only couples to particles of left-handed chirality (and antiparticles of right-handed chirality). There also exists a neutral weak interaction, which couples both to left-handed and right-handed particles.

This discovery motivated the introduction of the vector-axial (V-A) structure of the Lagrangian of the weak force.

The model of the weak interaction was subsequently promoted to a gauge theory by requiring local invariance under symmetries of the $SU(2)$ group, and it was associated with a conserved quantity called the *weak isospin*.

Each generation of left-handed fermions forms a doublet satisfying $I_3 = \pm \frac{1}{2}$, while right-handed fermions correspond to singlets of null isospin, as follows:

$$\chi_L = \begin{pmatrix} \nu_l \\ l \end{pmatrix}_L \quad l_R \quad (1.9)$$

where $l = (e, \mu, \tau)$, and a right-handed neutrino singlet is not introduced since there is still no observation of such a particle. A similar representation is given for quarks where both up (u, s, t) and down-types (d, c, b) have a right-handed component, singlet under $SU(2)_L$.

The transitions between quark doublet members corresponds to $SU(2)$ raising (τ^+) and lowering (τ^-) operators, giving the charge raising and lowering currents [4]:

$$J^+ \sim g(\bar{u} d_c) = g(\bar{u} \bar{d}_c) \begin{pmatrix} 0 & 1 \\ 0 & 0 \end{pmatrix} \begin{pmatrix} u \\ d_c \end{pmatrix} = g(\bar{q} \tau^+ q) \quad (1.10)$$

$$J^- \sim g(\bar{d}_c u) = g(\bar{u} \bar{d}_c) \begin{pmatrix} 0 & 0 \\ 1 & 0 \end{pmatrix} \begin{pmatrix} u \\ d_c \end{pmatrix} = g(\bar{q} \tau^- q)$$

where overall numerical factors have been omitted, d-quark is 'Cabibbo-rotated' ($\theta_c \sim 13^\circ$) and g is the dimensionless weak coupling constant and quarks.

If there exist an appropriate symmetry, based on some underlying gauge theory, then a current involving τ_3 is also expected, since these operators are related via the commutation relation $[\tau^+, \tau^-] = 2\tau_3$. Hence, with such a gauge theory symmetry, one would expect the existence of a neutral current (identified by the Z^0 boson) of the form :

$$\begin{aligned} J^0 &\sim 2g(\bar{q}\tau_3q) = g(\bar{u}u - \bar{d}_c d_c) \\ &= g[\bar{u}u - \bar{d}_c d \cos^2 \theta_c - \bar{s}_c s \sin^2 \theta_c - (\bar{d}s + \bar{s}d) \cos \theta_c \sin \theta_c] \end{aligned} \quad (1.11)$$

The terms $\bar{d}s$ and $\bar{s}d$ correspond to strangeness-changing neutral currents (SCNC), which are heavily suppressed in nature.

For example, the decay branching ratio $K^+ \rightarrow \mu^+ \nu_\mu$ is 63.5%, whereas that for $K_L^0 \rightarrow \mu^+ \mu^-$ is $\sim 10^{-8}$.

A mechanism to suppress this unwanted strangeness-changing neutral currents was suggested in 1970 by Glashow, Iliopoulos and Maiani (GIM) and it will be described in the next section.

1.1.2.1 GIM mechanism

Until the beginning of the 1970s, the only three light quarks u, d and s known at this time could explain the observed hadron spectrum, and the observed weak decays of pions and kaons were mostly in good agreement with the predictions of the *Cabibbo mechanism*. Glashow, Iliopoulos and Maiani proposed the existence of a second orthogonal doublet, additional to $(\frac{u}{d_c})$, containing a new quark c (charm) with charge $\frac{2}{3}$, as follows [5]:

$$q' = \begin{pmatrix} c \\ s_c \end{pmatrix} = \begin{pmatrix} c \\ -d \sin \theta_c + s \cos \theta_c \end{pmatrix} \quad (1.12)$$

Adding this term gives the total neutral current:

$$\begin{aligned} J^0 &\sim 2g(\bar{q}\tau_3q + \bar{q}'\tau_3q') = g(\bar{u}u + \bar{c}c - \bar{d}_c d_c - \bar{s}_c s_c) \\ &= g[\bar{u}u + \bar{c}c - \bar{d}d - \bar{s}s] \end{aligned} \quad (1.13)$$

That is, the unwanted terms cancel, leaving a flavour diagonal result.

The GIM mechanism gives also the prediction of the charmed quark, before the J/Ψ discovery occurred in 1974.

In the three-quarks picture, and according to the Cabibbo mechanism alone, $s \rightarrow d$ transitions via *Flavour Changing Neutral Current* FCNC processes would be possible at all orders of the perturbation expansion.

For example, the process $K_L^0 \rightarrow \mu^+ \mu^-$ FCNC decay could take place, in terms of known quark (u and d-quarks), via the "box-diagram" of Figure 1.1(a).

The calculated rate is larger than what was observed experimentally.

However, including the diagram of Figure 1.1(b), the total amplitude is:

$$\mathcal{M} = \mathcal{M}_{(a)} + \mathcal{M}_{(b)} \sim f(m_u)g^4 \cos \theta_c \sin \theta_c - f(m_c)g^4 \cos \theta_c \sin \theta_c \quad (1.14)$$

Thus, the c-quark induces a cancellation, giving a BR compatible with the experiments, but not a total cancellation because $m_c \neq m_u$. Hence, the prediction on the mass of the c-quark that in the end is ~ 3 GeV. In addition to this major prediction, the GIM mechanism led to the prediction



Figure 1.1 – Feynman diagrams of $K_L^0 \rightarrow \mu^+ \mu^-$ via (a) u-quark exchange and (b) c-quark exchange

that FCNC processes are forbidden at tree-level Leading Order. The branching ratios of several FCNC decays of the top quark in the SM are given in Table 1.1. The FCNC production is also

	$t \rightarrow uZ$	$t \rightarrow c\bar{Z}$	$t \rightarrow u\gamma$	$t \rightarrow c\gamma$	$t \rightarrow ug$	$t \rightarrow cg$	$t \rightarrow uH$	$t \rightarrow cH$
BR	8×10^{-17}	1×10^{-14}	3.7×10^{-16}	4.6×10^{-14}	3.7×10^{-14}	4.6×10^{-12}	2×10^{-17}	3×10^{-15}

Table 1.1 – Branching ratios for top quark FCNC interactions in the SM [6].

sensitive to numerous new physics models, as is mentioned in more details in Section 1.3. The GIM hypothesis represents a generalization of Cabibbo’s idea. The introduction of the fourth quark (c) restored the symmetry in the (then known) numbers of quark and leptons. These ideas were extended by Kobayashi and Maskawa (1973), who introduced a framework of six quarks and it will be described in the next section.

1.1.2.2 CKM matrix

In 1973 Kobayashi and Maskawa extended the Cabibbo’s mechanism allowing to describe the transitions within and in-between 3 generations of quarks using the so-called CKM 3×3 matrix [7, 8], which relates the weak eigenstate of down-type to their mass eigenstate:

$$\begin{pmatrix} d' \\ s' \\ b' \end{pmatrix} = V_{CKM} \begin{pmatrix} d \\ s \\ b \end{pmatrix} = \begin{pmatrix} |V_{ud}| & |V_{us}| & |V_{ub}| \\ |V_{cd}| & |V_{cs}| & |V_{cb}| \\ |V_{td}| & |V_{ts}| & |V_{tb}| \end{pmatrix} \begin{pmatrix} d \\ s \\ b \end{pmatrix} \quad (1.15)$$

By convention, the up-type quarks are taken to be pure states. Therefore, partners of the up-type quarks within the weak isospin doublets are the weak eigenstates d' , s' and b' which are the pure states.

The CKM matrix is fully defined by 4 independent parameters, which must be determined experimentally. These parameters are: 3 mixing angles and 1 CP-mixing phase, which violates the CP³ symmetry in the SM [9]. The diagonal elements of the CKM matrix are close to 1, reflecting

the fact that transitions are favoured between quarks of the same generation. The CKM matrix is unitary, i.e. the sum of the transition probabilities for any quark flavour is equal to 1. If this assumption was to be disproved, it could imply the existence of a fourth quark generation.

1.2 Top quark physics

The heaviest known elementary particle described by the Standard Model is the top quark. In 1995, the top quark discovery at FERMILAB [10, 11] was a great success for the SM predictions e.g. the corroboration of existence of a weak isospin partner of the top quark. Due to its large mass, the predicted lifetime $\tau_t \approx 5 \times 10^{-25}$ s (in agreement with theoretical expectations [12]) entail that it decays before hadronising.

In the next sections, the production mechanism is reported, as well as an overview of the decay channels.

1.2.1 Production

The top quark can either be produced as pairs, via strong interaction, or as a single top quark via electroweak interaction that does not preserve the flavour.

The main parton sub-processes that lead to top-pair production are the quark-antiquark annihilation ($q\bar{q} \rightarrow t\bar{t}$, Figure 1.2(a)) and the gluon-gluon fusion ($gg \rightarrow t\bar{t}$, Figures 1.2(b) and 1.2(c)).

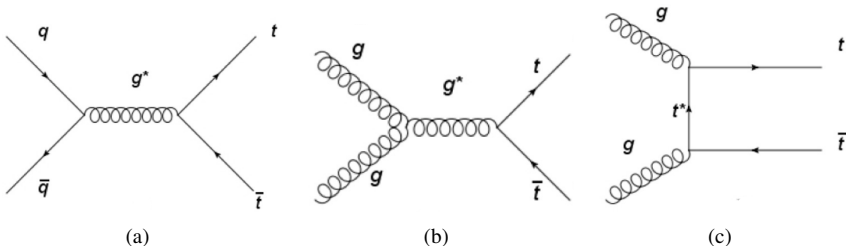


Figure 1.2 – Feynman diagrams of $t\bar{t}$ production via (a) quark-antiquark annihilation ($q\bar{q} \rightarrow t\bar{t}$), (b) and (c) gluon-gluon fusion ($gg \rightarrow t\bar{t}$)

Since in protons there are no valence antiquarks, the quark-antiquark annihilation is suppressed by the parton distribution functions (PDF) of the antiquark in the proton. Therefore, at the LHC the dominant process turns out to be the gluon-gluon fusion, while in a proton-antiproton collider, such as Tevatron, the dominant process is the quark-antiquark annihilation, in fact:

- Tevatron: $q\bar{q} \rightarrow t\bar{t} \approx 86\%$, $gg \rightarrow t\bar{t} \approx 15\%$
- LHC: $q\bar{q} \rightarrow t\bar{t} \approx 20\%$, $gg \rightarrow t\bar{t} \approx 80\%$

³Charge transformation followed by a parity transformation.

Top-pairs can be produced also by the weak interaction when two quarks exchange Z^0 or a γ ; however the cross-section of these type of processes is negligible when compared to the production cross-section through strong interaction.

Although at the LHC the top quarks are mainly produced in the process described above, a not negligible number of tops are produced singly by weak interaction. The production cross section, in this case, is equal to approximately 1/3 of the top-pair production cross-section, which is $\sigma_{t\bar{t}} = 831.8^{+19.8+35.1}_{-29.2-35.1} \text{ pb}$ [13], at $\sqrt{13} \text{ TeV}$ and taking into account a top quark mass of 172.5 GeV.

1.2.2 Decay channels

Since the top quark mass is larger than the W boson mass, the top decays through the weak interaction, mainly in to $t \rightarrow W^+ b$; according to the SM in 100% of the possible cases.

The other channels ($t \rightarrow W^+ s$, $t \rightarrow W^+ d$) are strongly suppressed by the CKM matrix elements (see Section 1.1.2.2). Exploiting the matrix unitarity and the B meson oscillation measurements, it is possible to extract the following BRs[14]:

$$\begin{aligned}\text{BR}(t \rightarrow W^+ b) &\sim 0.998 \\ \text{BR}(t \rightarrow W^+ s) &\sim 1.9 \cdot 10^{-3} \\ \text{BR}(t \rightarrow W^+ d) &\sim 10^{-4}\end{aligned}$$

Therefore, the top decay total width is given by, in good approximation, the decay ($t \rightarrow W^+ b$), thus equals to $\Gamma_t = 1.44 \text{ GeV}$. The W boson may decay in only two ways: "leptonically" ($W \rightarrow l\nu$) or "hadronically" ($W \rightarrow q\bar{q}'$). This leads to three different categories of $t\bar{t}$ decays: dileptonic, semi-leptonic or hadronic.

Figure 1.3 summarizes the BRs associated to each channel.

At hadron colliders, the dominant hadronic mode is the most difficult to isolate due to the large QCD background.

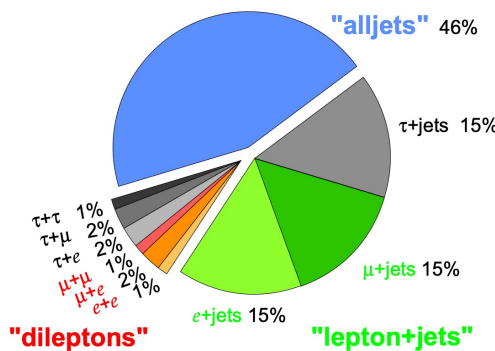


Figure 1.3 – Branching ratios associated to each $t\bar{t}$ decay channel [15].

1.3 Theories for physics beyond the Standard Model

The previous sections described the core components of what we call *Standard Model* and report few major successes of many. Its predictive power makes this model the most tested in physics and it reached the culmination of success on 4 July 2012, when the ATLAS and CMS experiments at CERN announced the observation a new particle in the mass region around 125 GeV, the Higgs boson [16].

But in spite of its important achievements, the SM falls short of explaining several important observations that in this section are briefly reported.

- The SM considers neutrinos as massless particles but this is in contradiction with the results of many experiments, which observed, in several different contexts, the *neutrino oscillations*.

It is a quantum mechanical phenomenon whereby a neutrino created with a specific lepton family number (e , μ , or τ) can later be measured to have a different lepton family number and this mechanism, implies that the neutrino has a non-zero mass since it arises from mixing between the flavour and mass eigenstates of neutrinos.

- The SM can not describe *dark matter* and *dark energy*. The first evidence of dark matter came with the observation of the rotational speed of galaxies, which suggests the existence of a huge amount of undetected mass [17].

None of the SM particles could explain this phenomenon and, since a dark matter has never been directly observed, implies that it interacts only weakly with the ordinary matter and radiation, or does not interact at all.

Likewise, dark energy is an unknown form of energy that affects the universe on the largest scales. The first observational evidence for its existence came from supernovae measurements, which showed that the universe does not expand at a constant rate; rather, the expansion of the universe is accelerating.

The data collected by the Planck spacecraft, indicate that dark energy contributes 68% of the total energy in the present-day observable universe. The mass–energy of dark matter and ordinary (baryonic) matter contributes 27% and 5%, respectively, and other components such as neutrinos and photons contribute a very small amount [18].

- After the Big Bang one could expect that the universe produced the same amount of particles-antiparticles and that the constant annihilation of pairs would have resulted in a universe of radiation. What we observe actually is large cosmological matter (but not antimatter) structures. The mechanism suggested by the SM through the CP-symmetry violation of neutral oscillating hadrons is not sufficient to explain alone this phenomenon.
- There are also other strong indications that the SM could be not yet complete. Indeed, it is based on 19 parameters (excluding neutrino masses) that must be determined experimentally and have no known theoretical origin. Moreover, gravity could not be included as a gauge theory because, describing graviton (the associated gauge boson) interactions, the classical theory of Feynman diagrams, and semiclassical corrections with at least two loops lead to *ultraviolet divergences*. These infinite results cannot be removed because quantized general relativity is not perturbatively renormalizable, unlike QED and models such as the Yang–Mills theory. Therefore, when the probability of a particle to emit or absorb gravitons is calculated, the theory loses predictive veracity. Those problems and the complementary approximation framework are grounds to show that a theory more unified than quantized general relativity is required to describe the behaviour near the Planck scale.

- The problem of *naturalness* is also much debated in literature. The Higgs boson is very sensitive to loop corrections and if one considers the theory close to the Planck scale, the corrections involving the top quark may not explain why the Higgs boson mass is so relatively small (~ 125 GeV). Another problem is, in fact, the mass scale of fermions that it ranges across many orders of magnitude without any clear explanation.

Many are models of "new physics" that attempt to describe and explain the phenomena mentioned above but so far there is no evidence of new physics Beyond Standard Model (BSM). In the SM, top quark decays almost exclusively into bW while flavour-changing neutral current (FCNC) decays such as $t \rightarrow qZ$ are forbidden at tree level. FCNC decays occur at one-loop level (Figure 1.4) but are strongly suppressed by the GIM mechanism (Section 1.1.2.1), with a suppression factor of 14 orders of magnitude relative to the dominant decay mode[19].

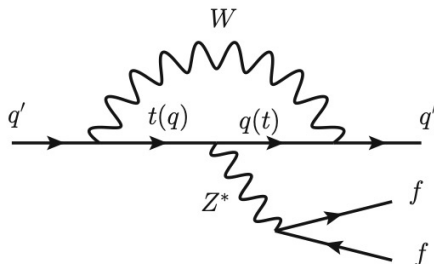


Figure 1.4 – Sketched Feynman diagram for SM $q' \rightarrow q'' f \bar{f}$ induced by the tqZ coupling, where q' and q'' denote the down-type quarks; $q = u, c$, and f can be any possible fermions. In the Standard Model, FCNC processes are forbidden at tree level but occur at one-loop level (see GIM mechanism in Section 1.1.2.1).

However, in the BSM models, the suppression could be relaxed and the loop diagrams mediated by new bosons that could contribute, leading to couplings of many orders of magnitude higher than those expected by the SM.

Examples of such extensions are the quark-singlet model (QS)[20], the two-Higgs-doublet model with (FC 2HDM) or without (2HDM) flavour conservation[21], the Minimal Supersymmetric Standard Model (MSSM)[22], the MSSM with R-parity violation (RPV SUSY)[23], models with warped extra dimensions (RS)[24], or extended mirror fermion models (EMF) [25]. Reference [26] gives a comprehensive review of the various extensions of the SM that have been proposed. Table 1.2 provides the maximum values for the branching ratios predicted by these models and compares them to the value predicted by the SM.

In this section we will briefly describe some of these theories interesting for the topics of this thesis.

Model:	SM	QS	2HDM	FC 2HDM	MSSM	RPV SUSY	RS	EMF
$\mathcal{B}(t \rightarrow qZ)$	10^{-14}	10^{-4}	10^{-6}	10^{-10}	10^{-7}	10^{-6}	10^{-5}	10^{-6}

Table 1.2 – Maximum allowed FCNC $t \rightarrow qZ$, ($q = u, c$) branching ratios predicted by several models[19–26].

1.3.1 Quark singlets

The need to suppress the FCNC mechanism lead to:

- they are not mediated by Z^0 boson at tree-level
- no FCNC mechanism in the scalar sector at tree-level

It is possible to overcome these dogmas using extensions of the SM, like the Quark Singlets (QS) [27] that introduces a vector-like quark ($Q = \frac{1}{3}$ or $Q = \frac{2}{3}$), thus a small violation of the $3 \times 3 V_{CKM}$ unitarity (see Section 1.1.2.2), mediated by Z^0 boson and natural FCNC suppression at tree-level.

Given x_L and x_R , $SU(2)_L$ singlets

$$\begin{pmatrix} d' \\ s' \\ b' \\ x' \end{pmatrix} = \begin{pmatrix} |V_{ud}| & |V_{us}| & |V_{ub}| & |V_{ux}| \\ |V_{cd}| & |V_{cs}| & |V_{cb}| & |V_{cx}| \\ |V_{td}| & |V_{ts}| & |V_{tb}| & |V_{tx}| \end{pmatrix} \begin{pmatrix} d \\ s \\ b \\ x \end{pmatrix}, \quad (1.16)$$

the non orthogonality of the columns leads to terms of the type:

$$J_\mu = \frac{g}{\cos\theta_W} Z_{bd} \bar{b}_L \gamma_\mu d_L Z^\mu \quad (1.17)$$

where

$$Z_{bd} = V_{ud} V_{ub}^* + V_{cd} V_{cb}^* + V_{td} V_{tb}^* \quad (1.18)$$

and Z_{bd} is suppressed by $\frac{m_q}{m_x}$.

In this way it is possible to have deviations from 3×3 unitarity.

For instance, the PMNS matrix in the leptonic sector, in the context of the see-saw mechanism is not 3×3 unitarity [28].

Vector-like quarks provide the simplest model with spontaneous *CP violation* and a framework to have a common origin of all CP violation, because it is a potential solution of the *strong CP problem*.

1.3.2 Two Higgs Doublet Model

The LHC discovery of a Standard-Model-like Higgs $H(125)$ particle in 2012[16] could be a portal to an extended Higgs sector predicted by several models. One of such models is the Two-Higgs-Doublet Model (2HDM) [29]. The most natural extension of the Standard Model scalar sector is the addition of an extra $SU(2)_L$ doublet.

The 2HDM is an *Effective Field Theory* (EFT)⁴ consisting of two complex Higgs doublets, which provide masses to both the up-type and the down-type fermions:

$$\Phi_1 = \begin{pmatrix} \phi_1^+ \\ \phi_1^0 \\ \phi_1^- \end{pmatrix} \quad \Phi_2 = \begin{pmatrix} \phi_2^+ \\ \phi_2^0 \\ \phi_2^- \end{pmatrix} \quad (1.19)$$

⁴An EFT corresponds to a low-energy approximation to a more fundamental underlying theory, characterized by an energy scale Λ (e.g. the mass of new particles)

with the minimum of the potential corresponding to

$$\Phi_{1,0} = \frac{1}{\sqrt{2}} \begin{pmatrix} 0 \\ \nu_1 \end{pmatrix} \quad \Phi_{2,0} = \frac{1}{\sqrt{2}} \begin{pmatrix} 0 \\ \nu_2 \end{pmatrix}. \quad (1.20)$$

After the electroweak symmetry breaking (EWSB), there are five physical scalar fields, consisting of neutral bosons h, H, A of which the first two bosons are CP-even, as opposed to the A -boson which is CP-odd and of two charged Higgs states H^\pm .

The model is parametrized by the five Higgs masses (m_H, m_h, m_{H^\pm}, m_A), the ratio of the vacuum expectation values of the two Higgs doublets $\tan \beta = \nu_2/\nu_1$ and the mixing angle α between the CP-even Higgs states.

There exist four types of 2HDM which simultaneously forbid the presence of FCNC and preserve CP symmetry:

- in Type I all fermions couple to the second doublet Φ_2 . It follows that BR are independent of $\tan \beta$;
- in Type II or MSSM-like scenario, lepton and down-type quarks couple to the first doublet Φ_1 , whilst up-type quarks couple to Φ_2 ;
- in Type III or lepton specific scenario, quarks couple to Φ_2 while leptons couple to the other doublet;
- in Type IV or flipped model, the coupling of the leptons is reversed with respect to the Type-II model.

1.3.3 Minimal Supersymmetric Standard Model

The FCNC processes have also been studied within the *Minimal Supersymmetric Standard Model* (MSSM), where there are loop corrections of the supersymmetric QCD with gluinos and scalar quarks, as shown in Figure 1.5. In supersymmetric QCD it was shown that there occurs flavour-changing strong interactions between the gluino, the left-handed quarks, and their supersymmetric scalar partners, whereas the couplings of the gluino to the right-handed quarks and their partners remains flavour diagonal. To calculate the one-loop diagrams shown in Figure 1.5, we need the couplings of the gluon to the gluinos, of the scalar partners of the left-handed quarks to the gluon, photon, and Z boson, and of the gluino to the left-handed quark and its scalar partner.

After the introduction of non-trivial squark mixing, it is possible to calculate the coupling that leads to flavour changing in which appears K_{ij} , the supersymmetric version of V_{CKM} :

$$\begin{pmatrix} 1 & \epsilon & \epsilon^2 \\ -\epsilon & 1 & \epsilon \\ -\epsilon^2 & -\epsilon & 1 \end{pmatrix}. \quad (1.21)$$

It is possible to demonstrate that all divergent terms cancel exactly, without the GIM mechanism. Finally, we define $\mathcal{B}(t \rightarrow cZ) = \frac{\Gamma_S(t \rightarrow cZ)}{\Gamma_W(t \rightarrow bW)}$, where:

$$\Gamma_W(t \rightarrow bW) = \frac{\alpha}{16 \sin \Theta_W} m_{top} \left(1 - \frac{m_W^2}{m_{top}^2} \right)^2 \left(2 + \frac{m_{top}^2}{m_W^2} \right) \quad (1.22)$$

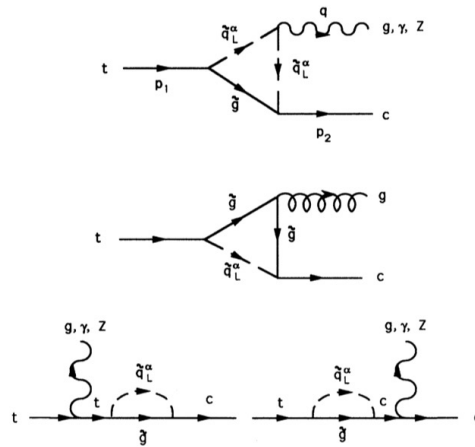


Figure 1.5 – The diagrams with scalar quarks and gluinos within the loop, which contribute to the top quark decay into a charm quark and a Z boson, photon, or gluon[30].

Using the following values for the parameters $m_{top} = 174$ GeV, $\alpha_s = 1.4675 / \ln \left(\frac{m_{top}^2}{\Lambda_{QCD}^2} \right)$ with $\Lambda_{QCD} = 0.18$ GeV, it is possible to derive the branching ratio $\mathcal{B}(t \rightarrow cZ)$ as a function of the scalar mass m_S for a gluino mass of 100 GeV (Figure 1.6).

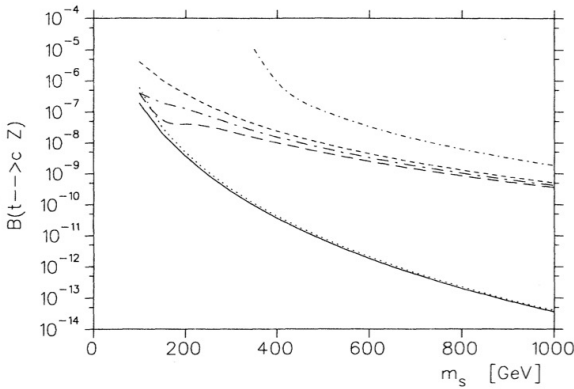


Figure 1.6 – The branching ratio $\mathcal{B}(t \rightarrow cZ)$ as a function of the scalar mass m_S . The gluino mass was taken to be 100 GeV. The solid line is the unphysical case with no squark mixing, the dotted lines are different scenarios of squark mixing[30].

We see that without mixing, $\mathcal{B}(t \rightarrow cZ)$ decreases rapidly with increasing scalar mass. The mixing has a drastic effect. It enhances the branching ratio by up to 5 orders of magnitude for large m_S .

CHAPTER 2

The LHC accelerator and the ATLAS experiment



Figure 2.1 – The LHC ring, aerial view.

This chapter main focus is the experimental setup, thus the ATLAS detector, one of the four large experiments at CERN (*Conseil Européen pour la Recherche Nucléaire*) and whose location is shown in Figure 2.1.

Established in 1954, CERN is the largest particle physics laboratory in the world and the organization is based in a north-west suburb of Geneva on the Franco-Swiss border. The analysis presented in this thesis is based on the data collected in Run2 (2015-2018). Since December 2018, LHC has been shut-down (LS2, 2019-2020) to undergo a major upgrade (Phase I Upgrade) which may enable to collect up to 300 fb^{-1} at a c.o.m. energy of 14 TeV by 2023. After that, a second major upgrade (Phase II Upgrade) is planned to the LHC (LS3, 2024-2025) which will increase the interaction rate by a factor of 10; this upgrade will lead LHC to High-Luminosity LHC (HL-LHC).

2.1 The LHC accelerator

Located at CERN, the Large Hadron Collider (LHC) [31] is the world's highest energy particle accelerator. LHC is a circular hadron accelerator, positioned at a depth of about 100 m in the tunnel built for the LEP accelerator. It is 26.6 km long and currently operates by making proton beams collide at an energy $\sqrt{s} = 13$ TeV. The overall accelerator complex is shown in Figure 2.2.

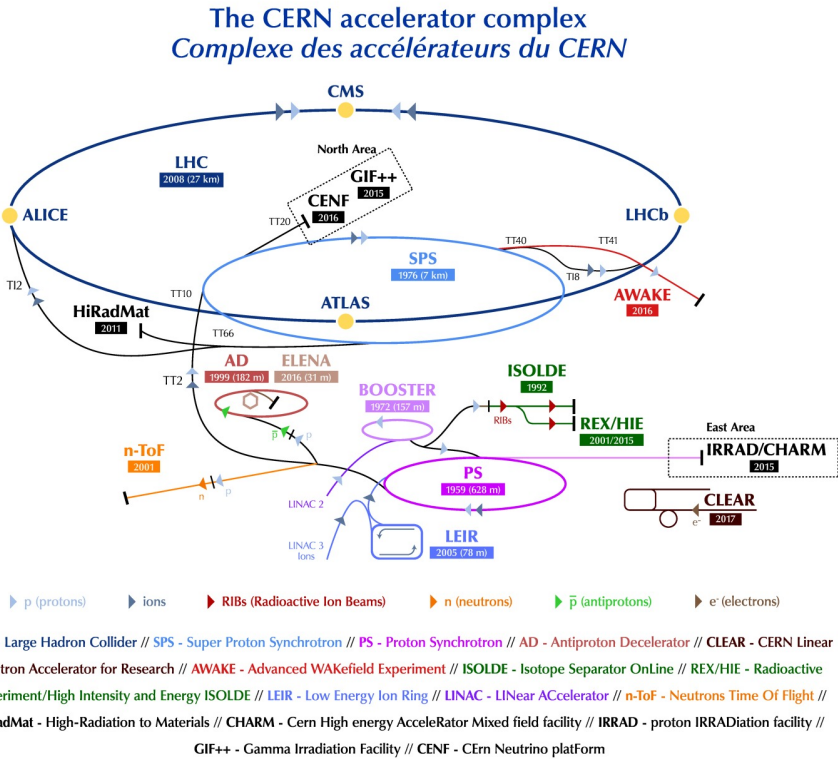


Figure 2.2 – The overall CERN accelerator complex [32].

CERN's choice to replace the LEP leptonic collider with an hadronic one, such as LHC, has brought two fundamental advantages: the first is that for the same infrastructural size it is possible to reach a higher energy in the center of mass, since the energy lost by radiation of synchrotron from a particle in circular motion is $\frac{dE}{dt} \propto \frac{E^4}{m^4 R}$, where R is the bending radius and m is the mass of the accelerated particle travelling at an energy E , hence protons are better than electrons. The second advantage is that the composite structure of the protons allows access to a wider energy spectrum that can be explored simultaneously without having to change the beam parameters. On the other hand, the number of background events also increases. In addition to proton-proton ($p-p$)

p) collisions, the LHC can also collide heavy lead ions (Pb-Pb).

Before reaching the target energy, protons undergo subsequent acceleration steps.

The first step is the proton production from hydrogen gas, after which protons are accelerated up to 50 MeV at the LINear ACcelerator 2 (LINAC 2). These protons are then injected into the Proton Synchrotron Booster (PSB) where their energy reaches 1.8 GeV. The acceleration chain continues into the Proton Synchrotron (PS) which pushes the beam to 25 GeV. After that, the beam is injected into the Super Proton Synchrotron (SPS) where the protons are accelerated up to 450 GeV. Finally, the bunches of protons are injected in the LHC. A typical bunch train corresponds to 2808 bunches for each beam with 25 ns separation, and a bunch contains about 10^{11} protons colliding at a rate up to 40 MHz.

The LHC is designed to accelerate each beam at an energy of 7 TeV thanks to a complex system of dipole and higher order magnets but the LHC performance has not always been that of today. The first protons beams were circulated in the LHC on September 10th of 2008. From 2010 to 2012, the protons beams had an energy of 3.5 TeV. From 2012 to 2013, the energy reached was 4 TeV per beam. Following, the first shutdown, the LHC started to accelerate beams up to an energy of 6.5 TeV in April 5th of 2015.

Since protons are charged particles, a strong magnetic field, produced by 1232 superconducting electromagnets, curves the beams around the circular accelerator. To maintain the superconductivity properties, these magnets require a temperature of 1.9 K ($\approx 271.3^{\circ}\text{C}$). This temperature allows the dipole magnets to generate a magnetic field of 8 T. Besides the bending magnets, a total of 392 quadrupole magnets maintain the beams focused and 16 radio-frequency cavities accelerate particles and keep them in controlled bunches with a constant energy. Four main interaction points are used as collision points corresponding to the location of the four detectors: ALICE, ATLAS, CMS and LHCb.

The number of multiple interactions per bunch crossing is called *pile-up* and it is denoted by μ . Actually there are two different sources of pile-up:

- in-time pile-up occurs when multiple collisions take place in a single bunch crossing
- out-of-time pile-up is due to finite read-out time resolution of the detectors, often larger than 25 ns. In this case, the residual energy from a previous bunch crossing could potentially be associated to the following bunch crossing.

The distribution of $\langle \mu \rangle$ is shown in Figure 2.3, for the different data-taking periods. The average pile-up for 2015-2018 is $\langle \mu \rangle = 33.7$.

The event rate of a given process with cross section σ is given by $\frac{dN}{dt} = \mathcal{L}\sigma$, where \mathcal{L} is a characteristic of the accelerator, known as *instantaneous luminosity* and is given by:

$$\mathcal{L} = \frac{N_b^2 k_b f \gamma}{4\pi \sigma_x \sigma_y} F \quad (2.1)$$

where N_b^2 is the number of particles per bunch, k_b is the number of bunches, γ represents the relativistic gamma factor, f is the revolution frequency of the accelerator, σ_x and σ_y are the horizontal and vertical beam size, F is a geometrical correction factor from the crossing-angle of the two beams at the interaction point (IP).

Given a period of time T , one can define the *integrated luminosity* as $L = \int_0^T dt \mathcal{L}$ which is typically expressed in fb^{-1} (1 b = 10^{-28} m^2).

Figure 2.4 shows the total integrated luminosity over the full LHC data taking period at $\sqrt{s} = 13 \text{ TeV}$ and Table 2.1 summarizes the main design parameters of the LHC.

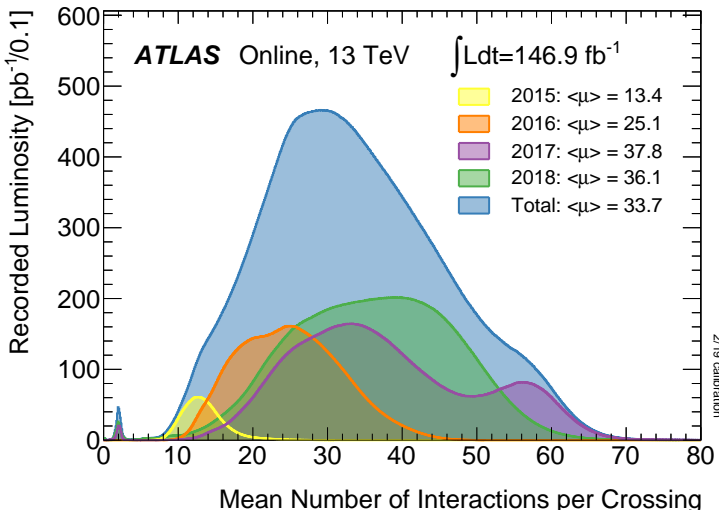


Figure 2.3 – Luminosity-weighted distribution of the mean number of interactions per crossing for the 2015–2018 pp collision data at $\sqrt{s} = 13$. All data recorded by ATLAS during stable beams is shown, and the integrated luminosity and the mean μ value are given in the figure [33].

Parameter	2015	2016	2017	2018
Bunch intensity [$\times 10^{11}$ p]	1.2	1.1	1.25	1.15
Number of bunches	2200	2200	1900	2500
Emittance [μm]	3.5	2.5	2.0	2.2
Crossing angle [μrad]	290	280	300	300
Peak luminosity [$10^{34}\text{cm}^2\text{s}^{-1}$]	0.5	1.5	1.5	2.0

Table 2.1 – Main beam parameters of proton-proton collisions of LHC in Run2.

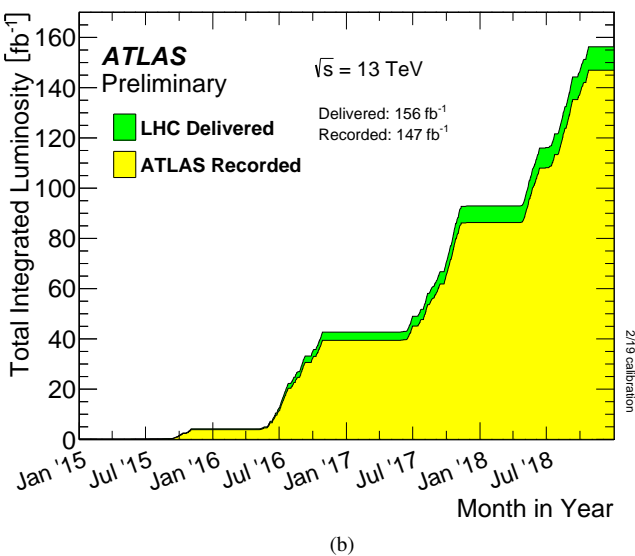
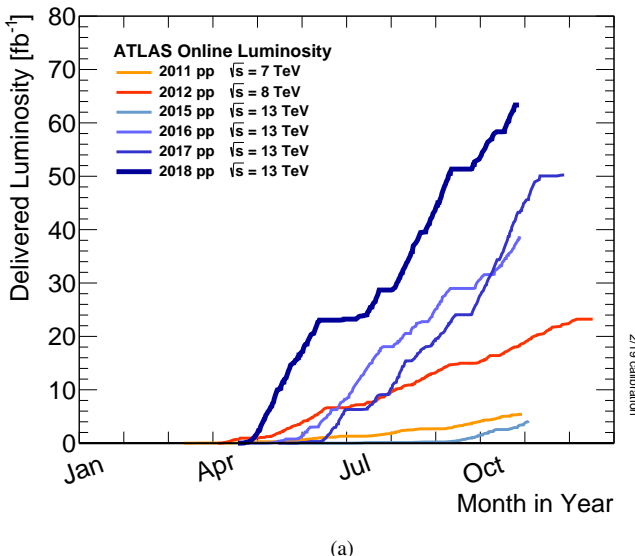


Figure 2.4 – Cumulative luminosity versus (a) day delivered to ATLAS during stable beams; (b) time delivered to ATLAS (green) and recorded by ATLAS (yellow) during stable beams for pp collisions at $\sqrt{13}$ [33].

2.2 The ATLAS detector

ATLAS (A Toroidal LHC ApparatuS) [34] is a multi-purpose apparatus whose primary goal is to identify and measure the properties of particles produced in p–p collision.

The overall ATLAS detector layout is shown in Figure 2.5. The ATLAS detector consist of a concentric cylinder shape (4π coverage), therefore nominally forward-backward symmetric with respect to the interaction point (IP) where the proton beams collide in it. It can be divided into five main parts:

- Magnet System (section 2.2.1);
- The Inner Detector (section 2.2.2);
- The Calorimetric System (section 2.2.3);
- Muon Spectrometer (section 2.2.4).
- Trigger and data acquisition System (section 2.2.5).

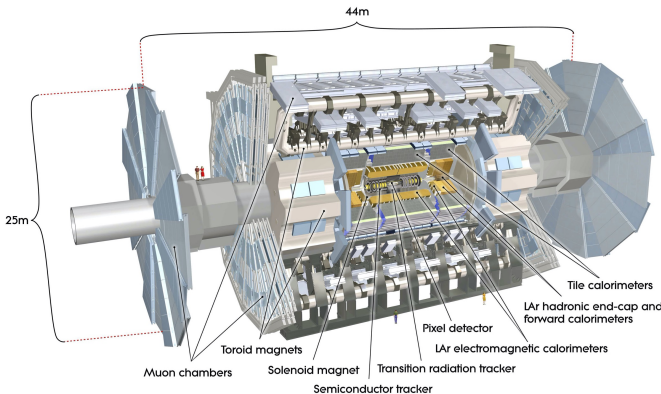


Figure 2.5 – Cut-away view of the ATLAS detector. The dimensions of the detector are 25 m in height and 44 m in length. The overall weight of the detector is approximately 7000 tonnes [34].

Coordinate system

The ATLAS coordinate system is a right-handed Cartesian coordinate system with the origin defined at the IP, in the center of the detector. The z -axis corresponds to the beam pipe while the x and y directions define the transverse plane.

A cylindrical coordinate system is often used due to the geometry of the detector, where ϕ is the azimuthal angle and θ is the polar angle. The ϕ is orthogonal to the beam direction, therefore it is invariant under a Lorentz boost(z -axis), while θ is not an invariant, so the *pseudorapidity* is defined as:

$$\eta = -\ln \left(\tan \left(\frac{\theta}{2} \right) \right) \quad (2.2)$$

Pseudorapidity is an approximation of the *rapidity*¹ for relativist particles ($m \ll p$) with mass m and momentum p .

The distance between two objects is indicated using ΔR , defined as:

$$\Delta R = \sqrt{\Delta\eta^2 + \Delta\phi^2} \quad (2.3)$$

The transverse momentum is the projection of the momentum orthogonal to the beam direction, defined as:

$$p_T = \sqrt{p_x^2 + p_y^2} \quad (2.4)$$

2.2.1 Magnet System

The magnet configuration comprises a thin superconducting solenoid surrounding the inner-detector cavity, and three large superconducting toroids (one barrel and two end-caps) arranged with an eight-fold azimuthal symmetry around the calorimeters. This fundamental choice has driven the design of the rest of the detector.

The inner detector is immersed in a 2 T solenoidal field provided by the central solenoid with inner radius of 1.23 m and a total length of 5.8 m.

It is designed to minimize the amount of material in front of the calorimeter to have a small impact on the energy measurement. This is achieved by hosting the solenoid and the cryostat in the same vacuum vessel of the electromagnetic calorimeter.

The overall dimensions of the magnet system is 26 m long and 20 m diameter and provide an average magnetic field intensity of 0.5 T in the barrel and 1 T in the end-caps regions [35].

2.2.2 Inner Detector

The Inner Detector (ID) [34] is the detector system closest to the beam.

It is composed of three detectors: the semiconductor pixel detector (PIXEL), the microstrip detector SCT (Semi-Conductor Tracker), and the most external, the transition radiation detector TRT (Transition Radiation Tracker). Its overall layout is depicted in Figure 2.6.

The ID is contained in a cylinder, 7 m long and 1.15 m in radius, placed in a 2 T solenoid magnetic field and it is designed to trace charged particles with a minimum moment of 0.1 GeV/c, it allows the measurement of the moment through the track curvature radius and the reconstruction of the main interaction and decay vertices (both primary and secondary).

The innermost part of the ID, which has a radius of about 15 cm, consists of silicon pixels to maximize the precision in the reconstruction of the tracks and the resistance to radiation. The pixel detector records on average three points for each track, which allows a reconstruction of the secondary decay vertices. This detector has a total of approximately 80 million sensitive elements.

The intermediate part, which covers a radius ranging from 30 to 60 cm, uses a microstrip detector (Semi-Conductor Tracker), to provide good spatial resolution. The detection technique of the SCT relies on the same principle as for the pixel detector, however long strips are used compared to the rectangular pixels due to the smaller particle density in the outer layers. It is located around the Pixel detector and is designed to provide eight precision measurements per track, contributing

¹Rapidity is defined as $y = \frac{1}{2} \ln \frac{E+p_z}{E-p_z}$

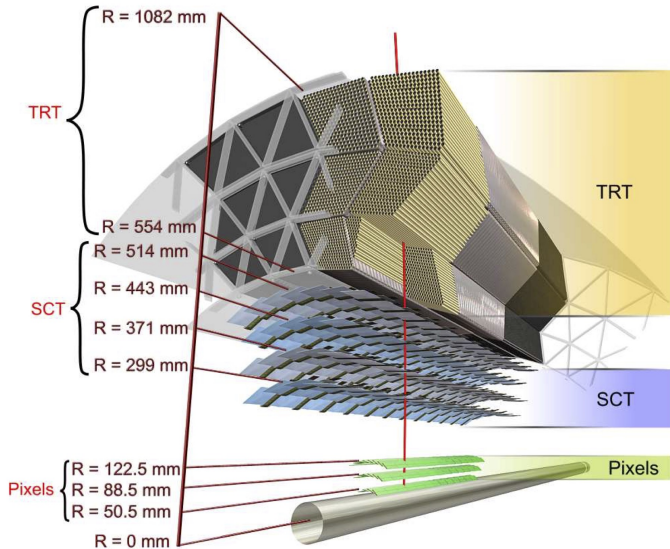


Figure 2.6 – Schematic view of the barrel of the ATLAS inner tracking system [34].

to the measurements of momentum, impact parameter and vertex position. The total number of sensitive items is around 6 million.

The outermost layer ranges from 60 to 95 cm in radius; it is a gas detector (Transition Radiation Tracker) consisting of a set of small diameter tubes, containing Xe (70%), CO₂ (27%), O₂ (3%); it provides a good resolution of the curvature of the track and contributes strongly to its reconstruction.

The tracker contributes to the identification of the electrons, being sensitive to the emission of transition radiation that the particles emit when passing between different materials.

2.2.3 Calorimetric System

Calorimeters must provide good containment for electromagnetic and hadronic showers, they must limit punch-through into the muon system, and finally they must detect the particles that do not lose energy by ionization and are therefore not seen by the internal detector.

It is important that calorimeters cover the largest possible portion of solid angle; in fact, if a particle passes through a region without instrumentation, it is not detected and its energy contributes to the *Missing Transverse Energy* (MET), the precision of which is essential for identifying and studying weakly interacting particles such as neutrinos and, possibly, new BSM particles.

In ATLAS there are two calorimeters: the Electromagnetic Calorimeter (ECAL) and the Hadron Calorimeter (HCAL), as depicted in Figure 2.7 and they cover the range $|\eta| < 4.9$.

The ECAL is divided into a barrel part ($|\eta| < 1.475$) and two end-cap components ($1.375 < |\eta| < 3.2$).

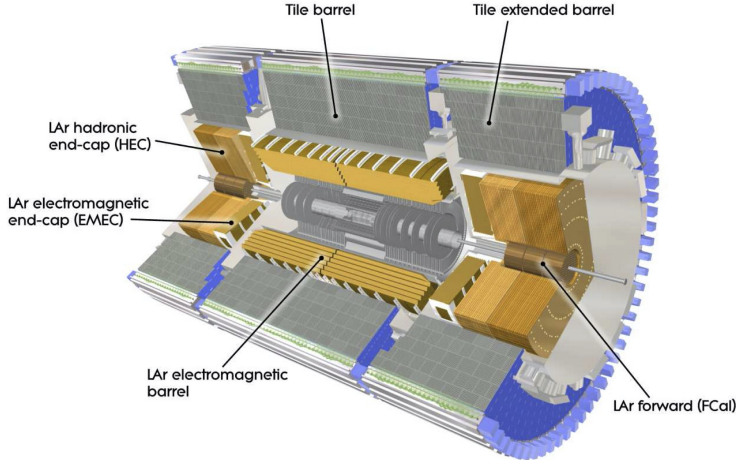


Figure 2.7 – Cut-away view of the ATLAS calorimeter system [34].

each housed in their own cryostat. It is a lead-LAr detector with accordion-shaped kapton electrodes and lead absorber plates over its full coverage. The accordion geometry provides complete ϕ symmetry without azimuthal cracks. The lead thickness in the absorber plates has been optimized as a function of η in terms of ECAL performance in energy resolution.

A schematic representation of the ECAL in the barrel and its main construction parameters are shown in Figure 2.8.

The outer calorimeter is the HCAL, which is divided in Tile Calorimeter (TileCal), the Hadronic End-cap Calorimeter (HEC) and the Forward Calorimeter (FCal).

LAr technology is also used for the hadronic calorimeters, matching the outer $|\eta|$ limits of end-cap electromagnetic calorimeters. The tile calorimeter barrel covers the region $|\eta| < 1.0$, and its two extended barrels the range $0.8 < |\eta| < 1.7$, with a sampling calorimeter using steel as the absorber and scintillating tiles as the active material.

The HEC consists of two independent wheels per end-cap, located directly behind the end-cap electromagnetic calorimeter. The technology is similar to that of the electromagnetic calorimeter in the end-cap region, the active medium is LAr, but the absorption medium is made of copper rather than lead. The FCal ($3.1 < |\eta| < 4.9$) is integrated into the end-cap cryostats, as this provides clear benefits in terms of uniformity of the calorimetric coverage as well as reduced radiation background levels in the muon spectrometer. The FCal consists of three modules in each end-cap: the first, made of copper, is optimized for electromagnetic measurements, while the other two, made of tungsten, measure predominantly the energy of hadronic interactions.

An important quantity in calorimetry is the energy resolution, which is parameterized as:

$$\frac{\sigma_E}{E} = \frac{S}{\sqrt{E}} \oplus \frac{N}{E} \oplus C \quad (2.5)$$

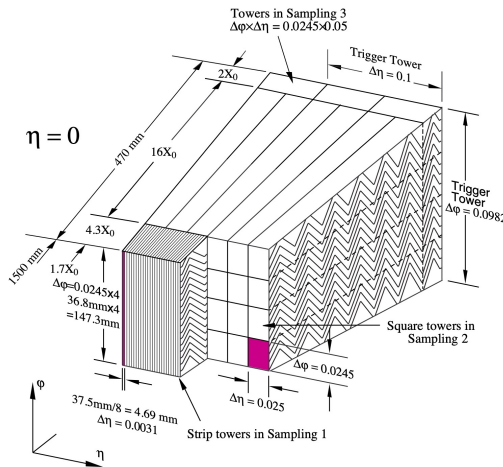


Figure 2.8 – Sketch of the accordion structure of the ECAL [36].

The first term represent the stochastic contribution related to the shower evolution, the second term is related to the read-out electronics and the effect of the pile-up. The last term is a constant, due to systematic effects (e.g. mis-calibrations, dead detector material). The dominant source of uncertainty is linked, at low energy, with the high pile-up whereas, at high energy, C becomes the leading uncertainty.

2.2.4 Muon Spectrometer

The calorimeter is surrounded by the Muon Spectrometer (MS) depicted in Figure 2.9, which is placed at the outermost part of the ATLAS detector.

The outer layers are reached by a few types of particles, mainly muons and neutrinos.

These muons ionize in the material passed through, but the energy, lost in the electromagnetic interaction with other nuclei of the calorimeter, is not sufficient to stop them. The MS identifies muons and measures their momentum.

A series of magnets arranged externally to the calorimeter creates a toroidal-shaped magnetic field that modifies the charged particles direction allowing the measurement of the momentum. For muons with $p_T > 30 \text{ GeV}$ the measurement is much more precise than the measurement obtained by the inner detectors. For lower p_T , on the other hand, the measurement is less accurate, due to the energy loss in the previous layers of the detector and taken in to account to handle *soft muons*, presented in Section 4.2.3.

For both the central part and the end-caps, there are two types of muon detectors:

- a trigger system based on cameras with fast response, such as the *Resistive Plate Chamber* (RPC) and the *Thin Gap Chamber* (TGC),
- precision tracking chambers, such as the *Monitored Drift Tube* (MDT) and the *Cathode Strip Chamber* (CGS).

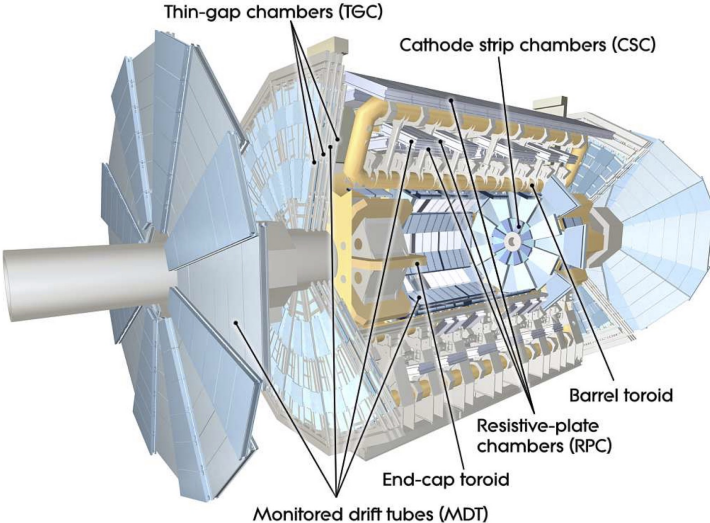


Figure 2.9 – Cut-away view of the ATLAS muon system [34].

In the central region ($|\eta| < 1.05$), the RPCs consist of two parallel planes filled with a mixture of gas that ionizes when a muon passes through. The HV applied between the plates allows the development of avalanches, along the ionization track towards the anode, which constitutes a signal.

In the end-cap ($1.05 < |\eta| < 2.4$), TGCs are used to complement the RPCs in the triggering system for their good time resolution and rate capability.

The TGC is a multi-wire proportional chamber operated in a highly quenching gas mixture. Both TGCs and RPCs can achieve a read-out time of less than 25 ns [37].

The MDTs are used for muons with $|\eta| < 2$, and they are a series of aluminium tubes filled with a gas mixture of Argon and CO₂. A central wire serving as anode allows to collect the electrons that are formed following the passage of the muon into the gas.

The CSCs cover the area while $2 < |\eta| < 2.7$, and are radially-oriented proportional multi-wire chambers, i.e. metal chambers containing a system of parallel and perpendicular anodic wires with strips of opposite polarity.

One important point to stress is that this detector measures the characteristics of any charged particle that passes through it and not just muons. For this reason it is possible that other particles that are not muons, such as pions that manage to overcome the calorimeter are detected as muons. What is presented in this paragraph about the MS is a general overview but much more will be presented in Chapter 3, going deeper on its functioning and its upgrade for the HL-LHC.

2.2.5 Trigger and Data Acquisition

Once fully operational, with the high frequency of collisions typical at LHC, an impressive amount of data is produced (40 MHz of p-p bunch collision frequency), which would be impossible to manage without the application of filters. The *Trigger and Data Acquisition system* (TDAQ) is able to recognize the interesting events for further study.

In Run2 the trigger system consists of two levels of event selection: the *Level-1 trigger* (L1), is an hardware trigger that reduces the rate to 100 kHz, while the *High-Level Trigger* (HLT), is a software trigger, further the reducing event rate to 1 kHz.

The Level-1 trigger is composed by three subsystems: the first is the L1 calorimeter trigger (L1Calo), which uses calorimeter information; the second is the L1 muon trigger (L1Muon), which primarily uses TGC and RPC information to make fast decisions on muon items; the third is the L1 topological trigger (L1Topo) that combines information from L1Calo and L1Muon into the Central Trigger Processor (CTP) which makes the final decision.

At this point, L1 identifies the *Region of Interest* (RoI) with an event rate reduced below 100 kHz. The RoI are then used by the HLT, which has access to the information of all the sub-detectors, targeting the maximum rate of 1 kHz.

Finally, the events are assembled into an event record passes to the offline storage facilities for a complete off-line reconstruction [38].

CHAPTER 3

The Trigger system upgrade for High-Luminosity LHC

Since the beginning, the LHC accelerator has faced operating periods and dedicated shut-downs to upgrade the accelerator machine and the detectors.

In Figure 3.1 a summary of the LHC timeline for operation and upgrade is shown.

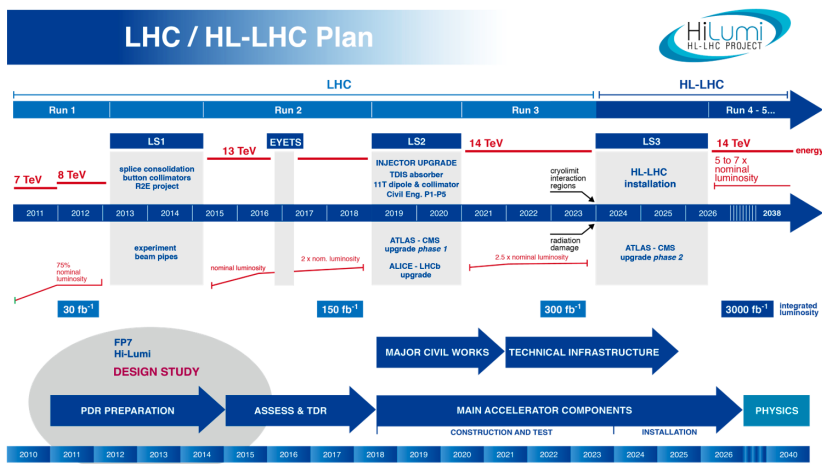


Figure 3.1 – Summary of the LHC timeline for operation and upgrade [39].

At the end of 2018, the LHC was shut-down and for two years it will be upgraded to bring the center-of-mass energy to its design value of 14 TeV and collect 300 fb^{-1} of data, almost double

the current available statistics of Run2. After 4 years of duty cycle, the High-Luminosity period of LHC (HL-LHC) will start and aims to bring the integrated luminosity to 3000 fb^{-1} , unlocking several studies, mostly related with rare phenomena, which are impossible to perform with the current datasets.

This chapter describes the Barrel Muon Trigger system (Section 3.1), the BI upgrade for the HL-LHC (Section 3.2), and the studies performed in the context of the RPC upgrade. In particular, the goal of this work was the implementation of a new simulation to model the digitization of RPC hits in the BI region (Section 3.3) and, using this new model, trigger efficiency studies were performed in the BI and BM/BO regions (Section 3.4). In the end, summary and final considerations are also reported (Section 3.5).

3.1 ATLAS Barrel Muon Trigger

The muon detector chambers are arranged such that particles from the interaction point traverse three stations of chambers.

The system is subdivided azimuthally into 16 sectors numbered from 1 to 16. The sector number increases in the direction of increasing ϕ with the number 1 corresponding to coordinate $\phi = 0$. The odd sector (called “large sectors”) are located between barrel coils, while, the even sectors (called “small sectors”) are covered by the coils.

The muon spectrometer consists of three large air-core superconducting toroidal magnets (two end-caps and one barrel) providing a field of approximately 0.5 T.

In the barrel, the chambers are arranged in three concentric cylinders around the beam axis called BI (Barrel Inner), BM (Barrel Middle), and BO (Barrel Outer).

The RPC planes are installed in the Middle and Outer stations of the Muon Spectrometer and are mechanically associated with MDT precision chambers (except for some “special” chambers).

Schematic drawings of the present ATLAS MS [40], are shown in Figures 3.2 and 3.3. The MS detector and electronics components have been designed for 10 years of operation at a luminosity of $1 \times 10^{34} \text{ cm}^{-2} \text{ s}^{-1}$, corresponding to an integrated luminosity of 1000 fb^{-1} . Conservative safety factors for radiation tolerance and rate capability were taken into account in the original designs, and components have been tested up to and above levels corresponding to the expected doses and rates predicted by simulations multiplied by the safety factors. After the start of LHC operation, detector hit rates and radiation doses could be measured directly, and the previous simulations have been found to agree with the measurements to within a maximum deviation of about 50%.

Based on this observation, the original safety factors were reduced [10], and as a consequence the original irradiation and high-rate tests have qualified the detectors for longer running and higher rates than originally anticipated.

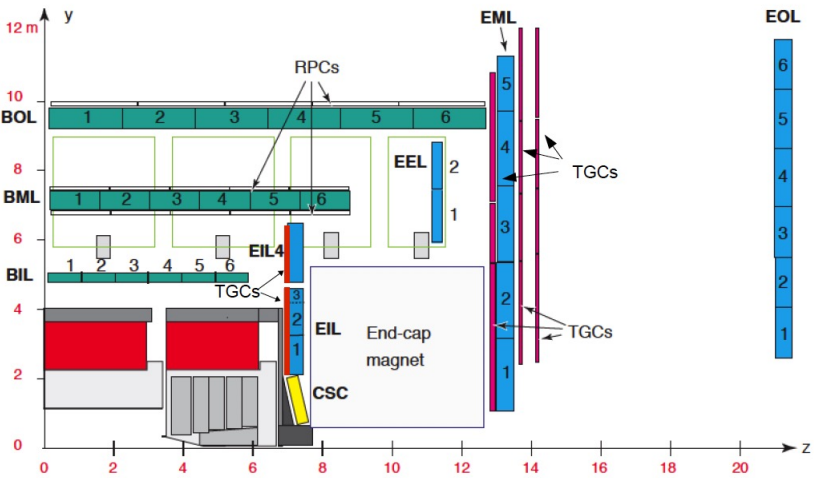
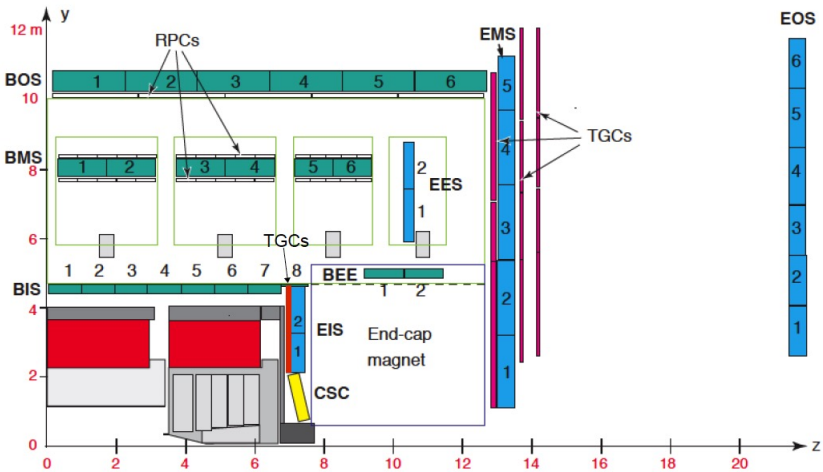


Figure 3.2 – Two R-Z views of the present (Run 1/2) ATLAS muon spectrometer layout. Top: One of the azimuthal sectors that contain the barrel toroid coils (small sector). Bottom: One of the sectors in-between the barrel toroid coils (large sector) [40].

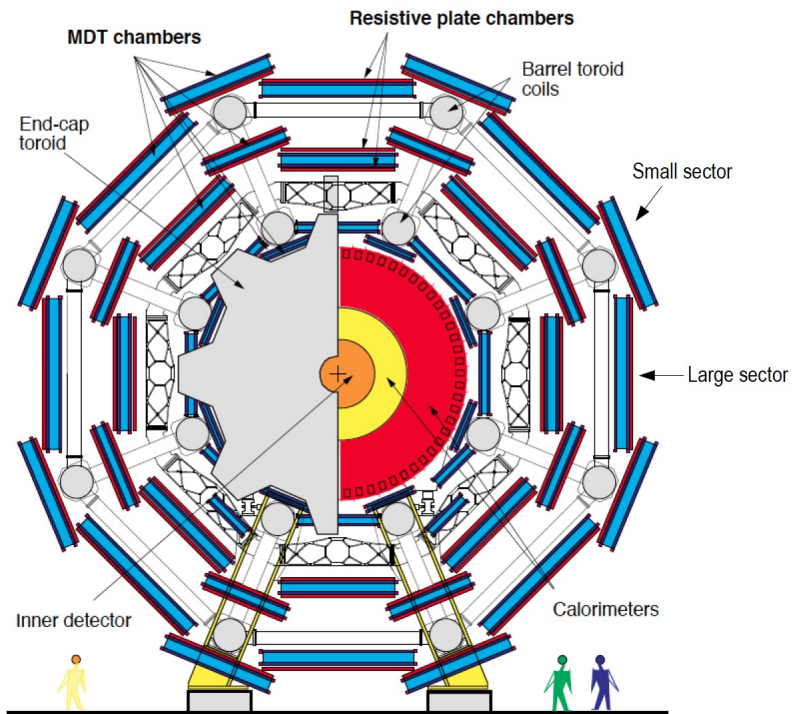


Figure 3.3 – View of the present (Run 1/2) ATLAS muon spectrometer barrel layout in the plane transverse to the beam axis (X-Y plane) [40].

3.2 BI upgrade for Phase-II

In the Phase-I upgrade, foreseen for LS2, the Small Wheels will be replaced by the New Small Wheels (NSW) [41] using small-strip TGC (sTGC) and Micro-Mesh Gaseous Structure (MicroMeGaS or Micromegas) chambers used for both triggering and precision tracking.

At the time of the Phase-II upgrade, there will thus be no CSC chambers any more in the detector, nor will there be the Small Wheel MDT chambers, which are the ones closest to the beam line and exposed to the highest rates. Also in LS2, the BIS7 and BIS8 MDT chambers will be replaced by integrated BIS78 stations of new RPC and small diameter MDT (sMDT) chambers to enhance the trigger coverage in this region [42].

Schematic drawings of the ATLAS MS with the new detectors that will be installed in the Phase-I and Phase-II upgrades are shown in Figure 3.4.

To maintain a high trigger efficiency, new RPC chambers with increased rate capability will be installed on the inner (BI) MDT chambers of the barrel. This addresses a fundamental issue of the present (old) RPC chambers: to ensure their continued operation at the HL-LHC, these chambers will have to be operated at reduced performance (i.e. efficiency), in order to respect the original design limits on currents and integrated charge. This can be achieved by reducing the gas gain through lowering the operating voltages. In the areas of high backgrounds, the gas gain will have to be reduced to such low levels that hit inefficiencies up to 35% will be encountered. This would reduce the trigger efficiency in the barrel region to an unacceptable level if no compensating measures were taken. In addition, due to changes in regulations, the present gas mixture used in ATLAS RPCs may need to be replaced by one with lower global-warming potential (GWP). Unless new gas mixtures are found in time, this too will imply operation of old RPCs at a reduced efficiency. Despite the lower single-hit efficiencies, a high trigger efficiency and purity can be maintained by loosening the requirements on hit coincidences in the old chambers, if at the same time a coincidence with the new BI RPC chambers is introduced. The installation of these chambers will also close most of the acceptance holes of the present barrel muon trigger, which amount to more than 20% of the $\eta - \phi$ coverage for $|\eta| < 1.05$ (see Section 3.4).

Adding new RPC chambers in the barrel is challenging in terms of available space and installation. In the small sectors, the BI RPC chambers can only be installed if the present MDT chambers are replaced by new sMDT chambers with reduced overall thickness so that the sMDT chambers and the new RPCs fit in the same envelope as the original MDT chambers. In the large sectors there is sufficient space available to add the new RPC chambers without replacing the MDTs, if on-detector services are re-arranged.

The retrofitting of selected RPC chambers in the BM and BO layer in the areas of high rate at $|\eta| > 0.8$, namely the BML7 and BOL6 chambers, is a small additional upgrade. The MDT+RPC stations will be temporarily removed from the detector to replace the front-end electronics and the readout panels, so that the chambers can be run at reduced HV without efficiency loss.

In the Section 3.4.1 it will be presented a study performed on the refurbish of BM and BO chambers and the installation of BI chambers in the rail sectors 11 and 15.

The retrofitting can only be done outside the experimental cavern, on the surface, since it requires the disassembly of the RPC chambers. The retrofitting of the BO chambers does not fit into the LS3 schedule because it would interfere with the BI chamber upgrade, and will likely be performed, at least partly, in winter shutdowns after LS3.

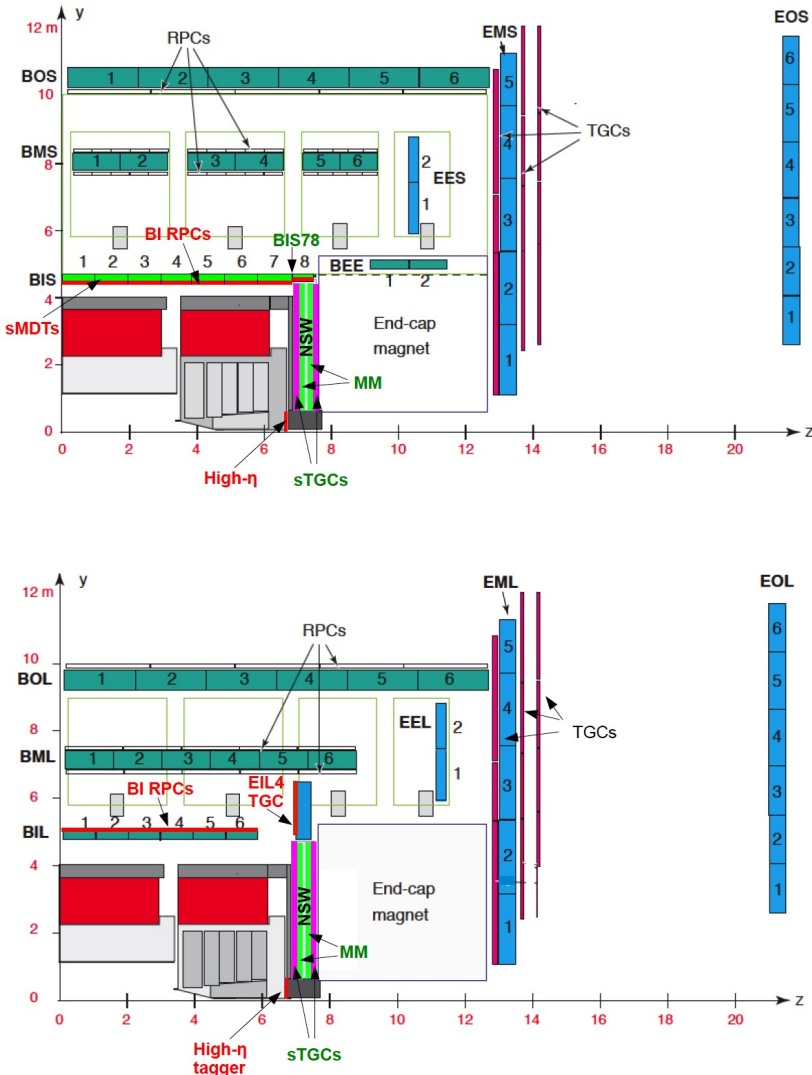


Figure 3.4 – Two R-Z views of the Phase-II ATLAS muon spectrometer layout showing a small sector (top) and a large sector (bottom). The drawings show the new detectors to be added in the Phase-II upgrade, including the addition of the high- η tagger (red text: BI RPC, sMDT, EIL4 TGC, high- η tagger), those to be installed during LS2 (green text: Micromegas and sTGC in the New Small Wheel and BIS78 RPC and sMDT), and those that will remain unchanged from the Run 1 layout (black text) [40].

The main limitations of the RPC system for operation at the HL-LHC are related to the chambers, owing to the more than a factor of seven higher luminosity than the chambers were designed for. The RPC rate capability depends on the total charge delivered per count, which, for the present RPCs, is 30 pC.

As a consequence, the single-gap efficiency will have to be reduced on average by 15%, and by 35% at large η . This efficiency loss will be compensated by installing a new layer of trigger chambers in the BI layer, increasing the overall barrel trigger redundancy.

To operate reliably at the HL-LHC, with high acceptance and efficiency and maintaining the high trigger selectivity of the present system, several upgrades are required for the RPC system:

- A new inner layer of BI RPC chambers will be added to the spectrometer. This will recover most of the current geometrical acceptance holes. The redundancy of the system will be greatly enhanced, so that full trigger efficiency can be maintained even if the old RPCs have to be operated at reduced efficiency, either to limit the effects of ageing or because the use of a different gas mixture is enforced. The BI RPCs will be new-generation RPCs with 1 mm gas gaps and high-sensitivity front-end electronics.
- The trigger and readout electronics (Pad and splitter boxes) have to be replaced in order to make the RPC system compliant with the Phase-II ATLAS trigger and readout scheme. The entire electronics chain, except for the front-end boards, will be replaced. The Pads will be replaced by the new data collector and transmitter (DCT) boards that will send all data off the detector to the counting room USA15 where the trigger and readout logic will be performed.
- In a worst-case scenario for the required reduction of efficiency of the old RPCs, a reduction of the trigger efficiency may still occur even after the BI RPC installation, in the region of $|\eta| > 0.8$. This efficiency loss can be recovered by retrofitting a limited number of BO chambers in that region. The retrofitting comprises replacing the original front-end electronics by the new BI version, and replacing the readout strip panels.

3.2.1 RPC upgrade

The BI system is designed to increase the trigger acceptance and the trigger efficiency, by loosening the requirements on the number of hits in the BM and BO chambers and, at the same time, adding the requirement of a coincidence with the BI layer. Any coincidences of hits in at least three chambers out of four (counting one BI, two BM, and one BO) will be accepted. Two-chamber BI-BO coincidences will be used to cover the remaining acceptance holes. Details of the Phase-II trigger algorithms and their performance are discussed in Section 3.2.2. Figure 3.5 illustrates the recovery of acceptance and efficiency obtained with the Phase-II trigger including the BI RPCs in a worst-case scenario in which the single-hit efficiency of the old RPC is reduced by 15–35% as a function of $|\eta|$, depending on the rate to which each chamber is exposed.

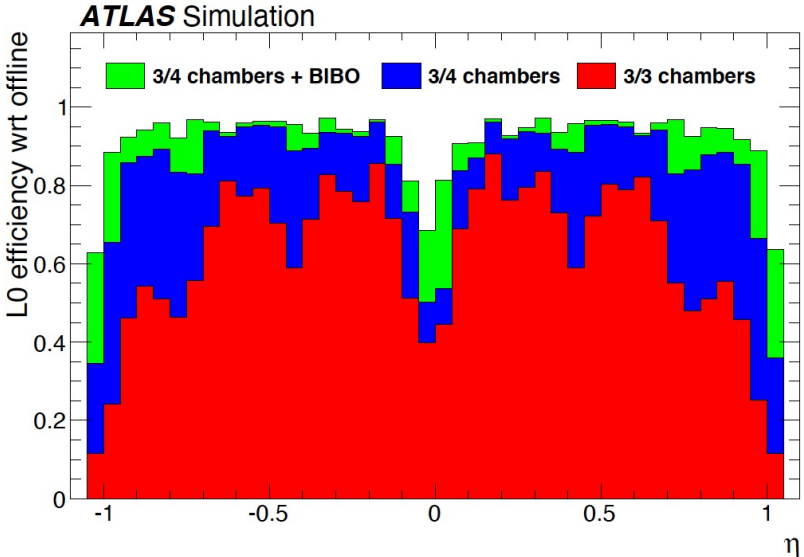


Figure 3.5 – Efficiency times acceptance of the L0 barrel trigger for reconstructed muons with $p_T = 25$ GeV as a function of η , assuming the worst-case scenario [40].

The new BI RPC chambers will have three sensitive gas gaps that are read out independently. A majority logic requiring hits in at least two out of three planes provides high efficiency while suppressing the rate of random coincidences due to uncorrelated hits from photons and neutrons. This is necessary, for instance, to keep the rate of BI-BO coincidences at an acceptable level. A major re-design of the RPC technology started around the year 2010, mainly aiming at a better rate capability and ageing behaviour. The new design is based on a reduced thickness of the gas gaps (from 2 mm to 1 mm) and of the resistive electrodes (from 1.8 mm to 1 mm), and on the use of a new generation of low-noise high-sensitivity amplifiers. Using these amplifiers, full efficiency can be achieved for a lower voltage across the gas gap, thus transferring part of the amplification from the gas avalanche to the electronics. In this way, the RPCs can be operated at a reduced charge per avalanche, reducing the detector current and thus improving rate capability

and ageing. A detail view of the positions of the BI RPCs in ATLAS is shown in Figure 3.6.

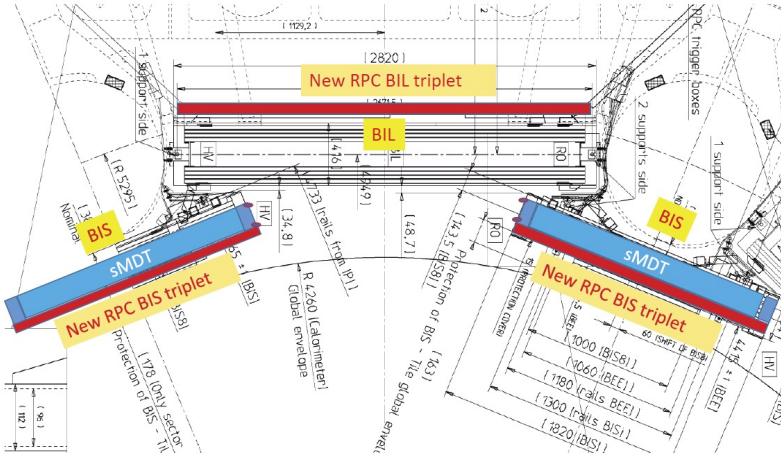


Figure 3.6 – X-Y view of the inner barrel layer, indicating the positions of the BI RPCs (red) and BIS sMDTs (blue) in the small and large sectors [40].

In the small sectors (BIS), due to the tight space limitations, the MDT chambers need to be replaced by new small-diameter MDT (sMDT) chambers with half the tube diameter (15 mm instead of 30 mm) in order to create space for the RPCs on the inside of the sMDT chambers. In the large sectors (BIL), the new RPCs will be installed on the outside of the existing MDTs. The layout of the new BI RPCs leaves the necessary holes and cut-outs for the existing MDT alignment lines and for detector services. It comprises 272 triplet RPC chambers, for a total area of about 470 m². Acceptance studies based on a realistic description of the BI RPC geometry show a geometrical acceptance of the BI RPC chambers of 91% for reconstructed muons with $|\eta| < 1.05$, compared to 95% for the MDT chambers. This results in a barrel trigger acceptance of 96%.

Each detector layer of the triplets is read out on both surfaces by orthogonal strip panels, providing η and ϕ measurements. The compact triplet structure and the use of highly sensitive amplifiers require a complete isolation of individual layers from each other. The choice of strip pitches, 24–26 mm depending on the chamber type, has been constrained by the performance requirements, the strip impedance, and cost considerations. The total number of readout channels is about 8700.

3.2.2 Trigger scheme

All the hits from RPC detectors will be available to the barrel Sector Logic board that uses them to generate barrel trigger candidates. The new BI RPCs increase the geometrical acceptance of the present barrel muon trigger and its robustness against inefficiencies of the old BM and BO RPCs caused by the reduced operating voltages necessary to ensure their longevity.

The RPC trigger will use nine measurement planes, provided by four layers of RPC chambers: one BI triplet (RPC0), two BM doublets (RPC1 and RPC2), and one BO doublet (RPC3).

Figure 3.7 shows the positions of the BI, BM, and BO RPC chambers in a small barrel sector together with the MDT chambers. The acceptance holes in the BM layer, caused by the magnet coils and their supports, are also visible.

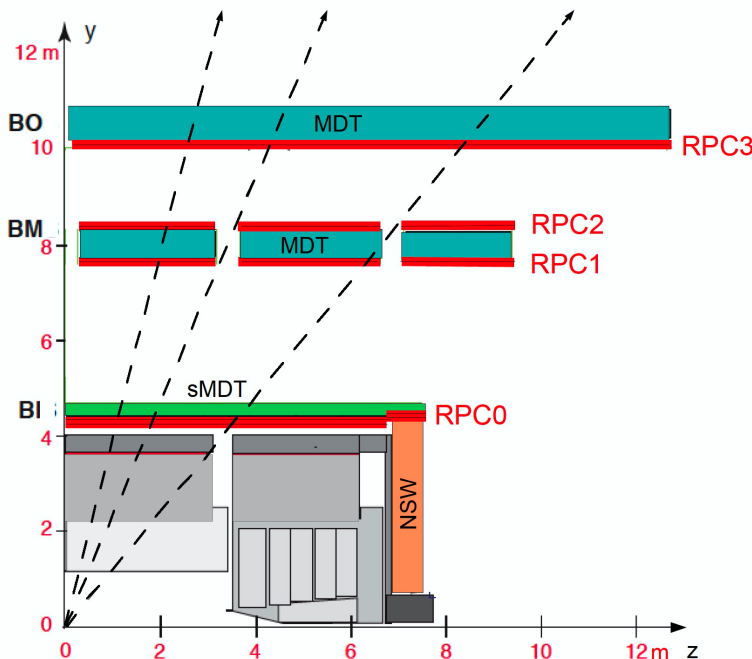


Figure 3.7 – Transverse section of a small sector in the barrel region, showing the four layers of RPC chambers (RPC0,1,2,3), as well as the MDT chambers in the barrel-inner (BI), barrel-middle (BM), and barrel-outer (BO) layers. The three dashed lines represent muon trajectories traversing four, two, and three RPC chambers [40].

To take advantage of the redundancy of detector planes, a trigger algorithm that does not make use of a fixed pivot plane (as in present ATLAS muon trigger) has been developed. This makes it possible to define different trigger coincidence logic schemes.

These schemes (summarised in Table 3.1 and illustrated in Figure 3.8) are based on different requirements on the four layers of RPC chambers:

- 3/3 chambers. Hits in at least three out of four planes of the RPC1+RPC2 chambers and in at least one out of two planes of RPC3. This is equivalent to the present high-pT trigger.
- 3/4 chambers. The previous requirement in a logical OR with the requirement of hits in at least two planes out of three in RPC0 and in at least three planes out of six in RPC1+RPC2+RPC3. In this way, all combinations of three-chamber coincidences (satisfying the above hit requirements) are accepted.
- 3/4 chambers + BI-BO. The previous requirement in a logical OR with the requirement of at least two hits in RPC0 and at least one hit in RPC3. This enhances the trigger coverage in the regions where no BM RPCs are installed due to the mechanical support structure of the toroid coils. The BI-BO coincidence is expected to be prone to accidental coincidences of uncorrelated background hits that are negligible in three-chamber coincidences. In the baseline version of this trigger, BI-BO coincidences are used in the whole barrel region, but can be limited to the BM acceptance gaps, if the muon trigger rate in the barrel gets too high.

Trigger	Requirement
3/3 chambers	$3[\text{RPC1+RPC2}] \text{ AND } 1[\text{RPC3}]$
3/4 chambers	$(3[\text{RPC1+RPC2}] \text{ AND } 1[\text{RPC3}]) \text{ OR } (2[\text{RPC0}] \text{ AND } 3[\text{RPC1+RPC2+RPC3}])$
3/4 ch.+BI&BO	$(3[\text{RPC1+RPC2}] \text{ AND } 1[\text{RPC3}]) \text{ OR } (2[\text{RPC0}] \text{ AND } 3[\text{RPC1+RPC2+RPC3}])$ $\text{OR } (2[\text{RPC0}] \text{ AND } 1[\text{RPC3}])$

Table 3.1 – The hit requirements used in different RPC triggers. The left column shows the short name used in the text. The right column gives the coincidence scheme used for the selection logic. The notation $N[\text{RPC}_i+\text{RPC}_j+\dots]$ indicates a majority requirement of hits in at least N planes out of all the possible planes available in RPC chambers RPC_i , RPC_j, \dots with $i, j, \dots \in \{0, 1, 2, 3\}$.

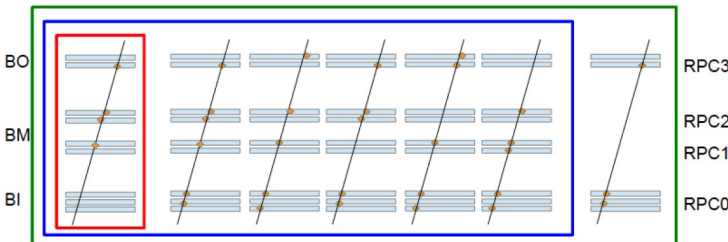


Figure 3.8 – Graphic view of the coincidence scheme used for the selection logic. High-Pt (3/3 chambers) in red, 3/4 chambers in blue, 3/4 chambers+BI&BO in green.

3.3 Hit digitization in the BI region

Since at the present time the new chambers in the BI region are not yet installed, the simulation performed for this work takes into account the presence of hits in the BI RPC chambers exploiting the true hits, recorded by the MDT chambers in the BI region, and treating them as hits of the future RPC chambers.

In this work, it has been used the the common framework `muTrigNt_write` [43] that includes a realistic digitization. This code reproduces the dimensions of the new BI RPC chambers and, given as input the true MDT hits, it checks if the hits are in the geometric acceptance. The code also allows to generate strips, of an arbitrary pitch, in the two orthogonal directions (η and ϕ) and thus to digitize the true MDT hits, recording them as hits with the coordinates reported in the center of the strip. In this way, it is possible to completely simulate the RPC chamber.

The studies presented in this chapter were performed using the official MC sample `mc15_14TeV.422063.ParticleGun_single_mu_Pt50.recon.ESD.e5392_s2988_s3000_r8974` [44], containing 50K events, produced with the ITk (Inner Tracker) simulation and with the layout of Run-I muons, that differs compared to the layout of Run-II muons because the feet and the elevator chambers are missing. This MC sample considers muons reconstructed in $|\eta| < 1.05$ by the off-line reconstruction, using a single-muon MC sample with fixed $p_T = 50$ GeV.

Given the framework described above, the goal of this work was to implement a simulation with a more realistic digitization that would produce:

- cluster size, strip number and the associated coordinates of the strips (Section 3.3.1);
- timing (Section 3.3.2);

3.3.1 The cluster size model

A single discharge in the gas volume can induce a signal in more than one RPC strip (i.e. it causes a so-called *cluster*), which is due to the charge sharing. The number of the RPC strips fired in temporal coincidence is called *cluster size*. The cluster size is a relevant parameter for the RPC detector and it must be strictly monitored to ensure a full trigger efficiency. The cluster size is simulated using a Gaussian charge distribution, with fixed width and centered on the true MDT hit that is induced on the strips [45]. This function is defined as:

$$G(z) = A(z) \cdot \frac{2}{\pi} \int e^{-\frac{\mu-z}{\sigma\sqrt{2}}} \quad (3.1)$$

where the amplitude $A(z)$ is a random distribution having a decreasing exponential distribution $f(A) = e^{-\frac{z}{\tau}}$, with the parameter $\tau = 0.8$, fixed width $\sigma = 16$ mm and μ is the z -coordinate of the hit. When the charge integrated over a strip exceeds a certain threshold (0.2 in this simulation), the strip is switched on.

This is not a strictly physical model but a decreasing exponential is useful to produce the expected tail, in the absence of a more realistic model for amplitudes based on experimental studies. A picture of the model used in this simulation is illustrated in Figure 3.9.

Cluster size is given by the number of strips fired at the same time.

It depends on the absolute value of charge integrated over a strip, but it also depends on the position of the true hit. Originally, the RPC hit is fixed to be at the center of the strip and the true MDT hit belongs to one strip only but in this simulation, it would be possible to have many strips fired at the same time using the relation: $\text{GlobPos}_i = \text{GlobPos}_{i,\text{true}} \pm \text{strip_center}_i$.

The resulting cluster size distribution is in line with the expectations in [40] and shown in Figure 3.10.

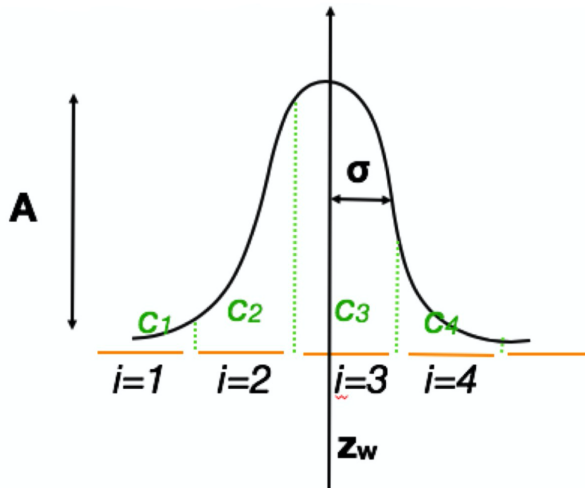


Figure 3.9 – Cluster size model used in the simulation. C_i is the charge integrated over a strip i . Some other parameters are the strip pitch z_w (22 mm), random amplitude A and width σ . When the charge integrated over a strip exceeds a certain threshold, the strip is switched on [45].

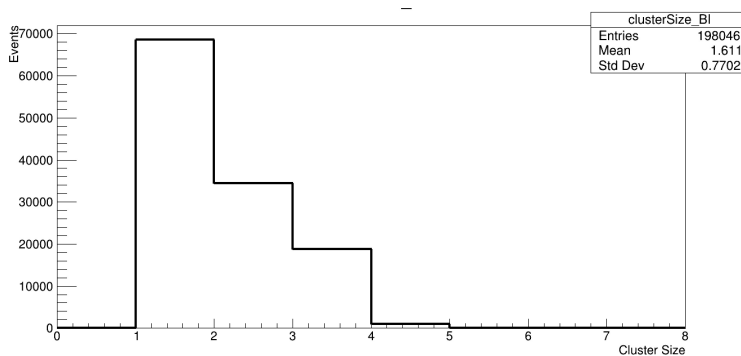
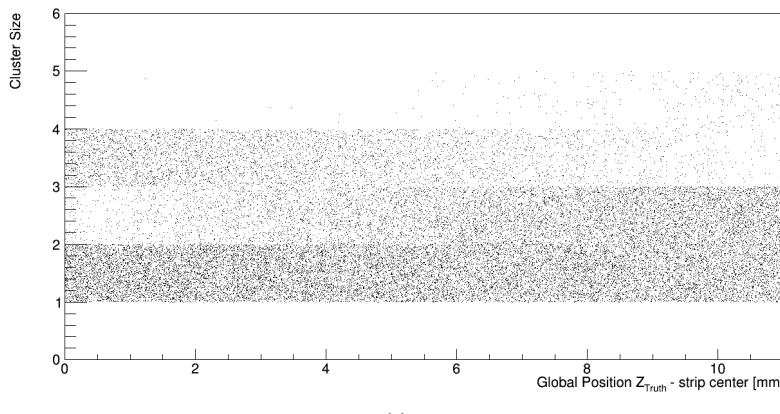


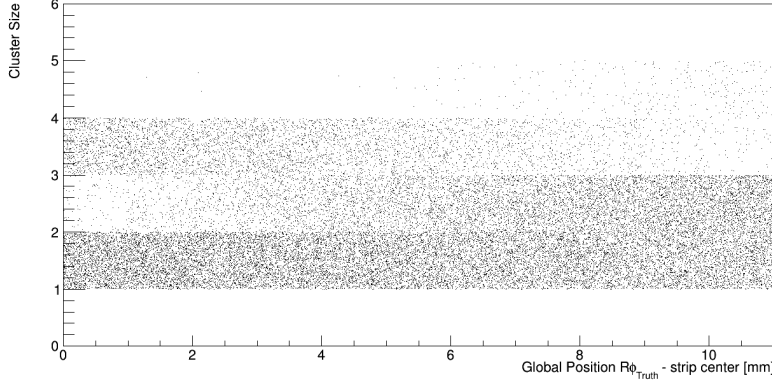
Figure 3.10 – Cluster size distribution obtained with the model and parameters illustrated in this section. The average value is 1.6.

Considering the hit distribution in Figure 3.11(a) for the η layer and Figure 3.11(b) for the ϕ layer, it is possible to see that:

- CS=0 is never possible by definition, one hit corresponds to at least one fired strip;
- CS=1 the hit distribution is uniform, because the integrated charge is less than the fixed threshold;
- CS=2 mostly when the truth hit is far from the strip center and at the strip edge;
- CS=3 mostly when the truth hit is far from the strip edge and at the strip center;
- CS=4 mostly when the truth hit is far from the strip center and at the strip edge.



(a)



(b)

Figure 3.11 – RPC hit distribution GlobPos_i for (a) strips along η and (b) strips along $R\phi$.

Strips in η and ϕ layers are orthogonal to each other and it is possible to see how they are arranged as a function of the Global Position in the BI region of the ATLAS detector.

In particular, in Figure 3.12(a) strips oriented along η are ordered in such a way that the strip number one is the inner strip, while Figure 3.12(b) shows that strips oriented along ϕ are always oriented with increasing ϕ .

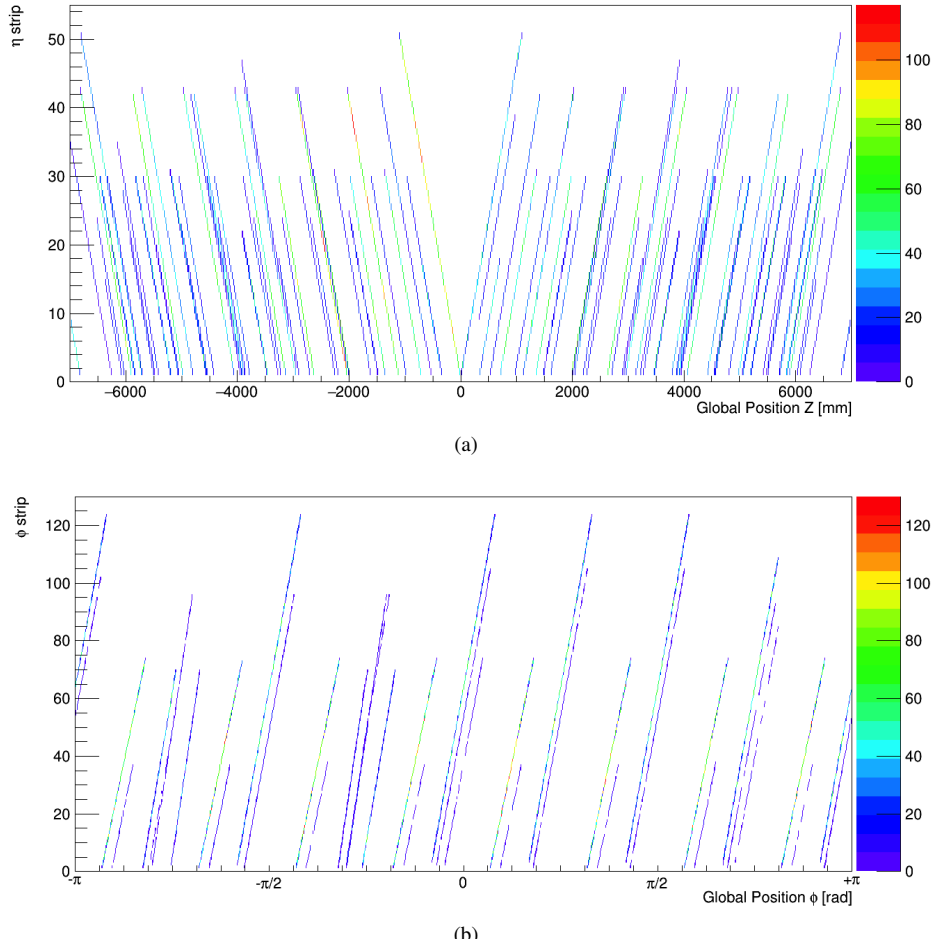


Figure 3.12 – Arrangement of strips in the (a) η layer and (b) ϕ layer as a function of the Global Position in the BI region of the ATLAS detector.

Tables 3.1(a) and 3.1(b) summarises the main chamber parameters of the expected layout for the Phase-II upgrade. Strip and front-end board entries are based on the assumptions of a 20 mm pitch and eight channels per board.

Figure 3.13 shows the number of η and ϕ strips switched on in the simulation. It is possible to verify that the simulation developed for this work follows the requirements of the Phase-II upgrade for BI RPCs to be realistic and reliable as much as possible.

RPC type	BIL-A	BIL-B	BIL-C	BIL-D	BIL-K	BIL-E	BIL-F	BIL-G	BIL-H	BIL-I	BIL-J
# of units	72	2	4	2	2	14	2	8	6	2	2
# of layers	3	3	3	3	3	3	3	3	3	3	3
length in Z (mm)	640	510	365	600	220	640	540	450	310	370	370
width in ϕ (mm)	2750	2750	2750	2750	2750	2380	2380	2300	2100	1850	1700
η strip pitch (mm)	18.4	19.2	19.7	17.2	21.3	18.4	20.4	16.7	16.3	20.0	20.0
ϕ strip pitch (mm)	21.1	21.1	21.1	21.1	21.1	20.8	20.8	21.6	21.4	20.5	20.6
# η strips/layer	32	32	16	32	8	32	24	24	16	16	16
# η strips/unit	96	96	48	96	24	96	72	72	48	48	48
# ϕ strips/layer	128	128	128	128	128	112	112	104	96	88	80
# ϕ strips/unit	408	408	408	408	408	360	360	336	312	288	264
area/layer (m^2)	1.76	1.40	1.00	1.65	0.61	1.52	1.29	1.04	0.65	0.68	0.63
gap area (m^2)	1.61	1.25	0.86	1.50	0.47	1.39	1.15	0.91	0.54	0.58	0.54
Gas volume/layer (l)	4.82	3.76	2.59	4.49	1.41	4.16	3.46	2.73	1.63	1.75	1.61
# FE cards/layer η	4	4	2	4	1	4	3	3	2	2	2
# FE cards/layer ϕ	16	16	16	16	16	14	14	13	12	11	10

RPC type	BIR-A	BIR-B	BIR-C	BIR-D	BIM-A	BIM-B	BIS-A	BIS-B
# of units	4	8	8	4	12	24	16	80
# of layers	3	3	3	3	3	3	3	3
length in Z (mm)	780	916	1104	735	437	495	1096	916
width in ϕ (mm)	2099	1251	819	1260	1536	1536	1820	1820
η strip pitch (mm)	18.3/22.8	21.7	22.0	21.4	16.1/24.2	18.5/27.8	21.8	21.7
ϕ strip pitch (mm)	21.3	21.4	19.2/24.0	21.6	20.6	20.6	20.1	20.1
# η strips/layer	40/32	40	48	32	24/16	24/16	48	40
# η strips/unit	120/96	144	168	96	72	72	168	120
# ϕ strips/layer	96	56	40/32	56	72	72	88	88
# ϕ strips/unit	288	168	120/96	168	216	216	264	264
area/layer (m^2)	1.64	1.15	0.90	0.93	0.67	0.76	2.00	1.67
gap area (m^2)	1.51	1.05	0.82	0.84	0.58	0.67	1.86	1.54
Gas volume/layer (l)	4.52	3.15	2.45	2.51	1.75	2.01	5.59	4.63
# FE cards/layer η	5/4	5	6	4	3/2	3/2	6	5
# FE cards/layer ϕ	12	8	5/4	7	9	9	11	11

Table 3.2 – Main parameters of (a) the BIL RPC chambers and (b) the BIR/BIM/BIS RPC chambers [40].

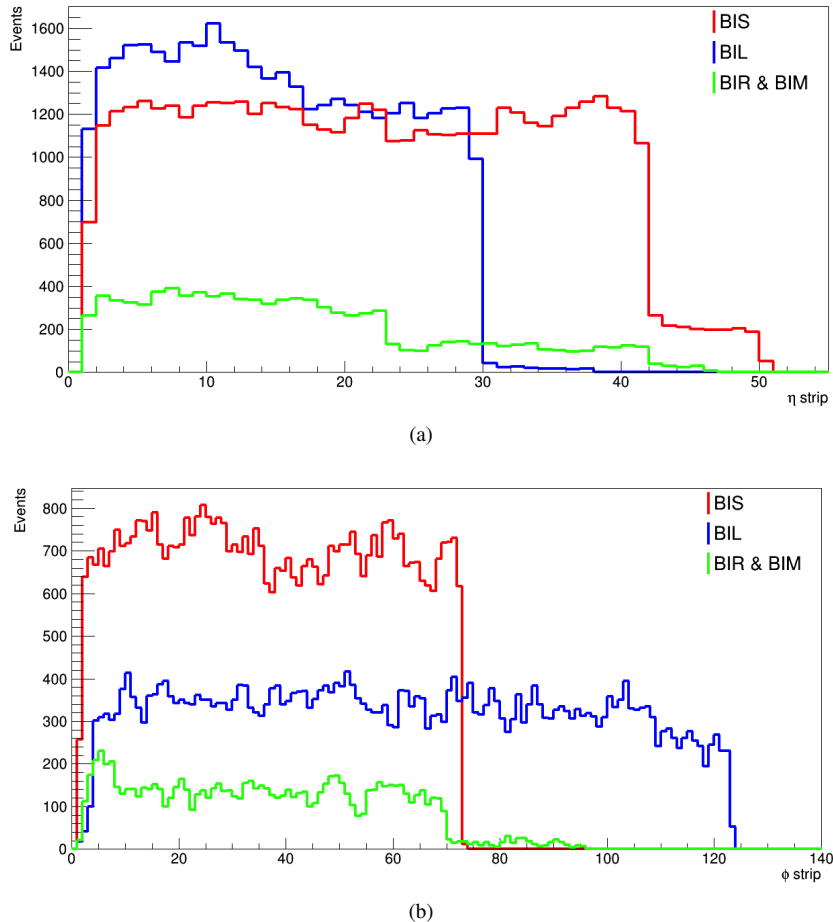


Figure 3.13 – Number of (a) η and (b) ϕ strips switched on for different chambers: BIS in red, BIL in blue, BIR & BIM in green.

3.3.2 Timing

Another important variable is the time taken for the particle to pass through the detector. It is important because it is one of the discriminating variables in the algorithm's selection of hits. Only hits recorded in the bunch crossing event are considered and not all the hits previously recorded. Therefore, all hits outside 25 ns coincidence window around the bunch crossing of interest are excluded.

In order to simulate the new RPCs one has to take into account several effects and apply an appropriate correction and extract a digital readout.

The final formula used to extract the digitized time in which the hit is recorded by the detector is:

$$t_{hit} = \text{int}^1 \left\{ \frac{t_{true} + t_{Gauss} + t_{FE} - t_{cal}}{\Delta t} \right\} \Delta t \quad (3.2)$$

- t_{true} is the true hit recorded by the MDT;
- Δt is the sampling rate (0.3 ns). The final t_{hit} must be a multiple of the sampling rate to have a digitization;
- t_{Gauss} is a Gaussian term that reproduces the fluctuations in the RPC signal (smearing 0.4 ns);
- t_{FE} is the propagation of the signal along the strip to the FE electronics assuming that the signal speed on the layer is 200 mm/ns;
- t_{cal} is the calibration offset. The true hit timing is recorded referring to the time of the collision on the MDT tubes. To report the timing centered around 0, it was necessary to subtract the time of flight of the particle assuming time to be calibrated with prompt muons crossing the center of the strip at $t = 0$.

Figure 3.14 shows the digitized time associated to the RPC hit calculated using the Equation 3.2. The tail of the distribution is given by low p_T muons that produce secondary hits.

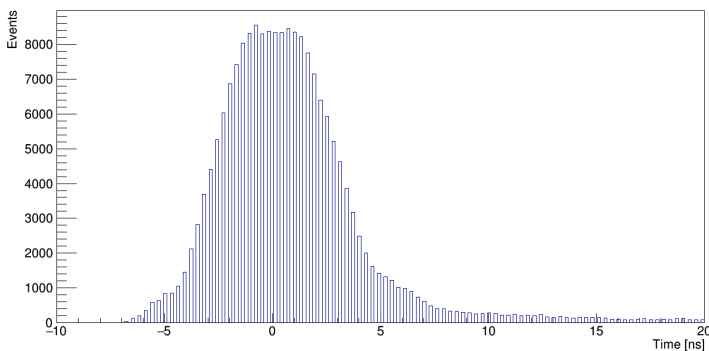


Figure 3.14 – Digitized time associated to the RPC hit. The tail of the distribution is given by low p_T muons that produce secondary hits

¹The int function takes the integer part of a real number.

3.4 L0 barrel trigger efficiency

The performance of the barrel muon trigger was studied using single-muon MC samples with fixed $p_T = 50$ GeV, for a fixed transverse momentum threshold: $p_T > 10$ GeV [46] and with the hit digitization described in the previous sections.

To study the robustness of the trigger against possible efficiency reductions of the old RPCs in the BM and BO layers, the simulation was performed in the so-called "worst-case scenario" that introduces inefficiencies depending on the station type and sector and summarised as Table 3.3. It includes inefficiencies due to a reduction of the high voltage of the BM and BO RPCs such that the expected RPC current is always below the safe operation limit.

Station Name	StationEta							
	1	2	3	4	5	6	7	8
BOL	0.90	0.90	0.82	0.82	0.76	0.74	-	-
BOS/BOG/BOF	0.89	0.90	0.90	0.90	0.89	0.66	0.60	0.60
BML	0.88	0.88	0.88	0.83	0.56	0.56	0.60	-
BMS	0.90	0.90	0.90	0.87	0.81	0.81	-	-

Table 3.3 – Efficiency for each station and sector of the barrel muon trigger in the "worst-case scenario". This scenario includes inefficiencies due to a reduction of the HV of the BM and BO RPC [46].

The trigger efficiency times acceptance for each trigger logic scheme is listed in Table 3.4 and it is defined as the fraction of reconstructed muons that are accepted by the trigger, using the simulation that includes the RPC detector efficiency. The trigger efficiency times acceptance is also presented in Figure 3.15. Adding the new BI RPC layer greatly reduces the dependence of the trigger efficiency on the hit efficiency of the old RPCs.

BM and BO efficiency (%)	Trigger efficiency x acceptance (%)		
	3/3 chambers	3/4 chambers	3/4 chambers + BIBO
WCS	58.78	83.27	91.89

Table 3.4 – Efficiency times acceptance for the L0 barrel trigger for each trigger logic scheme, assuming the worst-case scenario with the hit digitization .

Starting from the WCS scenario, other two studies have been performed on the L0 barrel trigger efficiency using simulations with RPC stations in various operational conditions: the first study is the refurbish of BM and BO chambers (Section 3.4.1) and the second study is about the installation of BI chambers in the rail sectors 11 and 15 (Section 3.4.2).

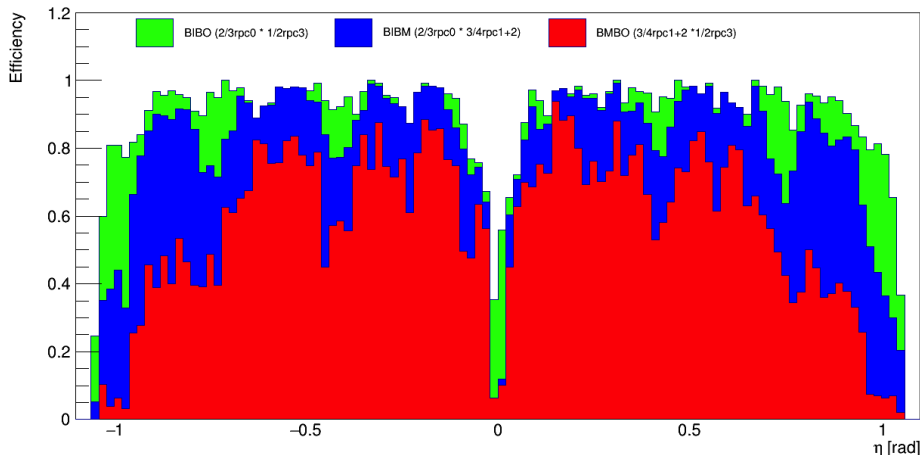


Figure 3.15 – Efficiency times acceptance of the L0 barrel trigger for each trigger logic scheme, assuming the worst-case scenario with the hit digitization.

3.4.1 BM and BO retrofitting

In the Phase-II upgrade of the muon system, most of the readout electronics will be replaced to make it faster and resistant to radiation. An essential step is therefore to understand what would be the impact of the legacy BM/BO chambers with the new electronics.

In this first study, efficiencies of the "worst-case scenario" summarised in Table 3.3, are used, except for the following stations set to 100% efficiency:

1. BML 7,
2. BOL 6,
3. BOS 6,
4. BOL 5.

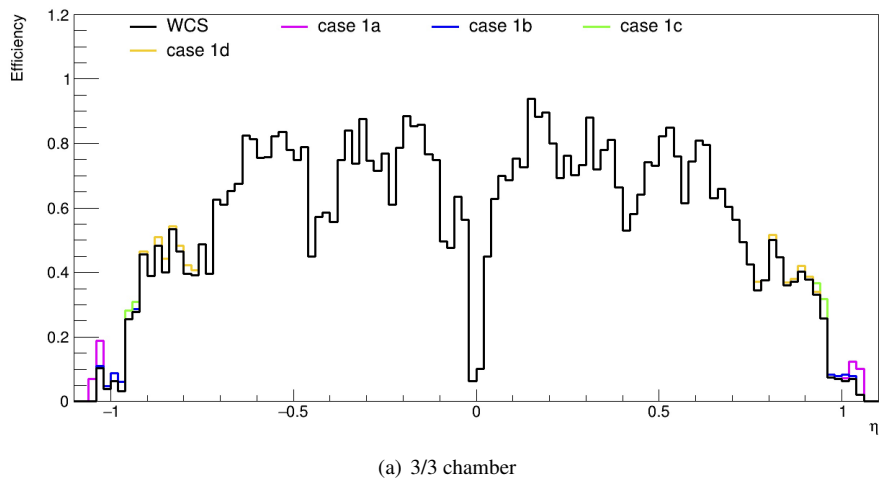
The products of muon trigger efficiency and acceptance for the BM and BO retrofitting are listed in Table 3.5.

The trigger efficiency times acceptance is also presented in Figure 3.16 that compare the "worst-case scenario" with all the variants of the WCS, in which some stations are fixed to 100% efficiency.

In the first analysed case, the most relevant effect on the trigger efficiency times acceptance is on the 3/4 chambers logic scheme, in particular for the Case 1b (BOL 6 100%) the variation is +1.08% compared to the "worst-case scenario".

BM and BO efficiency (%)	Trigger efficiency x acceptance (%)		
	3/3 chambers	3/4 chambers	3/4 chambers + BIBO
WCS	58.78	83.27	91.89
Case 1a (BML 7 100%)	+0.22	+0.26	+0.14
Case 1b (BOL 6 100%)	+0.13	+1.08	+0.53
Case 1c (BOS 6 100%)	+0.16	+0.51	+0.63
Case 1d (BOL 5 100%)	+0.23	+0.82	+0.41

Table 3.5 – Efficiency times acceptance for the L0 barrel trigger for different assumptions on the hit efficiency of the present RPC detectors. The “WCS” row corresponds to the scenario in which the efficiencies are listed in Table 3.3. The other rows correspond to the variants of the WCS, in which the efficiency of some stations are set to 100%. The corresponding results of these variants, are expressed as variations to the WCS [46].



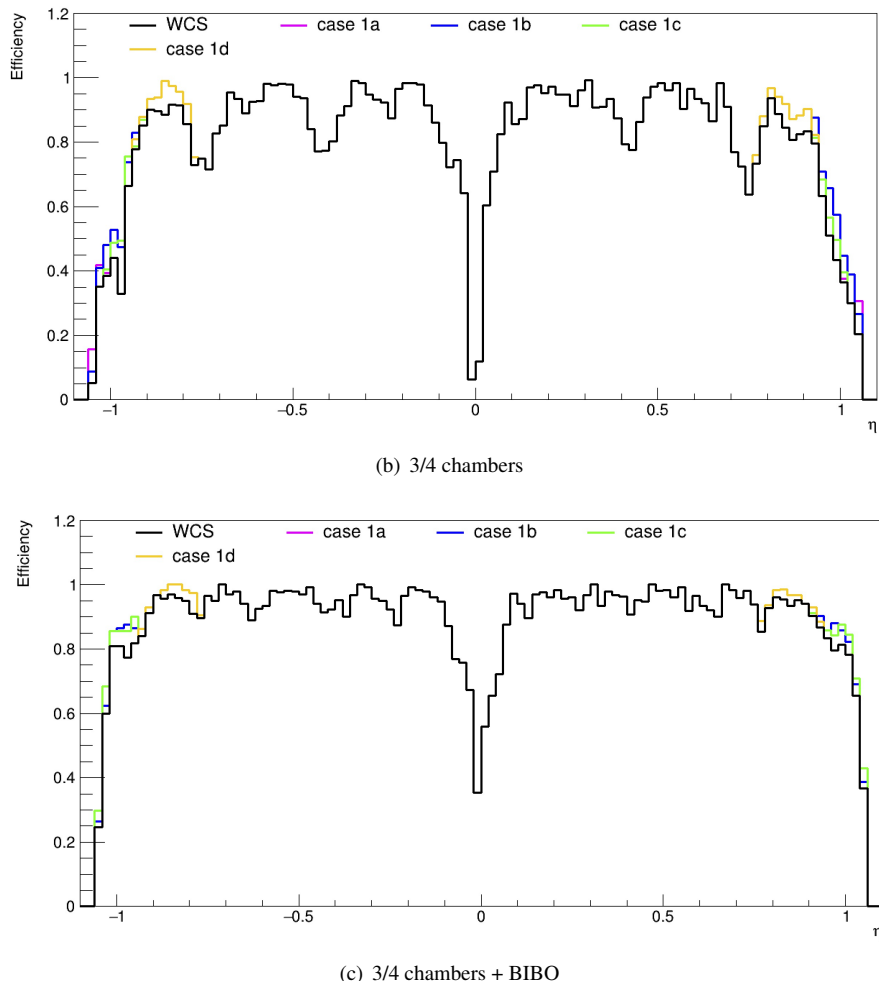


Figure 3.16 – Efficiency times acceptance of the L0 barrel trigger compared to reconstructed muons with $p_T = 50$ GeV as a function of η taking in to account all the variants of the WCS. The histograms show the efficiency of (a) the existing 3/3 chambers trigger, of (b) the 3/4 chambers trigger including the BI layer, and (c) the additional gain from the BI-BO trigger. Efficiency times acceptance is defined as the fraction of reconstructed muons accepted by the trigger, using a simulation that includes the RPC detector efficiency [46].

3.4.2 Dropping BIR and BIM chambers

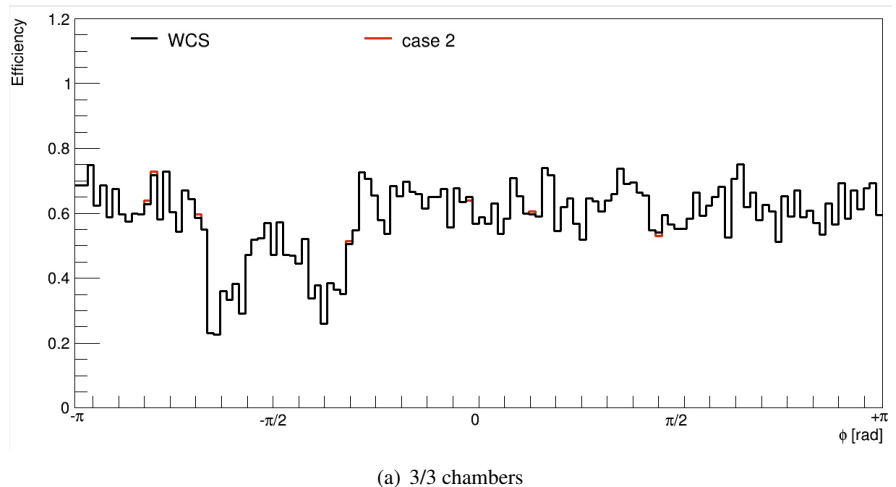
Since the installation of the RPCs in the sectors 11 and 15 seems to be very hard, another special case was performed simulating a scenario in which BIM and BIR RPC are not installed in these sectors.

The products of muon trigger efficiency and acceptance for this second study are listed in Table 3.6.

The results are also presented in Figure 3.17 that compares the "worst-case scenario" with this second case, in which BIM and BIR are turned off. The efficiency distributions show that the absence of BIR and BIM has the most relevant effect on the 3/4 chambers + BIBO logic scheme with a corresponding variation of -3.11%.

BM and BO efficiency (%)	Trigger efficiency x acceptance (%)		
	3/3 chambers	3/4 chambers	3/4 chambers + BIBO
WCS	58.78	83.27	91.89
Case 2 (BIM BIR off)	+0.03	-2.70	-3.11

Table 3.6 – Efficiency times acceptance for the L0 barrel trigger for different assumptions on the hit efficiency of the present RPC detectors. The WCS row corresponds to the scenario in which the efficiencies are listed in Table 3.3. The row "Case 2" corresponds to the case in which the RPCs in the sectors 11-15 (BIM and BIR) are turned off. The corresponding results of the Case 2, are expressed as variations to the WCS [46].



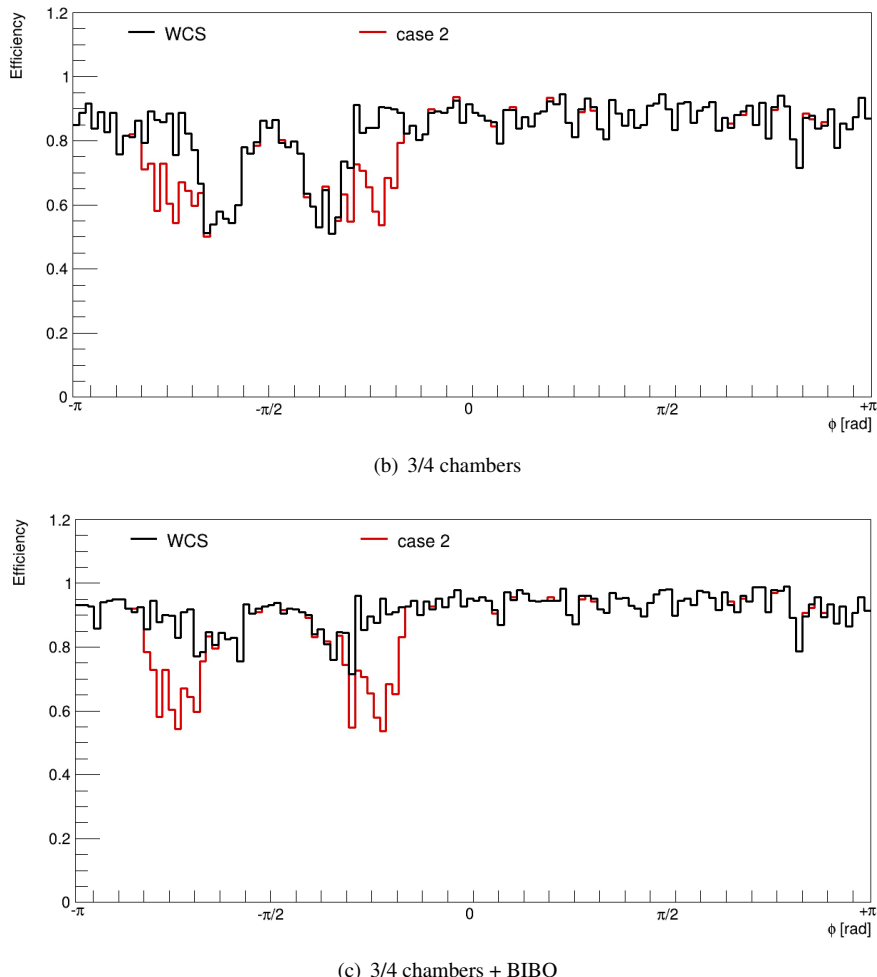


Figure 3.17 – Efficiency times acceptance of the L0 barrel trigger compared to reconstructed muons with $p_T = 50$ GeV as a function of ϕ . The histograms show the efficiency of (a) the existing 3/3 chambers trigger, of (b) the 3/4 chambers trigger including the BI layer, and (c) the additional gain from the BI-BO trigger. Efficiency times acceptance is defined as the fraction of reconstructed muons accepted by the trigger, using a simulation that includes the RPC detector efficiency [46].

3.5 Summary and considerations

The works described in this chapter aimed at a new simulation of the RPC in the BI region. They involved the construction of a model:

- for the definition of the cluster size, which is important for creating a simulation as realistic as possible;
- to define a variable that represents the time taken by the particle to pass through the detector, which is important because it is one of the discriminating variables in the algorithm's selection of hits.

The new developed model results in agreement with the required technical characteristics of the RPCs for Phase-II, described in the Technical Design Report [40].

A more realistic simulation of the RPCs is now available for further studies.

Using this model, L0 barrel trigger efficiency studies were performed in the following two scenarios:

1. the refurbish of BM and BO chambers, to understand what would be the impact of the legacy BM / BO chambers with the new electronics;
2. the drop of BIR and BIM chambers, given that the installation of the RPCs in the sectors 11 and 15 seems to be very hard.

The first scenario gives an estimation of the improvements by replacing the electronics. Moreover, the most significant expected improvement is from BOL6.

The second scenario showed that there is a significant loss of efficiency if the collaboration decides to don't install the RPC in sectors 11 and 15.

These two studies will help plan the work for the Phase-II upgrade.

CHAPTER 4

Data modeling and object reconstruction

Monte Carlo event generators are the indispensable workhorses of particle physics, bridging the gap between theoretical ideas and first-principles calculations on the one hand, and the complex detector signatures and data of the experimental community on the other hand. In fact, they are mainly used to predict event rates and topologies, simulate possible backgrounds, study detector requirements and study detector imperfections.

The same reconstruction algorithms used to reconstruct data are also applied to all MC samples.

4.1 Event simulation

To understand what the final state of any given physics process will look like, *Monte Carlo simulation* (MC) is used to model both the initial and final state of the process of interest, as well as the propagation of particles through the detector.

A typical MC simulated $p - p$ collision can be schematized as in Figure 4.1.

The first step of an event simulation is represented by the extraction of initial-state partons and the evaluation of their momenta using the proton PDFs.

Fixed order matrix element (ME) are used to determine the cross section for the hard scatter integrated over the phase space of the final state particles and it also predicts their momenta.

The particles produced by the hard scatter then undergo a process of *parton showering* (PS), where the quarks and gluons produce a “shower” of further coloured particles.

Particles are emitted and produced until the energy scale is below 1 GeV, at which point, the *hadronisation* process starts and colorless hadrons are formed. These hadrons then decay into lighter particles.

As well as the original hard scatter, additional interactions between other partons within the proton must be included in a process known as *underlying event*.

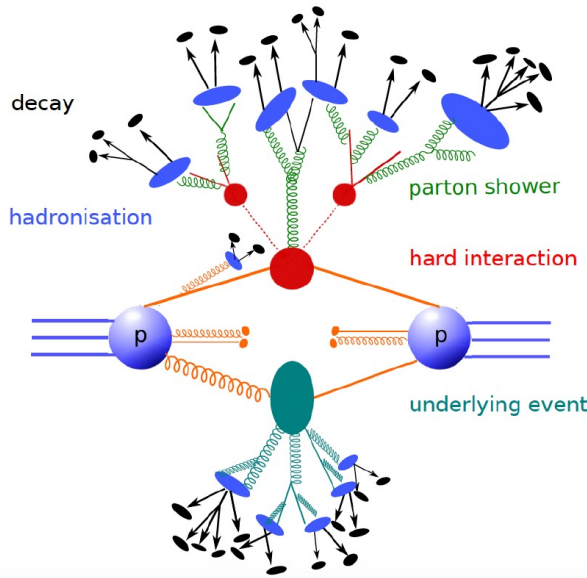


Figure 4.1 – Typical Monte Carlo simulated event with representation of several processes: underlying event, hard scattering, parton shower, hadronisation and decay.

Finally, *pile-up* collisions also overlap, which originate from collisions of other protons in the beam.

For hadronisation, two main models exist, the string model [47] and the cluster model [48]. In the PYTHIA event generator [49] the string model is used whereas the HERWIG event generator [50] uses the cluster model. The differences in performance of these models can be used to assess the uncertainty due to the model chosen.

The output of the MC event generation process is used as an input to a simulation of the ATLAS detector. This simulation describes all of the detector material and geometry, as well as any defects in the material or electrical problems. The simulation is built using the GEANT4 [51] simulation software.

The output of the detector simulation is reconstructed in the exact same way as data to allow the two to be compared directly.

The simulation of the passage of particles through the detector is very computationally expensive. This is mainly due to simulation of the calorimeters because it is extremely time consuming to simulate the particle showers. To speed this up, an approximate simulation, ATLASFAST-II (AFII) [52], is often used. This approximate model simulates the particle showers in the calorimeters using parameterised functions applied to particle energy, rather than carrying out the full shower simulation.

4.2 Object reconstruction

This section describes the main reconstruction and identification criteria applied for each physics objects considered in this analysis (electrons, muons, jets, b -tagged jets and missing transverse momentum).

A summary of the object selections is reported in Table 4.1.

	p_T	$ \eta $	ID	Isolation	Additional cuts
Electrons	$> 15 \text{ GeV}$	< 2.47	MediumLH	PLVTight	$ d_0^{\text{BL}} \text{ significance} < 5$ $ \Delta z_0^{\text{BL}} \sin \theta < 0.5 \text{ mm}$
Muons	$> 15 \text{ GeV}$	< 2.5	Medium	PLVTight	$ d_0^{\text{BL}} \text{ significance} < 5$ $ \Delta z_0^{\text{BL}} \sin \theta < 0.5 \text{ mm}$
Soft Muons	$> 4 \text{ GeV}$	< 2.5	Tight	–	$ d_0 < 3 \text{ mm}$ $ z_0 \sin \theta < 3 \text{ mm}$ $\Delta R(\mu, \text{jet}) < 0.4$
Jets	$> 25 \text{ GeV}$	< 2.5	PFlow	–	JVT
b -jets	$> 25 \text{ GeV}$	< 2.5	DL1r @77 %	–	–

Table 4.1 – Overview of the requirements applied for selecting objects.

4.2.1 Electrons

Electron candidates are reconstructed from energy clusters in the electromagnetic (EM) calorimeter that match a reconstructed track in the inner detector (ID) [53–56]. The clusters are required to be within the range $|\eta| < 2.47$, excluding the transition region between the barrel and endcap calorimeters at $1.37 < |\eta| < 1.52$. Electron candidates must also satisfy a transverse energy requirement of $E_T > 15 \text{ GeV}$.

Further requirements on the electromagnetic shower shape, calorimeter energy to tracker momentum ratio, and other discriminating variables are combined into a likelihood-based object quality cut (LH), optimised for strong background rejection. All electron candidates in this analysis must pass the MediumLH selection.

Electron tracks are also required to be consistent with the beam line applying the requirements: $|d_0^{\text{BL}} \text{ significance}| < 5$ and $|\Delta z_0^{\text{BL}} \sin \theta| < 0.5 \text{ mm}$.

Electrons are further required to be isolated, to reject candidates coming from other sources than prompt W or Z boson decays (hadrons faking an electron signature, heavy-flavour decays or photon conversions).

The isolation working point used in this analysis is PLVTight.

Correction factors are applied to simulated electrons to take into account the small differences in reconstruction, identification and isolation efficiencies between data and MC simulation.

4.2.2 Muons

Muon candidates are reconstructed by combining a reconstructed track from the ID with one from the muon spectrometer (MS) [57], and are required to have $p_T > 15 \text{ GeV}$ and $|\eta| < 2.5$.

The different combinations of input information (from ID and MS) leads to four different types of reconstructed muons:

- **Combined muons (CB):** a combined track is formed reconstructing independently tracks in the ID and MS;
- **Segment-tagged muons (ST):** a track in the ID is classified as a muon if, once extrapolated to the MS, it is associated with at least one local track segment in the MDT or CSC chambers;
- **Calorimeter-tagged muons (CT):** classification for ID tracks that are matched to an energy deposit in the calorimeter and it is compatible to a minimum ionising particle;
- **Extrapolated muons (ME):** the reconstructed trajectory of ME muons uses only the MS track and some loose requirement that its origin is the interaction point;

Muons from Z or W boson decays are considered *prompt* muons whereas those coming from pion or kaon decays are *non-prompt* muons.

This analysis needs the suppression of the contribution from non-prompt muons, therefore requirements are placed on muon candidates.

In CB tracks, the variables commonly used in muon identification are:

- **q/p significance:** defined as the absolute value of the difference between the ratio of the charge and momentum of the muons measured in the ID and MS divided by the sum in quadrature of the corresponding uncertainties;
- ρ' : defined as the absolute value of the difference between the transverse momentum measurements in the ID and the MS divided by the p_T of the combined track;
- χ^2 : normalised χ^2 of the combined track fit.

To reject misidentified muon candidates, primarily originating from pion and kaon decays, several quality requirements can be imposed on the muon candidate.

There are four muon identification working points:

- **Tight Muons:** selected to maximise the purity of muons at the cost of some efficiency. Only CB muons with hits in at least two stations of the MS and satisfying the Medium selection criteria are considered. The reconstruction efficiency for Tight muons in the range $20 < p_T < 100$ GeV is 91.8%.
- **Medium Muons:** this is the default working point used by the ATLAS collaboration. Only CB and ME tracks are used. The CB tracks are required to have 3 hits in at least two MDT layers. The reconstruction efficiency for this working point in the range $20 < p_T < 100$ GeV is 96.1%.
- **Loose Muons:** all CB and ME muons that satisfy the Medium requirement are also included in the Loose selection. It is optimised to maximise the reconstruction efficiency, while still retaining only good quality muon tracks. The reconstruction efficiency for Loose muons in the range $20 < p_T < 100$ GeV is 98.1%.
- **High- p_T Muons:** the selection is optimised for analyses searching for high-mass resonances using muons. CB muons are required to pass the Medium selection and have at least three hits in three MS stations. This selection maximises the momentum resolution for muons with $pT > 100$ GeV

The muon candidates in this analysis must pass the Medium identification definition, already described above.

Muon tracks are also required to be consistent with the beam line applying the requirements: $|d_0^{\text{BL}} \text{ significance}| < 3$ and $|\Delta z_0^{\text{BL}} \sin \theta| < 0.5 \text{ mm}$.

Muons are further required to be isolated and the isolation working point used in this analysis is PLVTight.

Like for electrons, correction factors are applied to simulated muons to account for the small differences between data and simulation.

4.2.3 Soft muons

Different requirements are applied to select and distinguish muons from leptonic decays of the Z and W bosons (referred to as ‘prompt’ or ‘isolated’ muons in the following) and muons from semi-leptonic c-hadron decays (called ‘soft’ or ‘SMT’ muons in the following).

Reconstructed muons with $p_T > 4 \text{ GeV}$ not passing the prompt muon selection can instead be selected as soft muons.

Soft muons are required to pass the Tight quality requirements [58] and to be closer than 0.25 in ΔR within a selected jet. The closest jet to a soft muon is defined as the ‘SMT’ jet.

Very loose requirements are applied on the impact parameters to remove pathological cases: $|d_0| < 3 \text{ mm}$ and $|z_0 \sin \theta| < 3 \text{ mm}$. More details on the soft muon tagging are in Ref. [59].

4.2.4 Jets

Jets are reconstructed using the particle flow algorithm [60].

All jets considered in this analysis should have a transverse momentum $p_T > 25 \text{ GeV}$ and a pseudo-rapidity of $|\eta| < 2.5$.

To suppress jets from in-time pileup, the Jet Vertex Tagger (JVT) discriminant, which is based on a two-dimensional likelihood method, is used [61]. A JVT value of at least 0.59 is required for jets with $p_T < 60 \text{ GeV}$ and $|\eta| < 2.4$, corresponding to an efficiency of 92%.

4.2.5 Soft Muon Tagging

The Soft Muon Tagging (SMT) is a tagging technique for heavy-flavour jets.

It exploits the $b \rightarrow \mu + X$, $b \rightarrow c \rightarrow \mu + X$ and $c \rightarrow \mu + X$ decay chains (with a total $\text{BR} \approx 20\%$), by identifying muons reconstructed inside jets. Those muons are referred to as soft muons and they were described in Section 4.2.3. More details on the soft muon tagging are in Ref. [59].

4.2.6 Recurrent Deep-Learning DL1r

In this analysis the DL1r algorithm is used [62, 63]. It is based on a deep feed-forward neural network (NN) trained using Keras [64] with the Theano [65] backend and the Adam optimiser [66]. The DL1 NN has a multidimensional output corresponding to the probabilities for a jet to be a b-jet, a c-jet or a light-flavour jet. The topology of the output consists of a mixture of fully connected hidden and Maxout layers [67]. The input variables to DL1 consist of those used for the previous official algorithm MV2, with the addition of the JETFITTER c-tagging variables described in Ref. [63].

4.2.6.1 b -tagged jets

Jets originating from bottom quarks (called b -tagged jets) are identified by reconstructing secondary vertices from the tracks associated to the jets and by combining their spatial parameters with life-time related information. In the current analysis the 77 % operation point is used.

Finally, all b -tagged jets considered in this analysis should have a transverse momentum $p_T > 25 \text{ GeV}$ and a pseudo-rapidity of $|\eta| < 2.5$.

4.2.6.2 c -tagged jets

The DL1r_c algorithm also allows to construct DL1r_c discriminant that is used for charm-tagging. They are reconstructed jets satisfying $p_T > 25 \text{ GeV}$ and $|\eta| < 2.5$ requirements, and failing the b -tagging requirement. This search uses the cut operation point giving the c -efficiency of 20% studied and being calibrated in the $t\bar{c}$ +MET SUSY analysis [68].

More details of charm-tagging are given in Chapter C.

4.2.7 Missing transverse momentum

The missing transverse momentum, E_T^{miss} , is a measure of the momentum imbalance, usually due to escaping neutrinos. It is calculated as the magnitude of the negative vector sum of the momenta in the transverse plane of all selected calibrated physics objects in the event [69, 70].

To account for the soft hadronic activity, a soft term built from tracks that are associated to the hard-scatter vertex but are not associated to any of the reconstructed objects. The soft term is included in order to account for low-momentum particles that are not identified among the final state objects [71–73].

It also includes an extra term to account energy losses due to the detector inefficiencies and resolution leading to the mis-measurement of the true transverse energy of the final interacting objects.

4.2.8 Overlap removal

In order to avoid double counting of single final state objects, like e.g. an isolated electron being reconstructed both as an electron and as a jet with the requirements above, a procedure is followed to remove overlaps between final state objects. This is the sequence of operation that are performed to solve these ambiguities, as implemented as the harmonized option [74] in the `AssociationUtils` [75] package:

- Electron candidates which share a track with a muon candidate are removed.
- If the distance in ΔR between a jet and an electron candidate is $\Delta R < 0.2$, then the jet is dropped. If multiple jets are found with this requirement, only the closest one is dropped.
- If the distance in ΔR between a jet and a baseline electron is $0.4 < \Delta R < 0.2$, then the electron is dropped.
- If the distance in ΔR between a jet and a muon candidate is $\Delta R < 0.4$, then: if the jet has more than 2 associated tracks then the muon is dropped, otherwise the jet is removed.

No overlap removal is performed on muons used for the Soft Muon Tagging.

CHAPTER 5

Search for the FCNC decay of top-quark in c-quark and Z boson

This chapter presents a search for the Flavor-Changing-Neutral-Current decay of top-quark in c-quark and Z boson, denoted FCNC tZc.

The study uses a data sample of proton–proton collisions at $\sqrt{s}=13$ TeV recorded in full Run2 (since 2015 to 2018) by the ATLAS experiment, and targets final states with three leptons (either electrons or muons).

I took in charge most of the analysis, from the event selection up to the final results.

5.1 Physics motivation

The heaviest particle in the Standard Model (SM), the top quark, decays almost exclusively to a W-boson and a bottom quark [76]. In proton–proton (pp) collisions, top quarks are produced dominantly in pairs, via the strong interaction, but also singly, via the electroweak interaction.

Within the SM, flavour changing neutral currents (FCNC) processes are forbidden at tree level due to the Glashow-Iliopoulos-Maiani mechanism [5] (see Section 1.1.2.1) and the approximate diagonality of the Cabibbo-Kobayashi-Maskawa matrix [76] causes the suppression of such processes at higher orders (see Section 1.1.2.2).

Nonetheless, there are several scenarios beyond the Standard Model (BSM) that can significantly enhance the FCNC processes in the top quark sector, opening a door for its detection at the Large Hadron Collider (LHC) [6, 21–24, 27] and some of them are already discussed in Section 1.3.

The analysis presented in the following searches for FCNC tZc processes. A comparison between SM and BSM models predictions for the branching ratios of top quark decays to an up or a charm quark and a Z boson is shown in Table 5.1.

Model:	SM	QS	2HDM	FC 2HDM	MSSM	RPV SUSY	RS	EMF
$\mathcal{B}(t \rightarrow qZ)$	10^{-14}	10^{-4}	10^{-6}	10^{-10}	10^{-7}	10^{-6}	10^{-5}	10^{-6}

Table 5.1 – Maximum allowed FCNC $t \rightarrow qZ$, ($q = u, c$) branching ratios predicted by several models[19–26].

The search for FCNC tZc processes can be performed by analysing the top quark decays in $t\bar{t}$ events as well as the production of single-top quarks (see Figure 5.1). In the former channel, one of the top quarks decays through FCNC and the other through the dominant mode ($t \rightarrow Wb$). The latter channel is characterised by a final state composed of a single top quark and a Z boson. The main difference between the final state of decay and production modes is the presence of one additional jet.

The analysis presented in the following targets both production and decay mode. This search is done using pp collision data collected by the ATLAS detector at a centre-of-mass energy of 13 TeV and corresponding to an integrated luminosity of 139 fb^{-1} .

The analysis targets both events with the production of a Z boson and a single-top quark decaying to a W boson and a b-quark and events with the production of top quark pairs, where one top quark decays to a Z boson and a charm quark and the other top quark decays to a W boson and a b-quark. For both modes, the Z boson decays into two charged leptons (electrons or muons including those coming from leptonic τ -lepton decays) and the W boson from the top quark decays leptonically too.

In a model independent way, the anomalous couplings can be described by the so called effective field theory (EFT). This theory considers an extension of the SM Lagrangian \mathcal{L}_{SM} by operators in higher-dimensions of the mass suppressed by the scale of new physics Λ as shown in Equation (5.1). Dimension-5 operators are not considered in this analysis due to the introduction of lepton-flavour violating processes. Therefore, the anomalous couplings can be approximated with dimension-6 operators $O_i^{(6)}$ whose strength is given by the Wilson coefficients $C_i^{(6)}$.

$$\mathcal{L} = \mathcal{L}_{SM} + \frac{1}{\Lambda^2} \sum_i C_i^{(6)} O_i^{(6)} \quad (5.1)$$

Experimental limit on the branching ratio of FCNC tZc decay was previously established by experiments at the Large Electron-Positron Collider (LEP) [77–80], the Hadron-Electron Ring Accelerator (HERA) [81], the Tevatron [10, 82] and the Large Hadron Collider (LHC) [83–85]. The ATLAS and the CMS collaborations obtained limits at the 95 % confidence level (CL) for this process using data collected at $\sqrt{s}=13 \text{ TeV}$ and $\sqrt{s}=8 \text{ TeV}$, focusing on FCNC top-quark decays [83, 84], or both production and decay modes combined [85]. A summary of the ATLAS and CMS results on the limits on FCNC couplings is shown in Figure 5.2. The actual observed limits on the FCNC tZc coupling from ATLAS is $\text{BR}(t \rightarrow cZ) < 2.4 \times 10^{-4}$ [83].

Recent studies were done on the interference effects on the tZl and $t\gamma q$ anomalous couplings, concluding that these effects are smaller than the variations of the systematics uncertainties considered [86]. Therefore, both decay and production modes are taken into account in this analysis to improve the results on the limit for tZc anomalous coupling.

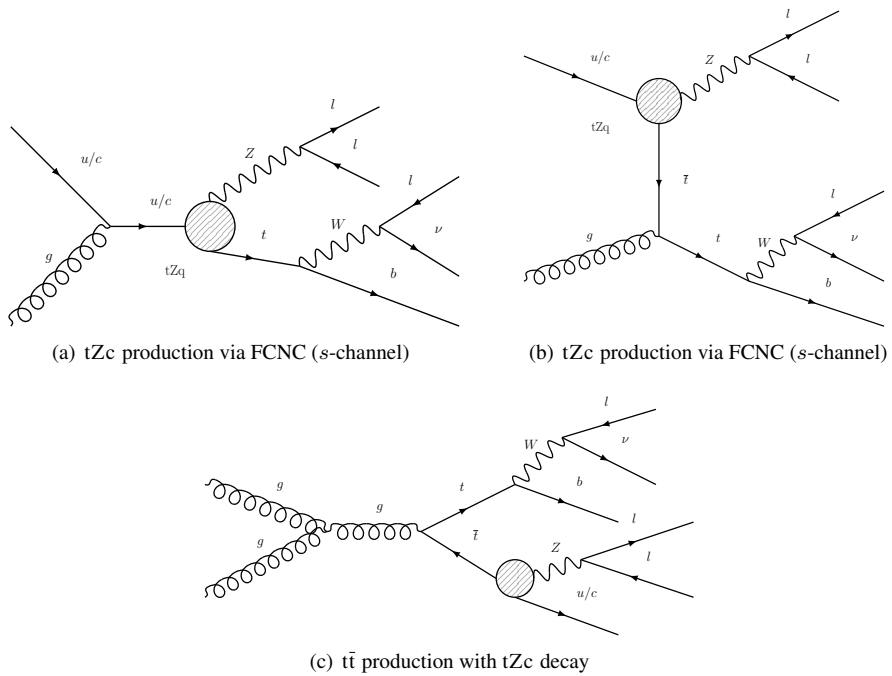


Figure 5.1 – Examples of lowest order Feynman diagrams for tZc production via FCNC in (a) the *s*-channel and (b) the *t*-channel. Example of the lowest order Feynman diagrams for (c) $t\bar{t}$ production, with one top-quark decaying through the SM and the other via tZc . The vertex labelled as tZq corresponds to the coupling responsible for the FCNC interaction.

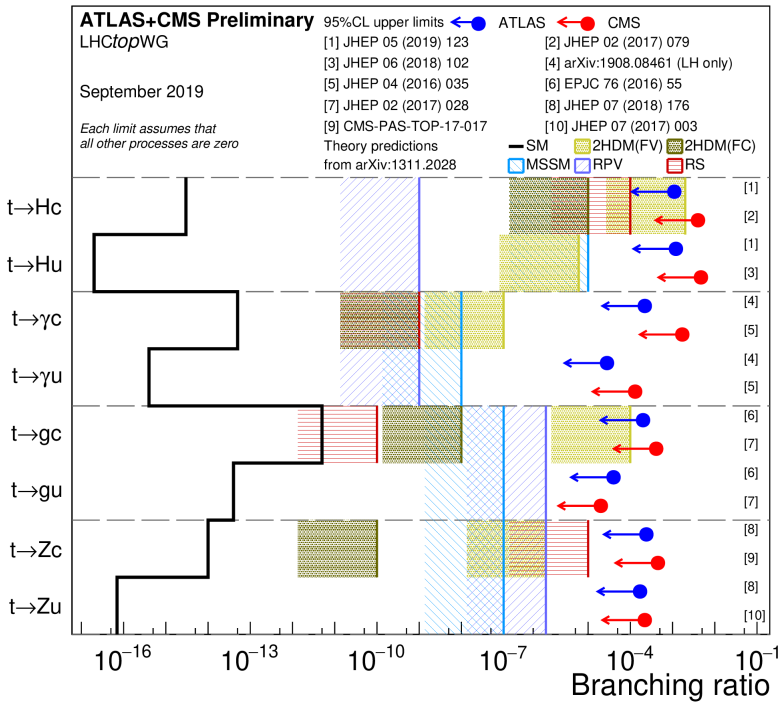


Figure 5.2 – Summary of the current 95% confidence level observed limits on the branching ratios of the top quark decays via flavour changing neutral currents to a quark and a neutral boson $t \rightarrow Xq$ ($X = g, Z, \gamma$, or H ; $q = u$ or c) by the ATLAS and CMS Collaborations compared to several new physics models. The ATLAS limits on $t \rightarrow q$ are valid for the case of a purely left-handed coupling. Status of figure: September 2019 (Top2019)

5.2 Analysis strategy

In the following, the analysis strategy is described.

Analysis motivation and overview The analysis presented in the following searches for flavour-changing neutral current (FCNC) coupling between the top-quark and the Z boson in proton–proton collisions at $\sqrt{s} = 13\text{ TeV}$ with the ATLAS detector. The search is carried out in both single-top quark production and top-quark pair-production events. In addition, to increase the sensitivity to FCNC tZc coupling, the Soft Muon Tagging (SMT) technique is exploited for the semi-leptonic decays of c-hadrons produced by the FCNC top decay.

Dataset Data from the full Run2 is used, 139 fb^{-1} .

The description of the data sample and of the Monte Carlo samples can be found in Section 5.3.

Signal regions The analysis focuses on the trilepton final state.

Three SRs are defined for the tZc coupling extraction, targeting:

- FCNC tZc in $t\bar{t}$ decays (called SR1tZc),
- FCNC tZc in single-top production (called SR2tZc),
- FCNC tZc in $t\bar{t}$ decays using the SMT technique (called SR3tZc).

The SRs for each coupling extraction are orthogonal between each other. The orthogonality is assured by selecting events with different jet multiplicities and by selecting or vetoing the presence of a jet associated to a soft muon.

This thesis main focus on the Soft Muon Tagging technique used as charm tagger and therefore on the definition of SR3tZc, reported in Section 6.1.

The description of the other SRs selections, used for the combined fit to extract expected limits, are reported in Section 7.1.

The DL1r_c technique is also investigated as an alternative to SMT and described in Section 6.4.

Background estimation The main background sources are:

- for SR1tZc, $t\bar{t}Z$ and $VV + \text{HF}$;
- for SR2tZc, $VV + \text{HF}$ and Standard Model tZq;
- for SR3tZc, $t\bar{t}Z$ and $VV + \text{HF}$.

All backgrounds are estimated using Monte Carlo samples. They are normalised to the theoretical cross-sections. The normalisation of the $t\bar{t}$ background is left free floating in the fits. Various control regions (CRs) are included in the fits to control the background normalisations. For the fit, a total of four CRs is used. The description of the background sources and the CR selections is reported in Section 6.2.

Separation of signal and backgrounds A multivariate analysis is used to improve the discrimination of signal to background events providing SRs with increased $\frac{S}{\sqrt{B}}$. Gradient Boosted Decision Trees (GBDTs) are trained separately for each SR.

The description of the multivariate analysis can be found in Section 6.3.

Fit and limit extraction To extract limits on the FCNC tZc coupling, the output of the GBDT in the SRs are simultaneously fit, together with other distributions in the CRs. The description of the fit and of the extraction of the limits can be found in Chapter 8.

Blinding strategy A blinding strategy is set to reduce any possible bias in the measurement. The prescriptions of the Top WG are followed [87]. To make sure that the background sources are correctly described, data is only looked at in regions where the signal contribution is expected to be small.

5.3 Data and Monte Carlo samples

This section describes the samples used in this analysis. The detailed lists of data and Monte Carlo (MC) samples can be found in Appendix A, while a description is presented below.

The starting point for the analysis are the ROOT ntuples, produced using the AnalysisBase-21.2.127 version, starting from TOPQ1 derivations [88]. The derivations contain a filter that requires at least one lepton (an LH loose electron or a good combined muon) with a p_T above 20 GeV and $|\eta| \leq 2.5$.

5.3.1 Data sample

The analysis described in this paper uses data collected from 2015 to 2018 by the ATLAS detector at a centre-of-mass energy of 13 TeV. The complete sample includes all 25 ns data periods from 2015, as well as the whole 2016–2018 datasets. The total integrated luminosity is of 139 fb^{-1} . The selected data periods were collected during stable beam LHC operations and with the ATLAS detector fully functioning. The partial integrated luminosities and the Good Run Lists used are reported in table 5.2.

Year	Int. lumi. (fb^{-1})	GRL
2015	3.2	data15_13TeV/20170619/physics_25ns_21.0.19.xml
2016	33.0	data16_13TeV/20170605/physics_25ns_21.0.19.xml
2017	44.3	data17_13TeV/20180619/physics_25ns_Triggerno17e33prim.xml
2018	58.5	data18_13TeV/20181111/physics_25ns_Triggerno17e33prim.xml

Table 5.2 – Integrated luminosity per year.

Events are considered only if they are accepted by at least one of the single-muon or single-electron triggers described in Refs. [89–92] and listed in section 5.3.1.

The ATLAS trigger system is composed by two levels: the first level (L1) is a hardware trigger implemented in custom-built electronics, while the second level, referred to as high level trigger (HLT), is software based.

The electron triggers select a calorimeter cluster matched to a track. Electrons must then satisfy identification criteria based on a multivariate technique using a likelihood (LH) discriminant. In 2015, electrons had to satisfy a medium identification and have $E_T > 24 \text{ GeV}$. In 2016–2018, electrons had to satisfy a tight identification together with an isolation criteria and have $E_T >$

Year	Single e	Single μ
2015	HLT_e24_lhmedium_L1EM20VH HLT_e60_lhmedium HLT_e120_lhloose	HLT_mu20_iloose_L1MU15 HLT_mu50
2016–2018	HLT_e26_lhtight_nod0_ivarloose HLT_e60_lhmedium_nod0 HLT_e140_lhloose_nod0	HLT_mu26_ivarmedium HLT_mu50

Table 5.3 – Trigger selections.

26 GeV. During the four years, to avoid efficiency losses due to identification and isolation at high p_T , two other triggers were also available, selecting medium electrons with $E_T > 60$ GeV and selecting loose electrons with $E_T > 120$ GeV (140 GeV in 2016–2018).

Muons are triggered on by matching tracks reconstructed in the muon spectrometer and in the inner detector. In 2015, muons had to satisfy a loose isolation requirement and have $p_T > 20$ GeV. In 2016–2018, the isolation criterion was tightened and the threshold increased to $p_T > 26$ GeV. During the four years, to avoid efficiency losses due to isolation at high p_T , another muon trigger without any isolation requirement was available, selecting muons with $p_T > 50$ GeV.

5.3.2 Monte Carlo simulated samples

ATLAS Monte Carlo samples for analyses on the 2015–2018 dataset are split into three subsets: mc16a reflects the pile-up conditions of the years 2015 and 2016, mc16d reflects the pile-up conditions of 2017 data and mc16e reflects the pile-up conditions of 2018 data. Therefore, mc16a samples need to be scaled to 2015+2016 integrated luminosity, mc16d samples need to be scaled to 2017 integrated luminosity and mc16e samples need to be scaled to the 2018 integrated luminosity. The generated MC samples containing top-quarks are produced with the top-quark mass, m_t , parameter set to 172.5 GeV and a branching fraction of the top-quark decay to a W boson and a b quark of 1. In all samples, decays into τ leptons are included and if the τ decays leptonically such events are taken into account in the analysis.

In the following, samples used in the analysis are explained in detail, both for the signal and for the background sources.

5.3.2.1 Signal samples

The Monte Carlo simulation samples for signal were generated at next-to-leading-order (NLO) with MADGRAPH5_aMC@NLO [93] interfaced to the PYTHIA8 [94] with the A14 tune [95] and NNPDF2.3LO PDF set. Only decays of the W and Z bosons involving charged leptons were generated at the matrix element level ($Z \rightarrow e^+e^-$, $\mu^+\mu^-$, $\tau^+\tau^-$ and $W \rightarrow e\nu, \mu\nu, \tau\nu$). For the matrix element, PDF set NNPDF3.0NLO is used. The Universal FeynRules Output (UFO) model [96] is used for computation at the NLO in QCD. Top quark FCNC decay is done by TopFCNC model [97, 98]. The TopFCNC UFO model includes the effects of new physics at a energy scale Λ by adding effective terms to the SM lagrangian:

$$\mathcal{L} = \mathcal{L}_{SM} + \mathcal{L}^{eff} = \mathcal{L}_4 + \frac{1}{\Lambda^2} \mathcal{L}_6 + \dots \quad (5.2)$$

where $\mathcal{L}_4 = \mathcal{L}_{SM}$ and \mathcal{L}_6 contains operators with dimension-six. The rest of the terms contain operators of dimension higher than 6 and will be suppressed due to the associated factors $1/\Lambda^4, \dots$. \mathcal{L}_6 can be written as a linear combination of dimension-six operators O_j :

$$\mathcal{L}_6 = \sum_j C_j O_j \quad (5.3)$$

with C_j being complex constants and O_j being SM gauge invariant dimension-six operators that contain the fermion doublets and singlets, the gauge field tensors, the Higgs doublet and the covariant derivatives.

Taking into account that both production and decay modes are considered in this analysis, separated samples for each mode and for tZc (using IC_{ctB} and IC_{ctW}) anomalous coupling were generated. In order to allow the study of the chirality of these couplings, samples with left-handed or right-handed couplings were obtained as well but not considered in this thesis. Finally, an additional sample for $t\bar{t}$ production was generated including a soft muon filter targeting the charm-tagging signal region.

Therefore, three different signal samples are considered:

- tZ production for tZc left-handed coupling;
- $t\bar{t}$ production for tZc left-handed coupling;
- $t\bar{t}$ production with soft muon tagging for tZc left-handed coupling.

For the signal samples with $t\bar{t}$ production, it is considered that one of the top-quarks decays through FCNC to cZ and the other, according to the SM, to bW .

For the tZ production, a top-quark and a Z boson is generated, where the top-quark decays according to the SM, since the tZq anomalous coupling is assumed in the primary vertex. The number of signal events is normalised to a branching ratio of

$$\mathcal{B}(t \rightarrow cZ) = 2.4 \times 10^{-4}, \text{ constraining } \mathcal{B}(t \rightarrow bW) = 1 - \mathcal{B}(t \rightarrow cZ).$$

The FCNC $t\bar{t}$ decay signal is normalised using the $t\bar{t}$ cross-section prediction at next-to-next-to-leading order (NNLO) in QCD including the re-summation of next-to-next-to-leading logarithmic (NNLL) soft-gluon terms calculated using TOP++2.0 [99–105]. For proton–proton collisions at a centre-of-mass energy of $\sqrt{s} = 13$ TeV, this cross section corresponds to $\sigma(t\bar{t})_{\text{NNLO+NNLL}} = 832 \pm 51$ pb using a top-quark mass of

$$m_t = 172.5 \text{ GeV}.$$

The uncertainties on the cross-section due to PDF and α_s are calculated using the PDF4LHC prescription [106] with the MSTW2008 68% CL NNLO [107, 108], CT10 NNLO [109, 110] and NNPDF2.3 5f FFN [111] PDF sets, and are added in quadrature to the scale uncertainty. The FCNC single-top quark production signal normalisation cross-section is calculated at NLO using the TopFCNC model as implemented in the MADGRAPH5_aMC@NLO .

The considered value of the $t \rightarrow cZ$ branching ratio is the observed limit obtained from the previous analysis at a center-of-mass energy of 13 TeV with 36 fb^{-1} [83].

5.3.2.2 Background samples

Simulated samples are included in the analysis in order to account for all the SM predicted background channels. The samples are normalised to the cross-sections given in Appendix A multiplied by the k factors given in the same tables.

The descriptions below are taken from the reference document by the PMG group.

$t\bar{t}$ production The production of $t\bar{t}$ events is modelled using the POWHEGBOX [112–115] v2 generator at NLO with the NNPDF3.0NLO [116] parton set of distribution functions (PDF) and the h_{damp} parameter¹ set to $1.5 m_t$ [117]. The events are interfaced to PYTHIA8.230 [118] to model the parton shower, hadronisation, and underlying event, with parameters set according to the A14 tune [119] and using the NNPDF2.3LO set of PDFs [111]. The decays of bottom and charm hadrons are performed by EVTGEN v1.6.0 [120]. In the sample used (DSID: 410472), it is required that both the W bosons from the t quarks decay leptonically.

The impact of the parton shower and hadronisation model is evaluated by comparing the nominal generator setup with a sample (DSID: 410558) produced with the POWHEGBOX [112–115] v2 generator using the NNPDF3.0NLO [116] parton distribution function (PDF). The events are interfaced with HERWIG7.04 [121, 122], using the H7UE set of tuned parameters [122] and the MMHT2014LO PDF set [123]. The decays of bottom and charm hadrons are simulated using the EVTGEN v1.6.0 program [120]. The Var3c A14 tune variation [119], that largely corresponds to the variation of α_s for initial state radiation (ISR) in the A14 tune, is considered as an uncertainty. The impact of final-state-radiation (FSR) is evaluated using PS weights which vary the renormalisation scale for QCD emission in the FSR by a factor of 0.5 and 2.0, respectively. Additionally, the uncertainty associated to the h_{damp} parameter is evaluated using the alternative sample (DSID: 410482) with the h_{damp} value increased to $3.0 m_t$.

$t\bar{t}V$ production The production of $t\bar{t}V$ events (DSID: 410155–410157, 410218–410220 and 410276–410278) is modelled using the MADGRAPH5_AMC@NLO v2.3.3 [93] generator at NLO with the NNPDF3.0NLO [116] parton distribution function (PDF). The events are interfaced to PYTHIA8.210 [118] using the A14 tune [119] and the NNPDF2.3LO [116] PDF set. The decays of bottom and charm hadrons are simulated using the EVTGEN v1.2.0 program [120].

The uncertainty due to initial-state-radiation (ISR) is estimated by comparing the nominal $t\bar{t}V$ sample with two additional samples (DSID: 410370–410375), which have the same setting as the nominal one, but with the Var3 up or down variation of the A14 tune. The Var3c A14 tune variation corresponds to the variation of α_s for initial state radiation (ISR) in the A14 tune.

Additional $t\bar{t}V$ samples (DSID: 410142) are produced with the SHERPA 2.2.0 [124] generator at LO accuracy, using the MEPS@LO setup [125, 126] with up to one additional parton for $t\bar{t}\ell\ell$ sample and two additional partons for the others. A dynamic renormalization scale is used and it is defined similarly to that of the nominal $t\bar{t}V$ samples. The CKKW matching scale of the additional emissions is set to 30 GeV. The default SHERPA 2.2.0 parton shower is used along with the NNPDF3.0NNLO [116] PDF set.

tZq production The production of tZq events is modelled using the MADGRAPH5_AMC@NLO v2.3.3 [93] generator at NLO with NNPDF3.0NLO [116] parton distribution function (PDF) (DSID: 412063). The events are interfaced with PYTHIA8.230 [118] using the A14 tune [119] and the NNPDF2.3LO [116] PDF set.

The uncertainty due to initial-state-radiation (ISR) is estimated by comparing the nominal tZq sample with two additional samples (DSID: 412064–412065), which have the same setting as the nominal one, but with the Var3 up and down variations of the A14 tune. The predicted cross-section was calculated with MADGRAPH5_aMC@NLO 2.6.0, using the five-flavour scheme with

¹The h_{damp} parameter is a re-summation damping factor and one of the parameters that controls the matching of Powheg matrix elements to the parton shower and thus effectively regulates the high- p_T radiation against which the $t\bar{t}$ system recoils.

the NNPDF30_NLO_AS_0118 PDF set and with the renormalization and factorisation scales, μ_R and μ_F , set to $\mu_R = \mu_F = (m_t + m_Z)/4 = 66$ GeV. The SM tZq cross-section at NLO in QCD, including non-resonant contributions with $m_{\ell^+ \ell^-} > 30$ GeV, is 102 fb.

tW production Although having a very low contribution, single top-quark production is also considered. The associated production of top-quarks with W bosons (tW) is modelled using the POWHEGBOX [113–115, 127] v2 generator at NLO in QCD using the five-flavour scheme and the NNPDF3.0NLO set of PDFs [116]. The diagram removal (DR) scheme [128] is used to remove interference and overlap with $t\bar{t}$ production.

The events are interfaced to PYTHIA8.230 [118] using the A14 tune [119] and the NNPDF2.31o set of PDFs [111]. In the samples used (DSIDs: 410648 and 410649), it is required that both W bosons in the event decay leptonically.

tWZ production The production of tWZ events is modelled using the MADGRAPH5_AMC@NLO v2.3.3 [93] generator at NLO with NNPDF3.0NLO [116] parton distribution function (PDF). The events are interfaced with PYTHIA8.212 [118] using the A14 tune [119] and the NNPDF2.3LO [116] PDF set. The decays of bottom and charm hadrons are simulated using the EVTGEN v1.2.0 program [120]. In the sample used (DSID: 410408), it is required that the Z boson decays leptonically.

An additional tWZ sample is used to estimate the uncertainty connected with the description of the interference between $t\bar{t}Z$ and tWZ. The nominal samples is generated with the DR1 scheme, while the alternative sample is generated using the DR2 scheme (DSID: 412119).

Diboson production The samples simulating WW, WZ and ZZ events with at least two charged leptons are all considered. In the trilepton topology, WZ events are the ones that significantly contribute to the background.

Samples of diboson final states (VV) are simulated with the SHERPA v2.2.1 or v2.2.2 [124] generator depending on the process, including off-shell effects and Higgs-boson contributions, where appropriate. Fully leptonic final states and semi-leptonic final states, where one boson decays leptonically and the other hadronically, are generated using matrix elements at NLO accuracy in QCD for up to one additional parton and at LO accuracy for up to three additional parton emissions (DSID: 364250, 364253-364255). Samples for the loop-induced processes $gg \rightarrow VV$ are generated using LO-accurate matrix elements for up to one additional parton emission for both cases of fully leptonic and semi-leptonic final states (DSID: 345705-345706). The matrix element calculations are matched and merged with the SHERPA parton shower based on Catani-Seymour dipole [129, 130] using the MEPS@NLO prescription [125, 126, 131, 132]. The virtual QCD correction are provided by the OPENLOOPS library [133, 134]. The NNPDF3.0nnlo set of PDFs is used [116], along with the dedicated set of tuned parton-shower parameters developed by the SHERPA authors.

Electroweak production of diboson in association with two jets ($VVjj$) is simulated with the SHERPA v2.2.2 [124] generator (DSID: 364283-364284). The LO-accurate matrix elements are matched to a parton shower based on Catani-Seymour dipoles [129, 130] using the MEPS@LO prescription [125, 126, 131, 132].

Samples are generated using the NNPDF3.0nnlo set [116], along with the dedicated set of tuned parton-shower parameters developed by the SHERPA authors.

To assess the uncertainty from the generator, alternative samples are used.

The PowhegBox v2 [113–115] generator is used to generate these alternative WW , WZ and ZZ samples [135] processes at NLO-accuracy in QCD. The effect of singly resonant amplitudes as well as the interference effects due to Z/γ^* and identical leptons in the final state is included, where appropriate.

Events are interfaced to PYTHIA8.186 [94] for the modelling of the parton shower, hadronisation, and underlying event, with parameters set according to the AZNLO tune [136]. The CT10 PDF set [109] is used for the hard-scattering processes, whereas the CTEQ6L1 PDF set [137] is used for the parton shower. The EVTGEN v1.2.0 program [120] is used to decay bottom and charm hadrons.

Z+jets production The POWHEGBOX v1 MC generator [113–115, 138] is used for the simulation at NLO accuracy of the hard-scattering processes of Z -boson production and decay in the electron, muon, and tau channels. It is interfaced to PYTHIA8.186 [94] for the modelling of the parton shower, hadronisation, and underlying event, with parameters set according to the AZNLO tune [136]. The CT10 PDF set [109] is used for the hard-scattering processes, whereas the CTEQ6L1 PDF set [137] is used for the parton shower. The effect of QED final-state radiation is simulated with Photos++ (v3.52) [139, 140]. The EVTGEN v1.2.0 program [141] is used to decay bottom and charm hadrons.

$t\bar{t}H$ production The production of $t\bar{t}H$ events is modelled using the POWHEGBOX v2 [112–115, 142] generator which provides matrix elements at next-to-leading order (NLO) in the strong coupling constant α_S in the five-flavour scheme with the NNPDF3.0nlo [116] PDF set. The functional form of the renormalisation and factorisation scale is set to $\sqrt[3]{m_T(t) \cdot m_T(\bar{t}) \cdot m_T(H)}$. The events are interfaced to PYTHIA8.230 [118] using the A14 tune [119] and the NNPDF2.3lno [116] PDF set. The decays of bottom and charm hadrons are performed by EVTGEN v1.6.0 [141].

Other rare backgrounds The production of triboson (VVV) events is simulated with the SHERPA v2.2.2 [124] generator using factorised gauge boson decays. Matrix elements, accurate at NLO for the inclusive process and at LO for up to two additional parton emissions, are matched and merged with the SHERPA parton shower based on Catani-Seymour dipole factorisation [129, 130] using the MEPS@NLO prescription [125, 126, 131, 132]. The virtual QCD correction for matrix elements at NLO accuracy are provided by the OPENLOOPS library [133, 134].

Samples are generated using the NNPDF3.0nnlo set [116], along with the dedicated set of tuned parton-shower parameters developed by the SHERPA authors.

The production of $t\bar{t}tt$ is modelled using the MADGRAPH5_AMC@NLO v2.3.3 [93] generator at NLO with the NNPDF3.1nlo [116] parton distribution function (PDF). The events are interfaced with PYTHIA8.230 [118] using the A14 tune [119] and the NNPDF2.3lno [116] PDF set.

The decays of bottom and charm hadrons are simulated using the EVTGEN v1.6.0 program [141]. The other rare top quark processes namely the production of $t\bar{t}W$ W and $t\bar{t}t$ are all modeled using the MADGRAPH5_AMC@NLO generator at LO interfaced with PYTHIA8 using the A14 tune.

CHAPTER 6

FCNC tZc with charm-tagging

This chapter presents an important fraction of my work was dedicated to the event selection using the SMT technique, the charm-tagger DL1r_c and the comparison between these two techniques. The design and optimization of the multivariate analysis is also part of my work and it will be presented in this chapter.

6.1 Event selections and reconstruction

The channel studied for this work is FCNC tZc in $t\bar{t}$ decays using Soft Muon Tagging. One of the t-quarks decays following the SM into a W boson and a b-quark (called in the following *SM top*), while the other t-quark (called in the following *FCNC top*) decays into a Z boson and a c-quark that subsequently decays semi-leptonically.

This semi-leptonic decay is tagged using the Soft Muon Tagging (SMT) technique.

Only the trileptonic channel is considered, i.e. the Z boson from the FCNC top decays leptonically and the W boson from the SM top decays leptonically.

Therefore the final state is characterised by the presence of three leptons, an SMT-jet, a b-tagged jet and missing transverse momentum from the escaping neutrinos.

The final states where either the Z or the W bosons decay hadronically were not considered because of the higher backgrounds.

The pre-selection criteria, common to all the Signal Regions used in this work, are the following:

- Exactly three leptons (electrons or muons) required.

These leptons must satisfy the requirements described in sections 4.2.1 and 4.2.2. At least one lepton must have $p_T > 27 \text{ GeV}$. The other two leptons must have $p_T > 15 \text{ GeV}$. Events with a fourth lepton with $p_T > 15 \text{ GeV}$ are vetoed.

- There should be at least one opposite-sign same-flavour lepton pair (OSSF) with an invariant mass in the range $|m_{\ell\ell} - 91.2 \text{ GeV}| < 15 \text{ GeV}$.

These two leptons are considered as the ones coming from the Z boson.

If more than one lepton pair satisfy these selections, the pair with the invariant mass closest to the mass of the Z boson is considered.

6.1.1 Top quarks reconstruction

In the events having at least two jets with one of them being b-tagged, two top quarks (FCNC and SM tops) candidates are reconstructed under the FCNC $t\bar{t}$ decay signal hypothesis. The kinematics of the top-quark candidates can be reconstructed from the corresponding decay particles.

The reconstructed Z boson is assumed to come from the FCNC top decay ($t \rightarrow cZ$), while b-tagged jet from SM top decay ($t \rightarrow bW$).

In order to reconstruct both top quarks, further we need to associate a reconstructed jet to the c-quark from FCNC top decay, and reconstruct the W boson from the SM top decay. This can be done by assuming the lepton not used to reconstruct the Z boson to be the one coming from the W boson decay, the missing transverse momentum to be the transverse momentum of the neutrino from W boson decay and determining longitudinal component of the neutrino momentum (p_z^ν) using the minimisation of the following expression for each jet combination:

$$\chi^2_{t\bar{t}} = \frac{(m_{j_a\ell\ell}^{\text{reco}} - m_{t_{\text{FCNC}}})^2}{\sigma_{t_{\text{FCNC}}}^2} + \frac{(m_{j_b\ell_W\nu}^{\text{reco}} - m_{t_{\text{SM}}})^2}{\sigma_{t_{\text{SM}}}^2} + \frac{(m_{\ell_W\nu}^{\text{reco}} - m_W)^2}{\sigma_W^2}, \quad (6.1)$$

where $m_{j_a\ell\ell}^{\text{reco}}$, $m_{j_b\ell_W\nu}^{\text{reco}}$, and $m_{\ell_W\nu}^{\text{reco}}$ are the reconstructed masses of the cZ , bW , and $\ell_W\nu$ systems, respectively. For each jet combination, where any jet can be assigned to j_a , while j_b must correspond to a b-tagged jet, the $\chi^2_{t\bar{t}}$ minimisation gives the most probable value for p_z^ν . From all combinations, the one with the minimum χ^2 is chosen. For each event that contains at least one soft muon, the SMT-jet must be assigned to j_a or j_b , depending on the χ^2 . In Equation (6.1), the central value for the masses and the widths of the top quarks and W boson are taken from reconstructed simulated FCNC $t\bar{t}$ decay signal events. This is done by matching the true c- and b-quarks in the simulated events to the reconstructed ones, setting the longitudinal momentum of the neutrino to the p_z of the true simulated neutrino and then performing Bukin fits¹ [143] to the masses of the reconstructed top quarks and W boson (more details are in Chapter B).

The values are:

- $m_{t_{\text{FCNC}}} = 171.2 \text{ GeV}$, $\sigma_{t_{\text{FCNC}}} = 11.4 \text{ GeV}$;
- $m_{t_{\text{SM}}} = 168.0 \text{ GeV}$, $\sigma_{t_{\text{SM}}} = 23.9 \text{ GeV}$;
- $m_W = 82.6 \text{ GeV}$, $\sigma_W = 16.6 \text{ GeV}$.

¹These fits use a piecewise function with a Gaussian function in the centre and two asymmetric tails. Five parameters determine the overall normalization, the peak position, the width of the core, the asymmetry, the size of the lower tail, and the size of the higher tail. From these parameters, only the peak position and the width enter the χ^2 .

6.1.2 Signal Region with SMT definition

The SR3tZc has the following additional requirements:

- At least two jets satisfying the requirements described in Section 4.2.4.
- Zero, one or two b-jets satisfying the requirements in Section 4.2.6.1.
- The selected soft muon must be opposite-sign with the lepton coming from W boson also satisfying the requirements described in Section 4.2.3 .
- At least one SMT jet described in Section 4.2.5.
- No requirements on the masses of both the FCNC and the SM top-quark candidates are applied.

This selection is summarized in Table 6.1.

SR3tZc using SMT
Exactly 3 leptons with $ \eta < 2.5$ and $p_T(\ell_1) > 27 \text{ GeV}$, $p_T(\ell_2) > 15 \text{ GeV}$, $p_T(\ell_3) > 15 \text{ GeV}$ ≥ 1 OSSF pair, with $ m_{\ell\ell} - 91.2 \text{ GeV} < 15 \text{ GeV}$ ≥ 2 jets with $ \eta < 2.5$ ≤ 2 b-jets $\text{OS}(\mu^{soft}, \ell_W)$ ≥ 1 SMT jet

Table 6.1 – Overview of the requirements applied for selecting events in the Signal Region with SMT

The event yield for each b-jet multiplicities and the total event yield is shown in Table 6.2. Even though the selection with exactly one b-jet is the purest, for the SR3tZc, events containing zero and two b-jets are also considered in order to have the largest possible signal acceptance and then work on the separation of signal from background, as described in Section 6.3.

Figures 6.1 and 6.2 show the distributions of kinematic variables for events selected in the SR3 region for the tZc coupling extraction selection (SR3tZc). As it can be noticed, the main background sources are $t\bar{t}Z$ and $VV + \text{HF}$.

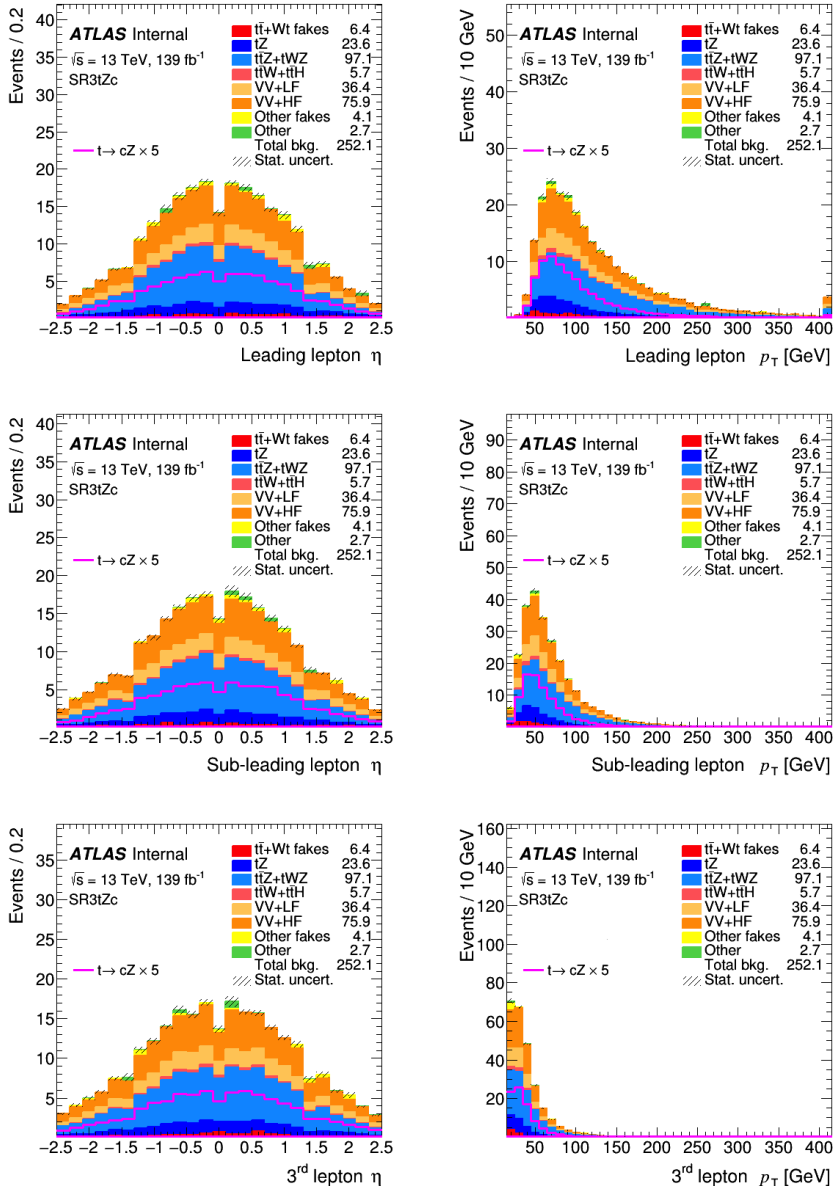


Figure 6.1 – Pre-fit distributions of kinematic variables of leptons for events selected in the SR3tZc region. Number of signal events are normalised to the current observed branching ratio limits and scaled by factor 5. The uncertainty band includes only the statistical uncertainty. These distributions are blinded, following the blinding strategy.

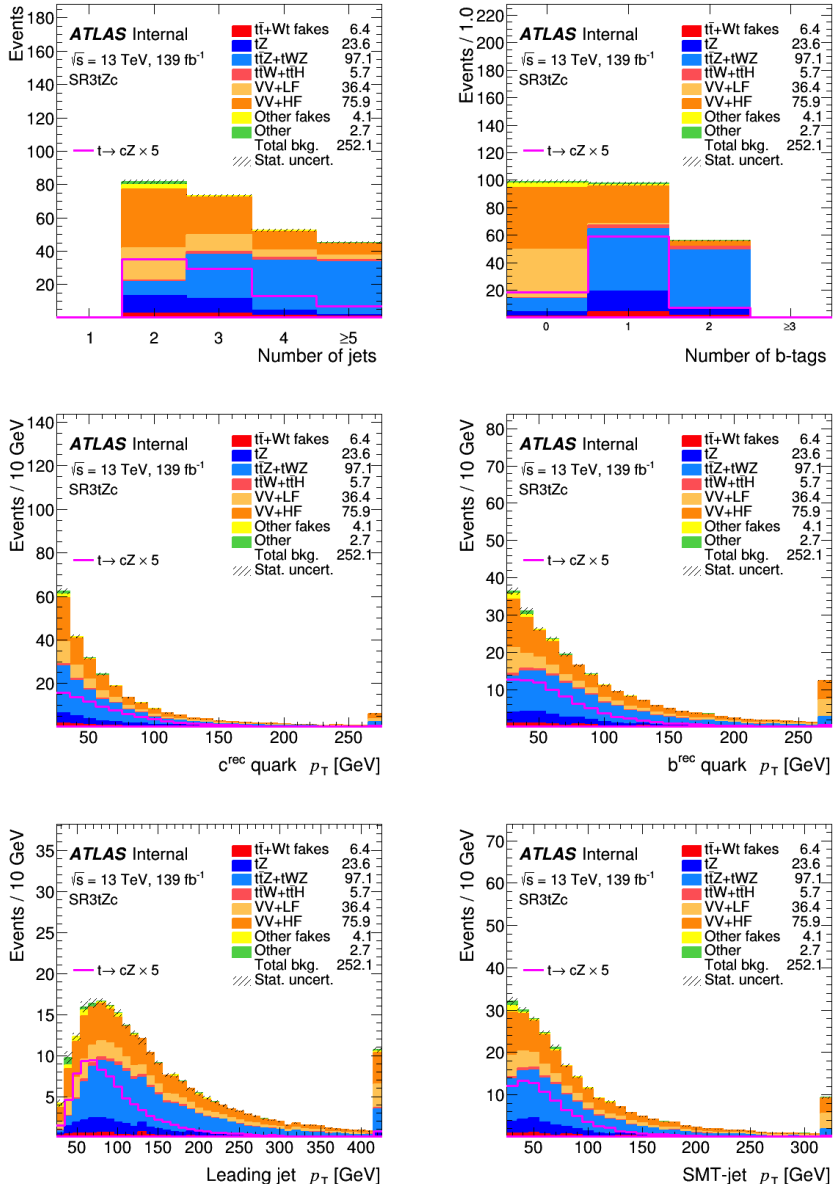


Figure 6.2 – Pre-fit distributions of kinematic variables of jets for events selected in the SR3tZc region. Number of signal events are normalised to the current observed branching ratio limits and scaled by factor 5. The uncertainty band includes only the statistical uncertainty. These distributions are blinded, following the blinding strategy.

Sample	Number of b -jets			Total yield
	=0	=1	=2	
ZZ+LF	15.40 ± 0.24	0.41 ± 0.04	0.00 ± 0.00	15.81 ± 0.25
ZZ+HF	4.64 ± 0.12	5.15 ± 0.13	0.83 ± 0.03	10.63 ± 0.18
WZ+LF	20.13 ± 0.36	0.45 ± 0.06	0.01 ± 0.01	20.59 ± 0.37
WZ+HF	40.24 ± 0.51	21.92 ± 0.38	3.10 ± 0.12	65.27 ± 0.65
VV (2l)	0.05 ± 0.08	0.09 ± 0.04	0.00 ± 0.00	0.15 ± 0.09
WtZ	1.87 ± 0.19	7.80 ± 0.40	3.59 ± 0.26	13.26 ± 0.51
t tW	0.23 ± 0.04	1.28 ± 0.10	1.04 ± 0.09	2.55 ± 0.14
t tZ (2l)	0.00 ± 0.00	0.02 ± 0.02	0.00 ± 0.00	0.02 ± 0.02
t tZ	7.69 ± 0.20	37.81 ± 0.45	38.35 ± 0.46	83.85 ± 0.67
Wt	0 ± 0.00	0.27 ± 0.19	0.00 ± 0.00	0.27 ± 0.19
tZ	8 ± 0.15	14.85 ± 0.30	5.60 ± 0.16	23.63 ± 0.37
t t	0.91 ± 0.19	3.97 ± 0.39	1.29 ± 0.22	6.17 ± 0.48
Z+jets	2.85 ± 0.80	1.07 ± 0.65	0.20 ± 0.20	4.12 ± 1.05
4 tops	0.01 ± 0.00	0.05 ± 0.01	0.15 ± 0.01	0.20 ± 0.01
3 tops	0.00 ± 0.00	0.01 ± 0.00	0.02 ± 0.00	0.03 ± 0.00
VVV	37 ± 0.02	0.11 ± 0.01	0.01 ± 0.00	0.49 ± 0.03
VH	5 ± 0.64	0.80 ± 0.57	0.00 ± 0.00	1.76 ± 0.86
t tH	0.24 ± 0.02	1.37 ± 0.04	1.51 ± 0.04	3.12 ± 0.05
t tWW	0.01 ± 0.01	0.09 ± 0.03	0.13 ± 0.03	0.23 ± 0.05
Total bkg.	98.79 ± 1.29	97.53 ± 1.25	55.82 ± 0.64	252.14 ± 1.91
FCNC t t (cZ)	3.44 ± 0.02	10.65 ± 0.04	1.40 ± 0.02	15.49 ± 0.05
FCNC (c)tZ	0.31 ± 0.02	1.34 ± 0.03	0.10 ± 0.01	1.74 ± 0.04

Table 6.2 – Event yield for each b-jet multiplicities and total event yield for the SR3tZc selection.

6.1.3 Reconstruction of the soft muon decay chain

In t \bar{t} events the soft muon can be originated from various sources. In MC simulation, truth information are used to identify the origin of the soft muon and the truth flavour of the SMT-jet that contains the soft muon. Therefore it is possible to reconstruct the chain of ancestors which in the end produces the soft muon. Four categories of events can be identified:

- muons originating from the decay chain of a b-quark produced by a $t \rightarrow Wb$ decay if the hadron and the b-quark are spatially matched within $\Delta R < 0.4$. Events with muons from $b \rightarrow \mu$, $b \rightarrow c \rightarrow \mu$ and $b \rightarrow \tau \rightarrow \mu$, are included in this category;
- muons originating from the decay chain of a c-quark produced by a $t \rightarrow cZ$ decay if the hadron and the c-quark are spatially matched within $\Delta R < 0.4$. Events with muons from $c \rightarrow \mu$ and $c \rightarrow \tau \rightarrow \mu$, are included in this category;
- muons which are either produced by light hadrons coming from a top-quark decay ($t \rightarrow Wb$ or $t \rightarrow cZ$) or muons coming from the decay in flight of light hadrons, mostly pions and kaons. These muons can be also categorised as ‘fake-SMT’;
- muons that are effectively prompt leptons from a W or Z boson decay, failing the prompt lepton selection cuts, being close to a jet and therefore entering the soft muon selection criteria, referred to as prompt $\rightarrow \mu$.

According to the categories described above, Table 6.3 shows the composition for the signal sample FCNC t t (cZ). It can be noted that soft muons come from B-hadrons ($\sim 60\%$) and

C-hadrons ($\sim 40\%$) decays. Table 6.4 and Table 6.5 show the composition for the main backgrounds, $t\bar{t}Z$ and $VV + HF$ respectively.

For $t\bar{t}Z$ the main contributions come from B-hadrons ($\sim 80\%$) as expected by the $t\bar{t}Z$ topology. For $VV + HF$ the main contributions come from C-hadrons ($\sim 60\%$), mostly $WZ + c\bar{c}$.

FCNC $t\bar{t}(cZ)$	
Total number of events = 15.49	
Chain	Fractions [%]
b $\rightarrow \mu$	15.60
b $\rightarrow c \rightarrow \mu$	10.16
b $\rightarrow \tau \rightarrow \mu$	0.80
c $\rightarrow \mu$	57.46
c $\rightarrow \tau \rightarrow \mu$	0.70
light $\rightarrow \mu$	10.80
prompt $\rightarrow \mu$	4.48

Table 6.3 – Reconstructed chain of ancestors that produces the soft muon for the signal sample FCNC $t\bar{t}(cZ)$.

$t\bar{t}Z$	
Total number of events = 83.85	
Chain	Fractions [%]
b $\rightarrow \mu$	42.24
b $\rightarrow c \rightarrow \mu$	31.82
b $\rightarrow \tau \rightarrow \mu$	3.01
c $\rightarrow \mu$	12.95
c $\rightarrow \tau \rightarrow \mu$	0.14
light $\rightarrow \mu$	7.32
prompt $\rightarrow \mu$	2.52

Table 6.4 – Reconstructed chain of ancestors that produces the soft muon for the background sample $t\bar{t}Z$.

$VV + HF$	
Total number of events = 75.90	
Chain	Fractions [%]
b $\rightarrow \mu$	6.60
b $\rightarrow c \rightarrow \mu$	9.23
b $\rightarrow \tau \rightarrow \mu$	0.80
c $\rightarrow \mu$	57.46
c $\rightarrow \tau \rightarrow \mu$	0.60
light $\rightarrow \mu$	10.83
prompt $\rightarrow \mu$	4.48

Table 6.5 – Reconstructed chain of ancestors that produces the soft muon for the background sample $VV + HF$.

6.2 Background estimation

A variety of background sources are considered. These include SM processes with similar final states as the FCNC tZc process (such as diboson or the associated production of $t\bar{t}$ with a Z boson), as well as events in which at least one of the leptons in the final state is *fake* (either a jet misidentified as a lepton or a non-prompt lepton). The estimation for the various sources of background relies on MC simulations, for both the normalisation and the shape, while for the $t\bar{t}$ fake-lepton background the shapes are taken from MC but the normalisation is extracted from data.

The $t\bar{t}Z$ enters the event selection because of the presence in the final state of a SM top quark and of a Z boson. The only difference to the signal topology, for the semi-leptonic $t\bar{t}$ decay, is the presence of additional jets in the event.

The diboson background (mainly W Z and Z Z) enters the selection because of the presence of a Z boson and of additional jets, that can come from heavy quarks. The diboson background is split into $VV + HF$ (heavy flavour) and $VV + LF$ (light flavour) based on the types of jets associated: if one of the associated jets originated from b-quark or c-quark then it is considered as $VV + HF$, otherwise it is considered as $VV + LF$. The jet type is determined using the `jet_truthtable` variable. This variable, provided by the flavour tagging group, defines a cone of $\Delta R < 0.3$ associated with each jet. If a b-hadron with ($p_T > 5$ GeV) is found within this cone the jet is identified as a *b*-jet. If no b-hadrons are found, the algorithm searches for c-hadrons, then τ leptons. If none of these identifiers are found the jet is labelled as a light jet.

6.3 Separation of signal from background events

A multivariate analysis (MVA) technique is used to separate signal from background. The Gradient Boosted Decision Trees (GBDT) method with TMVA software package is exploited in this study [144, 145]. The GBDT output score is in the range between -1 and 1. The most signal-like events have scores near 1 while the most background-like events have scores near -1. The GBDTs are trained separately in each signal regions as described below. The SR3tZc is defined targeting the FCNC tZc coupling in $t\bar{t}$ decay events using the soft muon tagging, therefore the MVA discriminant for this coupling, D_3 , is built using the GBDT trained with the FCNC tZc $t\bar{t}$ decay events against backgrounds.

6.3.1 Input variables

A set of variables as the GBDT input is used to train and test the GBDT method on the events in SR3tZc. Those variables are listed in Table 6.6, ordered by the separation value, defined by, as in [145]:

$$\langle s^2 \rangle = \frac{1}{2} \int \frac{[p_s(y) - p_b(y)]^2}{p_s(y) + p_b(y)} dy$$

where $p_s(y)$ and $p_b(y)$ are the signal and background PDFs of the classifier y . The separation is 0 (1) for identical (non-overlapping) signal and background shapes.

These sets of input variables are constructed based on separation values, correlations and impact

on the BDT performance. The details are documented in Appendix D. The distributions of input variables in the Signal Region is presented in Figure 6.3.

Variable	$\langle s^2 \rangle$	Definition
$m_{b\ell\nu}$	0.1717	SM top-quark candidate mass
$N b\text{ jets}$	0.08218	Number of b-jets tagged with DL1r
$m_{q\ell\ell}$	0.07019	FCNC top-quark candidate mass
$\frac{\mu^{softID} p_T}{SMT \text{ jet Sum} p_T \text{ Trk}}$	0.03357	Ratio between the soft muon ID pT and pT sum of tracks
$\Delta R(\ell, Z)$	0.03141	ΔR between W boson lepton and Z boson candidates
$\Delta R(t_{\text{SM}}, t_{\text{FCNC}})$	0.02508	ΔR between SM and FCNC top-quark candidates
$\Delta R(\mu^{soft}, Z)$	0.006596	ΔR between soft muon and Z boson candidates

Table 6.6 – Set of variables used in the training of the GBDT in SR3tZc to built the D_3 discriminant used in the tZc coupling search. Variables are ordered by the separation $\langle s^2 \rangle$ value.

6.3.2 GBDT training and evaluation

In order to train the GBDT algorithm and have a reliable model with a good performance, it is better to use as much statistics as possible from the available signal and background MC samples. On the other hand, to check the performance and validate the model, the trained GBDT model must be applied on the test sample (events that are not used in the training phase) that has sufficiently large statistics. Therefore, 80 % of available MC statistics is used for the training while 20 % for the testing, as described below.

All samples, including MC systematics samples and data (currently only in CRs), are divided into five approximately equal size groups using pseudo-random numbers, which ensures that the same event in nominal samples is assigned in the same group. All events in each group have assigned the same integer pseudo-random number from 1 to 5.

Five equivalent GBDT models are trained using four groups of nominal MC samples. Each training uses different combination of four groups out of five. The remaining one group is used as a test sample. Each of five GBDTs is evaluated on events with the assigned pseudo-random number that is not assigned to the training events of that GBDT.

Table 6.7 shows the values for configuration options of the BDT method. They are chosen to counteract overtraining and have an optimal performance.

Option	Value for D_3
NTrees	800
MinNodeSize	2%
BoostType	Grad
Shrinkage	0.05
UseBaggedBoost	True
BaggedSampleFraction	0.6
nCuts	200
MaxDepth	2
NegWeightTreatment	IgnoreNegWeightsInTraining

Table 6.7 – Used values for configuration options of the TMVA method Boosted Decision Trees [145].

6.3.3 GBDT performance and overtraining checks

Overtraining leads to a seeming increase in the classification performance over the objectively achievable one, if measured on the training sample, and to an effective performance decrease when measured with an independent test sample. A convenient way to detect overtraining and to measure its impact is therefore to compare the performance results between training and test samples. Figure 6.4 present the Receiver Operating Characteristic (ROC) curves for each GBDT output score in the signal region, while Figure 6.6 show the GBDT output score distributions for signal and background samples, comparing results between training and test samples. No significant overtraining is detected. The five GBDT output scores used to built discriminant variables are compared in Figure 6.7.

Input variables importance for each GBDT are presented in Table 6.8. The importance is evaluated as the total separation gain that this variable had in the decision trees (weighted by the number of events). It is normalized to all variables together, which have an importance of 1.

Variable	GBDT #1	GBDT #2	GBDT #3	GBDT #4	GBDT #5
$m_{q\ell\ell}$	0.1807	0.1758	0.1795	0.1799	0.1767
$\Delta R(\mu^{soft}, Z)$	0.1613	0.1597	0.1603	0.1555	0.1616
$\Delta R(t_{SM}, t_{FCNC})$	0.161	0.1635	0.1598	0.1634	0.1635
$m_{b\ell\nu}$	0.1536	0.1566	0.1565	0.1642	0.1478
$\Delta R(\ell, Z)$	0.1359	0.1433	0.1399	0.1378	0.1446
$\frac{\mu^{soft} ID p_T}{SMT \text{jet } Sump_T Trk}$	0.1216	0.1179	0.122	0.1203	0.1216
$N b \text{ jets}$	0.08582	0.08308	0.08205	0.07875	0.08431

Table 6.8 – Input variables importance in each GBDT used to built the D_3 discriminant.

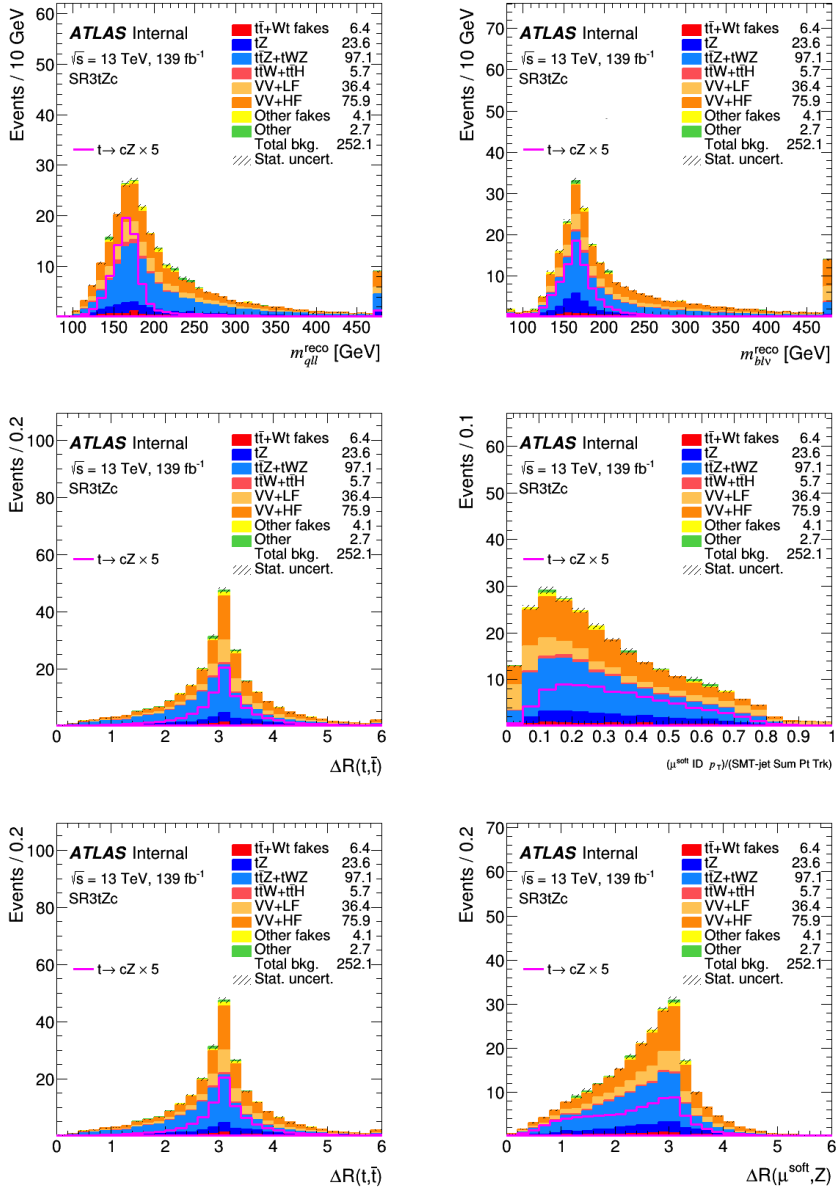


Figure 6.3 – Pre-fit distributions of the input variables used in the training of the GBDT in SR3tZc to built the D_3 discriminant. Number of signal events are normalised to the current observed branching ratio limits and scaled by factor 5. The uncertainty band includes only the statistical uncertainty. These distributions are blinded, following the blinding strategy.

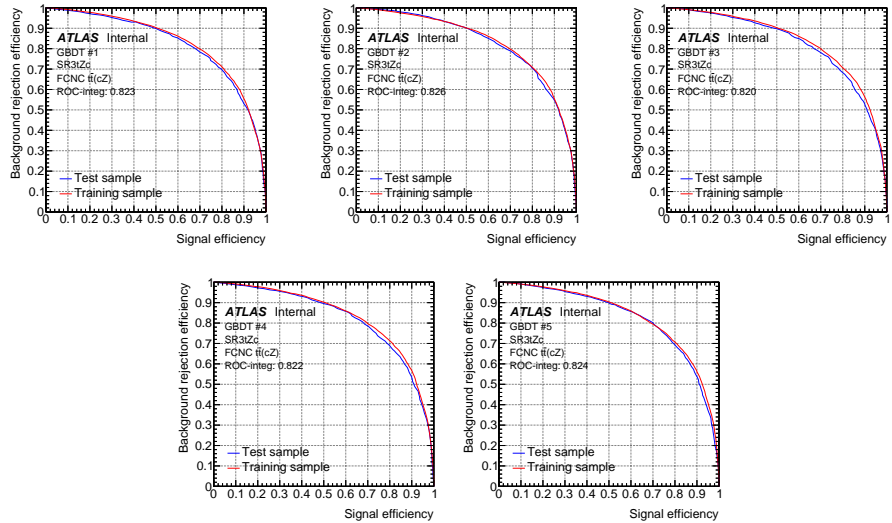


Figure 6.4 – The ROC curves for each of five GBDTs trained in SR3tZc to built the D_3 discriminant. Comparing results between training and test samples.

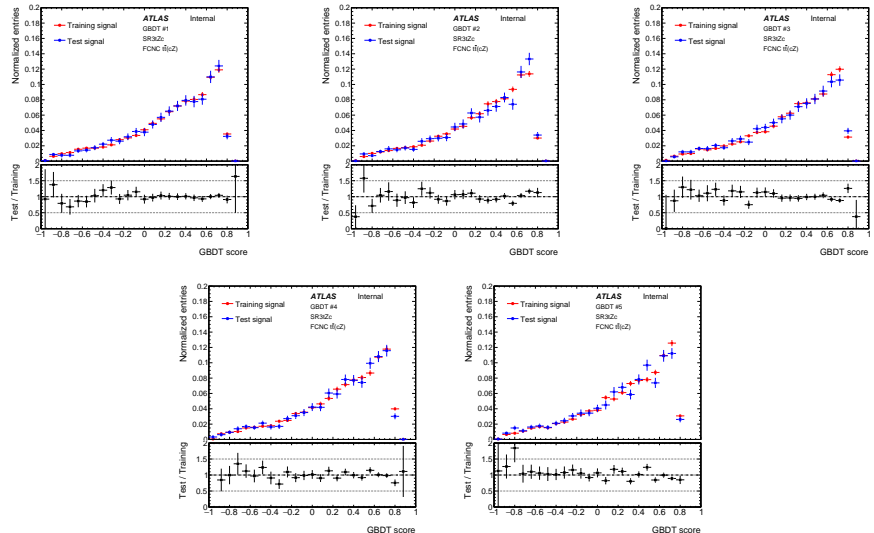


Figure 6.5 – The FCNC $t\bar{Z}c$ $t\bar{t}$ decay signal GBDT output score distribution for each of five GBDTs trained in SR3tZc to built the D_3 discriminant. Comparing results between training and test samples.

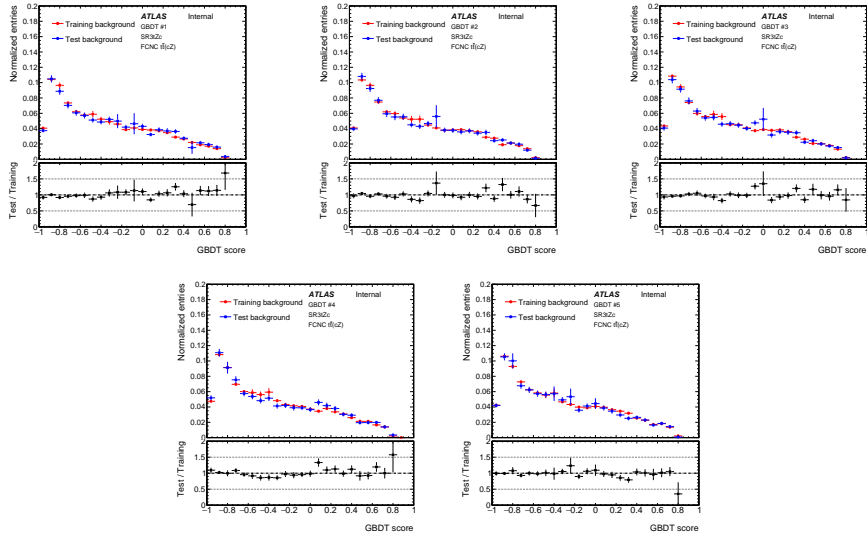


Figure 6.6 – The background GBDT output score distribution for each of five GBDTs trained in SR3tZc to built the D_3 discriminant. Comparing results between training and test samples.

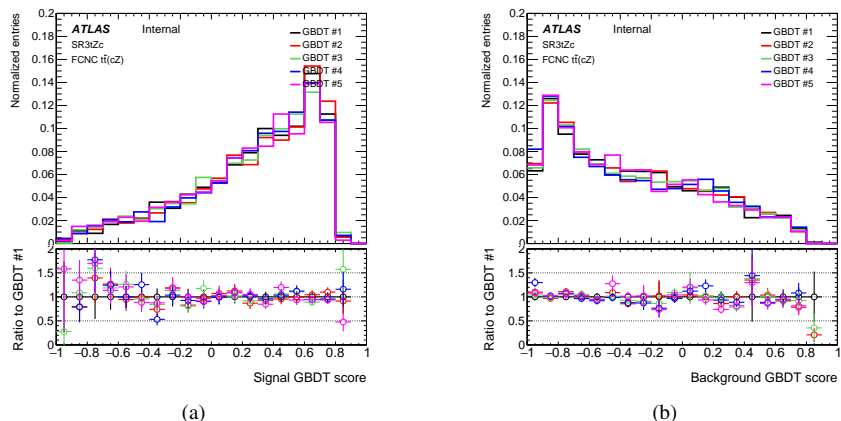


Figure 6.7 – The GBDT output score distributions for (a) signal events and (b) background events, in the test samples. Trained five GBDTs are compared in each signal region.

6.4 The alternative c-tagger DL1r_c

The alternative c-tagger DL1r_c (see Section 4.2.6.2) has been investigated for SR3tZc as an alternative to SMT, already discussed in Section 6.1.2.

The requirements in this region are the following:

- At least two jets satisfying the requirements described in Section 4.2.4.
- Exactly one b-jet satisfying the requirements in Section 4.2.6.1.
- At least one c-jets satisfying the requirements described in Section 4.2.6.2.
- No requirements on the masses of both the FCNC and the SM top-quark candidates are applied.

This selection is summarized in Table 6.9 together with the selection using SMT for comparison. Kinematic plots are presented in Section E.3.

Common selections	
Exactly 3 leptons with $ \eta < 2.5$ and $p_T(\ell_1) > 27 \text{ GeV}$, $p_T(\ell_2) > 15 \text{ GeV}$, $p_T(\ell_3) > 15 \text{ GeV}$	
≥ 1 OSSF pair, with $ m_{\ell\ell} - 91.2 \text{ GeV} < 15 \text{ GeV}$	=1 b-jet
≥ 2 jets with $ \eta < 2.5$	-
SR3tZc using SMT	SR3tZc using DL1r _c
≤ 2 b-tagged jets	≥ 1 c-tagged jet
OS(μ^{soft}, ℓ_W)	-
≥ 1 SMT jet	-
-	-

Table 6.9 – Overview of the requirements applied for selecting events in the Signal Region with DL1r_c

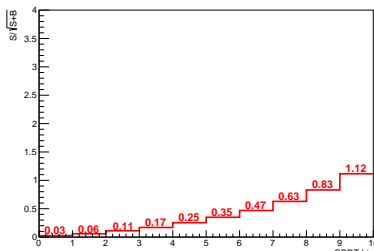
The event yield for this selection is shown in Table 6.10.

Comparing the two event yield in Table 6.2 with Table 6.10 is possible to see that using DL1r_c the number of signal events is significantly larger than using SMT since the semi-leptonic decay of heavy hadrons is limited by the branching ratio ($\simeq 20\%$). However, taking into account the SMT selection with only one b-jet, it is also possible to see that SMT has a better discrimination of backgrounds mainly due to a better light-rejection.

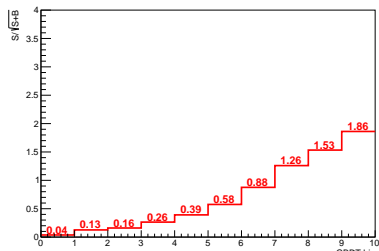
To choose the best selection, one can compare the values of $\frac{S}{\sqrt{S+B}}$ for each bin of the GBDT discriminant as can be seen in Table 6.11 for the SMT selection, in Table 6.12 for DL1r_c selection, and Figure 6.8.

For the DL1r_c selection, in the last three bins of the GBDT discriminant, there are 12.3 events of signal and 9.3 events of background which corresponds to more signal events and 10% background events of the whole SR3tZc with SMT. The GBDT output for SMT is presented in Section 6.3 while for DL1r_c it will be presented in Section 7.3.

Sample	Total yield
ZZ+LF	0.71 ± 0.07
ZZ+HF	5.31 ± 0.13
WZ+LF	2.18 ± 0.12
WZ+HF	25.02 ± 0.39
VV (2l)	0.05 ± 0.04
WtZ	12.39 ± 0.49
$t\bar{t}W$	2.04 ± 0.12
$t\bar{t}Z$ (2l)	0.02 ± 0.02
$t\bar{t}Z$	69.49 ± 0.61
Wt	0.00 ± 0.00
tZ	13.82 ± 0.28
$t\bar{t}$	3.66 ± 0.37
Z+jets	1.32 ± 0.58
4 tops	0.09 ± 0.01
3 tops	0.02 ± 0.00
VVV	0.22 ± 0.02
VH	0.00 ± 0.00
$t\bar{t}H$	2.63 ± 0.05
$t\bar{t}WW$	0.16 ± 0.04
Total bkg.	139.13 ± 1.17
FCNC $t\bar{t}(cZ)$	21.94 ± 0.39
FCNC (c)tZ	1.21 ± 0.03

Table 6.10 – Total event yield for the SR3tZc selection using the c-tagger DL1r_c .

(a) SMT selection

(b) DL1r_c selection**Figure 6.8** – Values of $\frac{S}{\sqrt{S+B}}$ for each bin of the GBDT discriminant for (a) SMT selection and (b) for DL1r_c selection.

Sample	Bin 6	Bin 7	Bin 8	Bin 9	Bin 10
Others	0.46 ± 0.42	0.91 ± 0.63	0.04 ± 0.05	0.02 ± 0.05	0.00 ± 0.05
$Z + \text{jets}$	0.18 ± 0.17	0.00 ± 0.17	0.26 ± 0.23	0.40 ± 0.28	0.21 ± 0.36
$t\bar{t} + tW$	1.07 ± 0.28	0.61 ± 0.24	0.43 ± 0.23	0.59 ± 0.22	0.16 ± 0.21
tZq	2.80 ± 0.13	2.08 ± 0.12	2.10 ± 0.11	1.48 ± 0.10	1.03 ± 0.08
$VV + \text{HF}$	6.11 ± 0.19	4.65 ± 0.20	2.85 ± 0.14	1.70 ± 0.11	0.82 ± 0.09
$VV + \text{LF}$	2.67 ± 0.13	1.56 ± 0.10	0.62 ± 0.07	0.15 ± 0.04	0.06 ± 0.01
$t\bar{t}H + t\bar{t}W$	0.55 ± 0.05	0.40 ± 0.04	0.25 ± 0.04	0.15 ± 0.03	0.06 ± 0.02
$t\bar{t}Z + tWZ$	7.83 ± 0.23	6.43 ± 0.21	4.65 ± 0.18	3.12 ± 0.15	1.62 ± 0.12
Total bkg	21.67 ± 0.63	16.65 ± 0.77	11.21 ± 0.43	7.60 ± 0.42	3.97 ± 0.45
Signal	1.69 ± 0.03	2.02 ± 0.03	2.31 ± 0.03	2.66 ± 0.03	2.93 ± 0.03
S/B	0.08	0.12	0.21	0.35	0.74
$S/\sqrt{S+B}$	0.35	0.47	0.63	0.83	1.12

Table 6.11 – Values of $\frac{S}{\sqrt{S+B}}$ for each bin of the GBDT discriminant for the SMT selection.

Sample	Bin 6	Bin 7	Bin 8	Bin 9	Bin 10
Others	0.03 ± 0.03	0.01 ± 0.03	0.02 ± 0.03	0.00 ± 0.03	0.00 ± 0.03
$Z + \text{jets}$	0.36 ± 0.29	0.06 ± 0.07	0.00 ± 0.07	0.21 ± 0.24	0.00 ± 0.07
$t\bar{t} + tW$	0.64 ± 0.15	0.17 ± 0.08	0.16 ± 0.08	0.14 ± 0.07	0.17 ± 0.09
tZq	1.80 ± 0.10	1.37 ± 0.08	0.76 ± 0.06	0.46 ± 0.04	0.27 ± 0.03
$VV + \text{HF}$	2.51 ± 0.13	1.86 ± 0.12	0.97 ± 0.07	0.53 ± 0.06	0.19 ± 0.03
$VV + \text{LF}$	0.25 ± 0.04	0.24 ± 0.05	0.08 ± 0.02	0.06 ± 0.03	0.00 ± 0.00
$t\bar{t}H + t\bar{t}W$	0.36 ± 0.04	0.37 ± 0.04	0.30 ± 0.03	0.17 ± 0.03	0.10 ± 0.02
$t\bar{t}Z + tWZ$	6.77 ± 0.22	4.53 ± 0.18	2.60 ± 0.14	1.38 ± 0.09	0.66 ± 0.07
Total bkg	12.74 ± 0.43	8.60 ± 0.26	4.88 ± 0.20	2.97 ± 0.28	1.40 ± 0.14
Signal	2.23 ± 0.12	2.98 ± 0.14	3.69 ± 0.16	4.07 ± 0.16	4.54 ± 0.17
S/B	0.17	0.35	0.76	1.37	3.24
$S/\sqrt{S+B}$	0.58	0.88	1.26	1.53	1.86

Table 6.12 – Values of $\frac{S}{\sqrt{S+B}}$ for each bin of the GBDT discriminant for the DL1r_c selection.

CHAPTER 7

FCNC tZc with charm-tagging veto

This chapter presents the Signal Regions dedicated to FCNC tZc in $t\bar{t}$ decays and single-top production using vetoes on c-tagged jets. Background sources are also described as well as the definitions of several Control Regions.

7.1 Event selections and reconstruction

The pre-selection criteria, common to all the Signal Regions used in this work were already discussed in Crefsec:selection. In this section, the topology of the final states of the signal in the signal regions are described. The SR3tZc selection using the c-tagger DL1 r_c is already presented in Section 6.4.

There are two more channels that remain to present.

The first channel is FCNC tZc in $t\bar{t}$ decays, where one of the t-quarks decays following the SM into a W boson and a b-quark (called in the following *SM top*), while the other t-quark (called in the following *FCNC top*) decays into a Z boson and a c-quark. Only the trileptonic channel is considered, i.e. when the Z boson from the FCNC top decays leptonically and the W boson from the SM top decays leptonically. Therefore the final state is characterised by the presence of three leptons, a c-jet, a b-tagged jet and missing transverse momentum from the escaping neutrino. The final state of this channel was already presented in Section 6.1 with the exception that no SMT or c-tagged jet is required.

The second channel is FCNC tZc in single-top production, where the production of a single top-quark proceeds through an FCNC interaction. The t-quark is produced in association with a Z boson. Also in this case only the trileptonic channel is considered. Therefore the final state is

characterised by the presence of three leptons, a b-tagged jet and missing transverse momentum from the escaping neutrino.

7.1.1 Top quarks reconstruction

In the events having at least two jets with one of them being b-tagged, two top quarks (FCNC and SM tops) candidates are reconstructed under the FCNC $t\bar{t}$ decay signal hypothesis. The kinematics of the top-quark candidates can be reconstructed from the corresponding decay particles using Equation (6.1) in Section 6.1.1 as well more other details about the Top quarks reconstruction. The SM top quark candidate is reconstructed under the FCNC single-top quark production hypothesis in the events having one or two jets with exactly one being *b*-tagged, which is assumed to come from the top-quark decay ($t \rightarrow bW$). The lepton not used to reconstruct the Z boson is assumed to be the one coming from W boson decay and the missing transverse momentum is assumed to be the transverse momentum of the neutrino from W boson decay, while the most probable value for the longitudinal component of the neutrino momentum is determined using the minimisation of the following expression:

$$\chi^2_{tZ} = \frac{(m_{b\ell_W\nu}^{\text{reco}} - m_{t_{\text{SM}}})^2}{\sigma_{t_{\text{SM}}}^2} + \frac{(m_{\ell_W\nu}^{\text{reco}} - m_W)^2}{\sigma_W^2}, \quad (7.1)$$

where $m_{b\ell_W\nu}^{\text{reco}}$ and $m_{\ell_W\nu}^{\text{reco}}$ are the reconstructed masses of the bW and $\ell_W\nu$ systems, respectively. In eq. (7.1), the central value for the masses and the widths of the top quark and W boson are the same as in eq. (6.1), therefore, in the events with two jets, the four-momentum of SM top-quark candidate reconstructed under the FCNC single-top quark production signal hypothesis is the same as the one reconstructed under the FCNC $t\bar{t}$ decay signal hypothesis.

The mass cuts are applied on the reconstructed top-quark candidates in the signal regions as described in the following sections.

The overview of the requirements applied for selecting events in all the signal regions is shown in Table 7.1.

7.1.2 SR1 selections

The SR1 have the following additional requirements:

- At least two jets satisfying the requirements described in Section 4.2.4.
- Exactly one b-jet satisfying the requirements described in Section 4.2.6.1.
- The mass of the FCNC top-quark candidate, m_t^{FCNC} , must be within $2\sigma^{\text{FCNC}}$ from 172.5 GeV, while no requirement on the mass of the SM top-quark candidate, m_t^{SM} , is applied.

In the SR1tZc region there is also a veto of events where there is a c-tagged jet described in Section 4.2.6.2. Kinematic plots are presented in Section E.1.

7.1.3 SR2 selections

The SR2s (both SR2tZu and SR2tZc) have the following additional requirements:

- Exactly one or two jets satisfying the requirements described in Section 4.2.4.

- Exactly one b-jet satisfying the requirements described in Section 4.2.6.1.
- The lepton not used to reconstruct the Z boson is assumed to be the one coming from the W boson. The transverse mass is calculated using the momentum of the lepton associated with the W boson, E_T^{miss} and azimuthal angle, ϕ , between them: $m_T(\ell_W, \nu) = \sqrt{2p_T^\ell E_T^{\text{miss}}(1 - \cos \Delta\phi)}$. Events are required to have $m_T(\ell_W, \nu) > 40 \text{ GeV}$.
- For events with exactly one jet, no requirement is applied on the massed of the FCNC and SM top-quark candidates. For events with exactly two jets, the mass of the FCNC top-quark candidate, m_t^{FCNC} , must be outside $2\sigma^{\text{FCNC}}$ from 172.5 GeV, while the mass of the SM top-quark candidate, m_t^{SM} , must be within $2\sigma^{\text{SM}}$ from 172.5 GeV. The requirement on m_t^{FCNC} makes this region orthogonal to SR1.

In the SR2tZc region there is also a veto of events where there is a c-tagged jet described in Section 4.2.6.2. Kinematic plots are presented in Section E.2.

Common selections			
Exactly 3 leptons with $ \eta < 2.5$ and $p_T(\ell_1) > 27 \text{ GeV}$, $p_T(\ell_2) > 15 \text{ GeV}$, $p_T(\ell_3) > 15 \text{ GeV}$ ≥ 1 OSSF pair, with $ m_{\ell\ell} - 91.2 \text{ GeV} < 15 \text{ GeV}$			
SR1tZc	SR2tZc	SR3tZc	
≥ 2 jets with $ \eta < 2.5$ $= 1$ b-jet $-$ $= 0$ c-tagged jet $ m_t^{\text{FCNC}} - 172.5 \text{ GeV} < 2\sigma^{\text{FCNC}}$ $-$	$= 1$ jet with $ \eta < 2.5$ $= 1$ b-jet $m_T(\ell_W, \nu) > 40 \text{ GeV}$ $-$ $-$ $-$	$= 2$ jets with $ \eta < 2.5$ $= 1$ b-jet $m_T(\ell_W, \nu) > 40 \text{ GeV}$ $= 0$ c-tagged jet $ m_t^{\text{FCNC}} - 172.5 \text{ GeV} > 2\sigma^{\text{FCNC}}$ $ m_t^{\text{SM}} - 172.5 \text{ GeV} < 2\sigma^{\text{SM}}$	≥ 2 jets with $ \eta < 2.5$ $= 1$ b-jet $-$ ≥ 1 c-tagged jet $-$ $-$

Table 7.1 – Overview of the requirements applied for selecting events in the signal regions.

7.1.4 Event yields in the Signal Regions

Event yields in the SRs for the tZc coupling extraction are reported in Table 7.2.

As it can be noticed, the main background sources are:

- for SR1s (both SR1tZu and SR1tZc), $t\bar{t}Z$ and $VV + HF$;
- for SR2s (both SR2tZu and SR2tZc), $VV + HF$ and Standard Model tZq;
- for SR3, $t\bar{t}Z$.

	SR1tZc	SR2tZc	SR3tZc
$t\bar{t}Z$	137.9 ± 0.9	24.11 ± 0.31	69.5 ± 0.6
tWZ	30.6 ± 0.8	9.4 ± 0.4	12.4 ± 0.5
$t\bar{t}W$	5.78 ± 0.22	3.33 ± 0.15	2.04 ± 0.12
$t\bar{t}H$	6.10 ± 0.08	0.881 ± 0.023	2.63 ± 0.05
$VV + LF$	28.2 ± 0.5	34.8 ± 1.5	2.89 ± 0.14
$VV + HF$	142.7 ± 1.0	155.9 ± 2.2	30.3 ± 0.4
tZq	46.5 ± 0.6	110.0 ± 0.7	13.82 ± 0.28
$t\bar{t}$	20.0 ± 0.9	31.5 ± 1.1	3.7 ± 0.4
tW	0.7 ± 0.4	0.8 ± 0.4	< 0.001
Z + jets	9.9 ± 1.6	11.8 ± 1.9	1.3 ± 0.6
VH	1.2 ± 1.2	3.2 ± 1.2	< 0.001
$t\bar{t}W W$	0.39 ± 0.06	0.027 ± 0.016	0.16 ± 0.04
VVV	0.704 ± 0.032	0.590 ± 0.034	0.220 ± 0.016
4 tops	0.151 ± 0.011	0.0030 ± 0.0012	0.092 ± 0.010
3 tops	0.0220 ± 0.0029	0.0011 ± 0.0010	0.0155 ± 0.0025
$t\bar{t}Z$ (2l)	0.046 ± 0.034	0.009 ± 0.029	0.02 ± 0.05
VV (2l)	0.49 ± 0.12	0.30 ± 0.11	0.05 ± 0.07
FCNC (c)tZ	3.24 ± 0.06	11.81 ± 0.10	1.205 ± 0.033
FCNC $t\bar{t}$ (cZ)	57.3 ± 0.6	17.67 ± 0.33	21.9 ± 0.4
Total background	431.4 ± 2.7	387 ± 4	139.1 ± 1.2

Table 7.2 – Event yields in the SRs for the tZc coupling extraction. The error includes only the statistical uncertainty.

7.2 Background estimation

A variety of background sources are considered and already discussed in Section 6.2. In order to study the modelling of the main background samples, Control regions (CRs) are used in the fit to extract the normalisation of some relevant background sources.

Several CRs are defined:

- $t\bar{t}$ CR is designed to control the minor $t\bar{t}$ background. As previously mentioned, this background enters the selection because of the presence of a mis-reconstructed lepton, i.e. a fake lepton. Since this background is small, the decision was taken to evaluate it using MC. Nevertheless, the normalisation is taken from data.
- $t\bar{t}Z$ CR is designed to control the $t\bar{t}Z$ background. It is constructed by requiring the presence of more jets with respect to the jet multiplicity required in the SRs.
- Side-band CRs are designed to contain a mixture of the main background sources ($t\bar{t}Z$ and diboson). They are constructed applying cuts on the top mass.

7.2.1 Control Regions definition

In the following, the event selection in the CRs is described.

Table 7.4 summarises the selection cuts in the various CRs.

$t\bar{t}$ CR selections The $t\bar{t}$ CR is defined by requiring that there is at least one pair of opposite-sign but different-flavour leptons in the event. Obviously, no cut on the invariant mass of the opposite-sign leptons is applied. Concerning the jet multiplicity, there should be at least one jet in the event, of which exactly one should be b-tagged. Kinematic plots are presented in Section F.1.

$t\bar{t}Z$ CR selections The $t\bar{t}Z$ CR is defined by requiring the presence of at least four jets and of exactly two b-tagged jets. Also the cut on the transverse mass of the W boson is softened to 30 GeV. To be orthogonal with SR3, also a veto on the presence of a c-jet is required. Kinematic plots are presented in Section F.2.

Side-band CR1 selections The mass side-band CR1 is defined by requiring the presence of at least two jets and of exactly one b-tagged jet. The mass of the FCNC top-quark candidate, m_t^{FCNC} , must be outside $2\sigma^{FCNC}$ from 172.5 GeV, the mass of the SM top-quark candidate, m_t^{SM} , must be also outside $2\sigma^{SM}$ from 172.5 GeV. In addition, a veto on the presence of a c-jet is required. Kinematic plots are presented in Section F.3.

Side-band CR2 selections The mass side-band CR2 is defined by requiring the presence of exactly one or two jets and of exactly one b-tagged jet. The transverse mass is calculated using the momentum of the lepton associated with the W boson, E_T^{miss} and azimuthal angle, ϕ , between them: $m_T(\ell_W, \nu) = \sqrt{2p_T^\ell E_T^{\text{miss}} (1 - \cos \Delta\phi)}$. Events are required to have $m_T(\ell_W, \nu) > 40$ GeV.

The mass of the SM top-quark candidate, m_t^{SM} , must be also outside $2\sigma^{SM}$ from 172.5 GeV. Kinematic plots are presented in Section F.4.

7.2.2 Event yields in the Control Regions

Event yields in the CRs are shown in Table 7.3. As it can be noticed, the signal contribution in the various CRs is small. Every Control Region is enriched of the correspondent background.

	Side-band CR1	Side-band CR2	t̄Z CR	t̄t CR
t̄Z +tWZ	88 ± 12	9.1 ± 2.1	164 ± 22	14.8 ± 1.9
t̄tW	4.3 ± 0.7	2.5 ± 0.5	2.3 ± 0.5	27 ± 4
t̄tH	2.3 ± 0.4	0.36 ± 0.07	5.4 ± 0.9	13.8 ± 2.1
VV + LF	25 ± 15	18 ± 7	0.20 ± 0.22	0.40 ± 0.21
VV + HF	130 ± 80	69 ± 28	13 ± 11	2.3 ± 1.4
tZq	20 ± 4	9.9 ± 1.7	14.6 ± 2.9	0.90 ± 0.15
t̄t +Wt	10 ± 4	9.1 ± 2.7	3.0 ± 1.2	102 ± 24
Other fakes	3 ± 5	10 ± 11	0.00 ± 0.06	0.12 ± 0.14
Other	2.2 ± 1.6	0.8 ± 2.6	1.1 ± 0.5	2.9 ± 1.5
Total background	280 ± 80	130 ± 32	203 ± 27	164 ± 25
Data	331	169	197	156
Data / Bkg.	1.18 ± 0.35	1.30 ± 0.34	0.97 ± 0.14	0.95 ± 0.16

Table 7.3 – Event yields in the CRs for the tZc coupling extraction. The error includes both statistical and systematic uncertainties.

Common selections				
Exactly 3 leptons with $ \eta < 2.5$ and $p_T(\ell_1) > 27 \text{ GeV}$, $p_T(\ell_2) > 15 \text{ GeV}$, $p_T(\ell_3) > 15 \text{ GeV}$				
t̄ CR	t̄Z CR	Side-band CR1	Side-band CR2	
≥ 1 OS pair, no OSSF	≥ 1 OSSF pair with $ m_{\ell\ell} - 91.2 \text{ GeV} < 15 \text{ GeV}$ $m_T(\ell_W, \nu) > 30 \text{ GeV}$	≥ 1 OSSF pair with $ m_{\ell\ell} - 91.2 \text{ GeV} < 15 \text{ GeV}$ $m_T(\ell_W, \nu) > 40 \text{ GeV}$	≥ 1 OSSF pair with $ m_{\ell\ell} - 91.2 \text{ GeV} < 15 \text{ GeV}$ $m_T(\ell_W, \nu) > 40 \text{ GeV}$	≥ 1 OSSF pair with $ m_{\ell\ell} - 91.2 \text{ GeV} < 15 \text{ GeV}$ $m_T(\ell_W, \nu) > 40 \text{ GeV}$
-	-	-	-	-
≥ 1 jet with $ \eta < 2.5$ = 1 b-jet	≥ 4 jet with $ \eta < 2.5$ = 2 b-jet	≥ 2 jet with $ \eta < 2.5$ = 1 b-jet = 0 c-jet	≥ 1 jet with $ \eta < 2.5$ = 1 b-jet	≥ 1 jet with $ \eta < 2.5$ = 1 b-jet
-	-	-	-	-
-	-	$ m_t^{\text{FCNC}} - 172.5 \text{ GeV} > 2\sigma^{\text{FCNC}}$ $ m_t^{\text{SM}} - 172.5 \text{ GeV} > 2\sigma^{\text{SM}}$	$ m_t^{\text{SM}} - 172.5 \text{ GeV} > 2\sigma^{\text{SM}}$	$ m_t^{\text{SM}} - 172.5 \text{ GeV} > 2\sigma^{\text{SM}}$
-	-	-	-	-

Table 7.4 – Overview of the requirements applied for selecting events in the control regions.

7.3 Separation of signal from background events

Three different GBDTs are trained separately in each signal region. In this section only the GBDT for SR3tZc will be presented because directly related to the work of this thesis.

The SR3tZc is defined targeting the FCNC tZc coupling in $t\bar{t}$ decay events using the charm tagger DL1r_c , therefore the MVA discriminant for this coupling, D_3 , is built using the GBDT trained with the FCNCtZc $t\bar{t}$ decay events against backgrounds.

The procedure is not different from that described in Section 6.3 and only the final results will be presented. The final set of variables used to train and test the GBDT method on the events in SR3tZc is in Table 7.5, ordered by the separation value.

The five GBDT output scores used to built discriminant variables are compared in Figure 7.1.

Variable	$\langle s^2 \rangle$	Definition
$m_{b\ell\nu}$	0.1329	SM top-quark candidate mass
p_T^q	0.07402	u/c-quark candidate transverse momentum
N_{jets}	0.0575	Jet multiplicity
$m_{q\ell\ell}$	0.04343	FCNC top-quark candidate mass
$\Delta R(t_{\text{SM}}, t_{\text{FCNC}})$	0.03822	ΔR between SM and FCNC top-quark candidates
$\Delta R(c, Z)$	0.0359	ΔR between c -quark and Z boson candidates
$\Delta R(\ell, Z)$	0.02417	ΔR between W boson lepton and Z boson candidates

Table 7.5 – Variables used in the training of the GBDT in SR3tZc to built the D_3 discriminant used in tZc couplings search. Variables are ordered by the separation $\langle s^2 \rangle$ value.

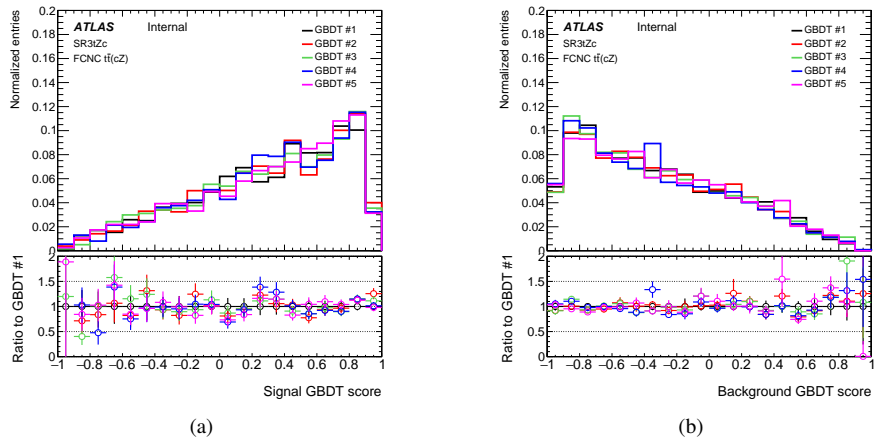


Figure 7.1 – The GBDT output score distributions for (a) signal events and (b) background events, in the test samples. Trained five GBDTs are compared in each signal region.

CHAPTER 8

Statistical analysis for tZc coupling

In this section the statistical analysis is presented. In Section 8.1 a discussion on the systematic uncertainties included in this study is reported. In Section 8.2 the fit strategy for both the tZc couplings is presented. In Section 8.3 a summary of how the fits are performed is reported. In Section 8.5 the results of the fit for the tZc coupling extraction is described.

8.1 Systematic uncertainties

Many sources of systematic uncertainties are considered in the search for FCNC tZc interaction and all of them will be reported in this section. Similarly, it will be reported also a set of systematic uncertainties that cause variations on the signal acceptance, the background rates, and the shape of the distributions that are fed to the fit. The systematic uncertainties are evaluated following the common prescriptions and the standard ATLAS procedures.

8.1.1 Sources of systematic uncertainties

Systematics uncertainties are considered for the normalisation of the individual backgrounds from various sources.

8.1.1.1 Object energy scale/resolution and efficiencies

Systematic uncertainties due to residual differences between data and Monte Carlo simulations, for jet, electron and muon reconstruction after calibration, as well as uncertainties on the calibration scale factors are propagated to the event yields and observables.

- **Lepton reconstruction**

The mis-modelling of muon (electron) trigger, reconstruction and identification efficiencies in simulation is corrected by introducing scale factors derived from measured efficiencies in data. The decays of $Z \rightarrow \mu^+ \mu^-$ ($Z \rightarrow e^+ e^-$) are used to obtain scale factors as functions of the lepton kinematics. The uncertainties are evaluated by varying the lepton and signal selections and from the uncertainties in the backgrounds evaluations.

For the SMT muons it was proved that the scale factors obtained for isolated muons are valid also for muons inside jets ??.

- **Lepton momentum scale and resolution**

The $Z \rightarrow ll$ processes are used to measure the lepton momentum scale and resolution. Calibration factors and associated uncertainties are derived to match the simulation to observed distributions in collision data. The effect of momentum scale uncertainties is evaluated by repeating the event selection after varying the lepton momentum up by 1σ and down by 1σ . For the momentum resolution uncertainties, the event selection is repeated by smearing the lepton momentum [146].

- **Jet energy scale**

The JES was derived using information from test-beam data, LHC collision data and simulation. The JES calibration consists of several steps that account for detector problems, jet reconstruction algorithms, jet fragmentation models, dense data-taking environment from high pile-up conditions and response difference between data and MC simulation. The fractional uncertainty decreases with the p_T of the reconstructed jet and is rather stable in η . The JES uncertainty has various components according to the factors it accounts for and the different steps used to compute it. The jet calibration procedure is described in Ref. [147]. The sources of the JES uncertainties with different effective number of parameters are: BJES response, detector, mixed, modelling, statistical, eta intercalibration, flavour composition, pile-up and relative non-closure.

- **Jet energy resolution**

The impact of the uncertainty on the jet energy resolution is evaluated by smearing the jet energy in the MC samples.

- **Jet vertex tagger**

The uncertainty for the JVT requirement is also applied.

- **Missing transverse momentum**

Uncertainties of the soft-track component are derived from the level of agreement between data and MC simulation of the p_T balance between the hard and soft E_T^{miss} components. Three different uncertainties are considered: an offset along the p_T (hard) axis, as well as the smearing resolution along and perpendicular to the p_T (hard) axis.

- **b -tagging efficiency**

The b -tagging efficiencies and mis-tag rate for the taggers have been measured in data using the same methods as described in [148, 149]. The number of NP used for the b -tagging data/MC scale factors is evaluated separately for b , c and light-flavour quark jets in the MC samples.

8.1.1.2 Monte Carlo modelling

Systematic effects from MC modelling are estimated by comparing different generators and varying parameters for the event generation.

- **Signal**

Scale uncertainties are included for the signal, following the latest prescriptions. In particular, the μ_r and μ_f variations are included and the envelope of the variations is added (called *Signal μ_r and μ_f*).

- $t\bar{t}$

The effect of changing the parton shower for $t\bar{t}$ events is included and the difference between PYTHIA8 and HERWIG 7 prediction is added as $t\bar{t}$ parton showering uncertainty (called *$t\bar{t}$ PS*).

Scale, radiation and tune systematics are also included, following the latest prescriptions. In particular, the μ_r and μ_f variations are included and the envelope of the variations is added (called *$t\bar{t} \mu_r$ and μ_f*). The A14 tune variations are added (called *$t\bar{t}$ A14 tune (ISR)*). Finally the FSR is varied (called *$t\bar{t}$ FSR*).

The systematic uncertainties related to the parton distribution functions are taken into account for the $t\bar{t}$ background (called *$t\bar{t}$ PDF*).

Additionally, the uncertainty associated to the h_{damp} parameter is evaluated (NP called *$t\bar{t}$ hdamp*) using the alternative sample with the h_{damp} value increased to $3.0 m_t$.

Last but not least, an uncertainty is added to take into account the differences in the photon conversion and b-hadron fractions in the signal regions with respect to the $t\bar{t}$ control region where the $t\bar{t}$ background is controlled. This uncertainty is obtained by taking the maximum difference in the fraction between the regions (13 % for b-hadron and 50 % for photon conversions) and it's applied to the relevant fraction. The two uncertainties are called *$t\bar{t}$ non-prompt lep. (photon conv.)* and *$t\bar{t}$ non-prompt lep. (b-decay)*.

- $t\bar{t}Z$

The effect of changing the MC generator for $t\bar{t}Z$ events was investigated and the difference between MADGRAPH5_aMC@NLO and SHERPA prediction is included as $t\bar{t}Z$ generator systematic uncertainty (called *$t\bar{t}Z$ Generator*).

A scale uncertainty systematic is also included, following the latest prescriptions. In particular, the μ_r and μ_f variations are included and the envelope of the variations is added (called *$t\bar{t}Z \mu_r$ and μ_f*). Additionally, the effects of QCD radiation for this sample are also taken into account through samples for different A14 tune variations (called *$t\bar{t}Z$ QCD*).

- tWZ

The effect of changing the diagram removal used for tWZ events was investigated and the difference between the two diagram removals prediction is included as tWZ generator systematic uncertainty (called *$tWZ DR$*).

- tZq

Also for SM tZq background, the differences by using different A14 tune variations are accounted and considered in the fit (called *$tZ QCD$*).

- **Diboson**

The effect of changing the MC generator for diboson events was also investigated and the difference between SHERPA and POWHEG-Box prediction is included as diboson generator uncertainty. This uncertainty is split into two components: light- and heavy-flavour (called *VV + LF Generator* and *VV + HF Generator*).

An uncertainty depending on the jet multiplicity is also included for the diboson samples with the separation by light- and heavy-flavour as well. Therefore, an uncertainty of 25 % (called *VV + LF N Jet* and similarly for *VV + HF*) is added in quadrature per jet in each jet multiplicity resulting into 5 NP ($= 1, = 2, = 3, = 4, \geq 5$ jets).

- **MC statistics**

The uncertainty due to the limited size of the MC samples is also included.

8.1.1.3 Background rate uncertainty

The uncertainties used on the background rate uncertainties are summarised in table 8.1.

- $t\bar{t}$

For the $t\bar{t}$ process, an uncertainty of 5.5 % on the normalisation is applied. Since this is one of the main backgrounds of this analysis, a normalisation factor for this background is added to the fit as a free-floating parameter.

- $t\bar{t}V$

For $t\bar{t}Z$ and $t\bar{t}W$ backgrounds, the uncertainty on the normalisation is taken from [?], where a 12 % theory uncertainty is quoted.

- tWZ

For the tWZ background, an uncertainty of 30 % is applied on the normalisation.

- tZq

For the tZq process, an uncertainty of 14 % on the normalisation is applied in agreement with the recent results from the tZq observation.

- **Diboson**

For diboson background, the normalization uncertainty is taken from ATLAS results [150]. The uncertainties applied are 20 % for the light diboson component and 30 % for the heavy diboson component. On top of that, modelling uncertainties are also used in the fit.

- $Z + \text{jets}$

Concerning the $Z + \text{jets}$ processes, an uncertainty on the normalisation is applied with a value of 100 % allowing the constraint of this value by the fit.

Process	Uncertainty
$t\bar{t}$	5.5 %
$t\bar{t}V$	12 %
tWZ	30 %
tZq	14 %
$VV + LF$	20 %
$VV + HF$	30 %
$Z + \text{jets}$	100 %

Table 8.1 – Uncertainties on the normalisation of all background processes.

8.1.1.4 Luminosity and Pile-up reweighting

The uncertainty in the combined 2015-2018 integrated luminosity is 1.7 %. It is derived, following a methodology similar to that detailed in Ref. [151], from the calibration of the luminosity scale using $x - y$ beam-separation scans.

The uncertainty of the pile-up reweighting in simulated samples is included.

8.1.2 Acceptance and shape uncertainties

The systematic uncertainties discussed above cause variations on the signal acceptance, the background rates, and the shape of the distributions that are fed to the fit. We denote the relative variation of the acceptance of process j due to a systematic source i α_{ij+} and α_{ij-} for a positive or negative variation of the systematic uncertainty.

The only systematic uncertainty that has acceptance uncertainty without a shape is luminosity. The MC statistics is related to the statistical uncertainty in each bin of the distributions that are used in the fit, so it can change the shape of the distributions. For all other systematics listed, rate and shape differences are taken into account.

8.1.2.1 Symmetrization of shape uncertainties

For the shape uncertainties included in the fit, the templates are symmetrised by taking half the difference between the up and down variation around the nominal template. For the bins where both the initial up and down variations are on the same side from the nominal, the largest variation is symmetrically assigned for the final templates.

Concerning all systematic uncertainties containing up and down systematic variations, these are symmetrised by $(\alpha_{ij-} + \alpha_{ij+})/2 = \alpha_{ij-} = \alpha_{ij+}$. For the systematic uncertainties with one sided systematics, these are symmetrised by defining $\alpha_{ij-} = \alpha_{ij+}$.

8.1.2.2 Smoothing and Pruning

Some fluctuations in individual bins can be caused by the low statistics shape systematic uncertainties. A smoothing of systematic shape uncertainties is performed using the default smoothing algorithm available through the `TRExFitter` package to average adjacent bins to remove statistical fluctuations.

Different levels of pruning are applied for shape and normalisation. A value of 1% and 0.5% were used for normalisation and shape, respectively.

8.2 Strategy

In order to extract the tZc couplings, a binned maximum likelihood fit is performed using the MC templates for both signal and background predictions.

The software framework used for performing the fit is `TRExFitter` [152]. This combines the functionalities of `RooFit` [153] and `RooStats` [154] and is designed to build probability density functions that are automatically fit to data and interpreted with statistical tests.

The likelihood function comprises histogram bins from both SRs and CRs.

Regions The regions included in the fit, as well as the distributions that are fitted together, are summarised in Table 8.2. The definitions of the various regions are shown in Table 7.1 for the SRs and in Table 7.4 for the CRs. Some regions are used to control the overall normalisation of various backgrounds.

tZc coupling extraction		
Region	Distribution	Additional info
SR1 tZc	D_1	
SR2 tZc	D_2^c	
SR3 tZc	D_3	
Side-band CR1 tZc	D_1	
Side-band CR2	D_2^c	
tZ CR	Leading lepton p_T	
t̄ CR	Leading lepton p_T	

Table 8.2 – Overview of the regions included in the fits.

Inputs The inputs to the fit consist of binned distributions, including the signal and all background channels. Additionally, for each MC sample, separate templates that take into account the systematic variations discussed in Section 8.1 are created and included in the fit.

POI The global likelihood function describing the agreement between data and prediction as a function of the parameter of interest (POI) and the set of nuisance parameters describing the effect of the corresponding systematic uncertainty sources is constructed and fitted. The POI is the signal strength parameter, μ , a multiplicative factor for the number of signal events normalised to a reference branching ratio $BR_{\text{ref}}(t \rightarrow cZ) = 0.024\%$. The relationship between μ and the corresponding $BR(t \rightarrow cZ)$ is

$$\mu = \frac{BR(t \rightarrow cZ)(1 - BR(t \rightarrow cZ))}{BR_{\text{ref}}(t \rightarrow cZ)(1 - BR_{\text{ref}}(t \rightarrow cZ))} \quad (8.1)$$

Systematic uncertainty NPs The impact of the systematic uncertainties on the extracted μ is estimated as follows.

A nuisance parameter (NP) is associated to each systematic uncertainty. These NPs have a central value and an associated uncertainty pre-fit. The fit is able to change the central value of the NPs (called *pull*) and the uncertainty on the NP can change (this is called *constraint* if the uncertainty becomes smaller), to better describe the data. To understand the impact of the NPs on the extracted μ , the following procedure is used: several fits are performed, each fit separately for each NP, changing the central value of each NP up and down by the pre-fit (post-fit) $\pm 1\sigma$ uncertainties, fixing it to that value and performing the fit to μ . The difference between this μ and the one extracted from the standard fit, $\Delta\mu$, is the pre-fit (post-fit) impact on μ . The values of $\Delta\mu$ are shown in the so called ranking plot that helps to understand the size of the effect that the uncertainty has on the signal strength.

To prevent statistical fluctuations increasing the systematic uncertainties and wasted computation time on fitting insignificant NPs, systematic uncertainties are pruned from the fit. A value of 1 % and 0.5 % are used for normalisation and shape, respectively.

Statistical uncertainty NPs The same procedure is applied to the so called γ parameters, which represent the background statistical uncertainty in each bin of the input distributions. There is therefore one gamma parameter per bin of each input distribution.

Background treatment in the fit The $t\bar{t}Z$ and tWZ backgrounds are merged in one template as well as $t\bar{t}$ and tW . Two templates are included in the fit for diboson process that correspond to the heavy and light components ($VV + HF$ and $VV + LF$). Separate templates are used for the remaining background sources. The normalisation of $t\bar{t} + tW$ background is free floating in the fit meaning that an unconstrained NP is associated to the corresponding template, namely $\mu_{t\bar{t}+tW}$. All other backgrounds have pre-fit normalizations with uncertainties (see Section 8.1.1).

8.3 Summary of fits

For the extraction of the tZc coupling, the following fits are presented:

B-only fit in CRs in this fit only CRs are used. Real data are used. The signal templates are not included in the fit.

S+B fit in SR+CRs with realistic Asimov in this fit both SRs and CRs are used. Real data is used in the CRs. In the SRs an Asimov dataset is constructed using post-fit background normalisations from the B-only fit in CRs.

These are summarised in the following table:

Setup	Fit	SRs	CRs	Template	Reference
1	B-only in CRs	–	real data	B	Appendix G
2	S+B in SRs+CRs with realistic Asimov	realistic Asimov from Setup 1	real data	S+B	Section 8.4

8.4 Signal + Background fit in SRs+CRs with realistic Asimov

To extract the expected sensitivity, an SRs+CRs S+B fit is performed. Real data is used in CRs while in SRs an Asimov dataset is used, constructed using the background normalisations found in Appendix G.

A summary of plots and tables shown in this section are the following:

- The value of the post-fit normalisation parameters of the free floating background is shown in Figure 8.1.
- The pull distributions of the all nuisance parameters can be seen in Figures 8.2 and 8.3 and Figure 8.4.
- The correlation matrix of the nuisance parameters is shown in Figure 8.5.
- The list of the systematic shapes that are dropped from the fit for each sample and for each region is shown in fig. 8.6.
- The ranking of the nuisance parameters is shown in Figure 8.7.
- Event yields pre- and post-fit are shown in Tables 8.3 and 8.4.
- Pre-fit and post-fit distributions of the fitted distributions in the various regions are shown in Figures 8.8 to 8.11.

As expected, the behaviour of the fit with the realistic Asimov dataset is almost identical to the results of the B-only fit in the CRs (Chapter G). Normalisation factors (fig. 8.1) and NP pulls and constraints (Figures 8.2 and 8.3) are very similar.

None of the systematic uncertainties has a post-fit impact on the signal strength parameter greater than 3%. Concerning the correlations between NPs (Figure 8.5), some strong correlations between diboson related NPs are present, as expected. This is also true for the $t\bar{t}$ normalisation and some $t\bar{t}$ modeling NPs.

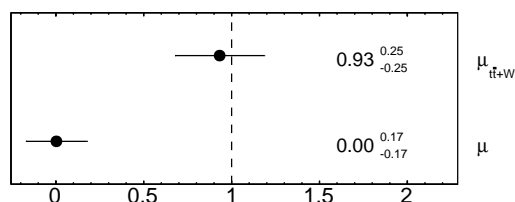


Figure 8.1 – Normalisation factors for the S+B tZc fit in SRs+CRs with realistic Asimov.

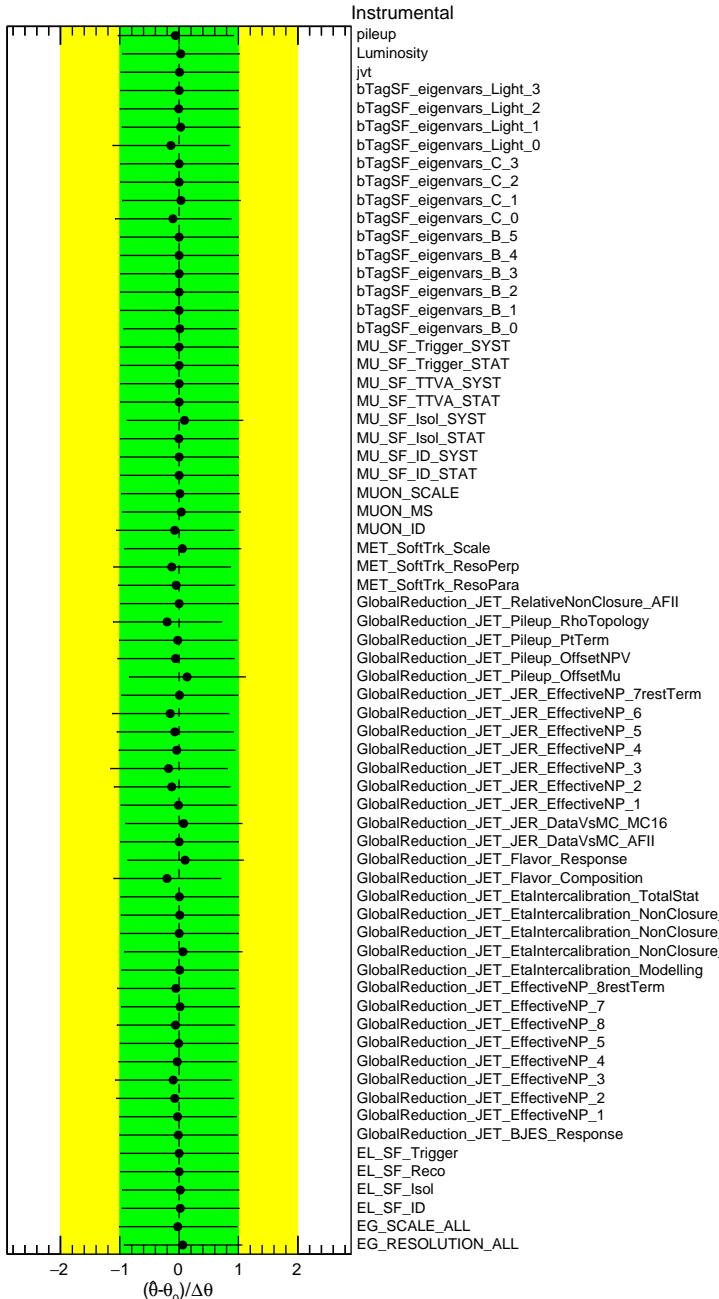


Figure 8.2 – Pulls and constraints of the instrumental nuisance parameters for the S+B tZc fit in SRs+CRs with realistic Asimov.

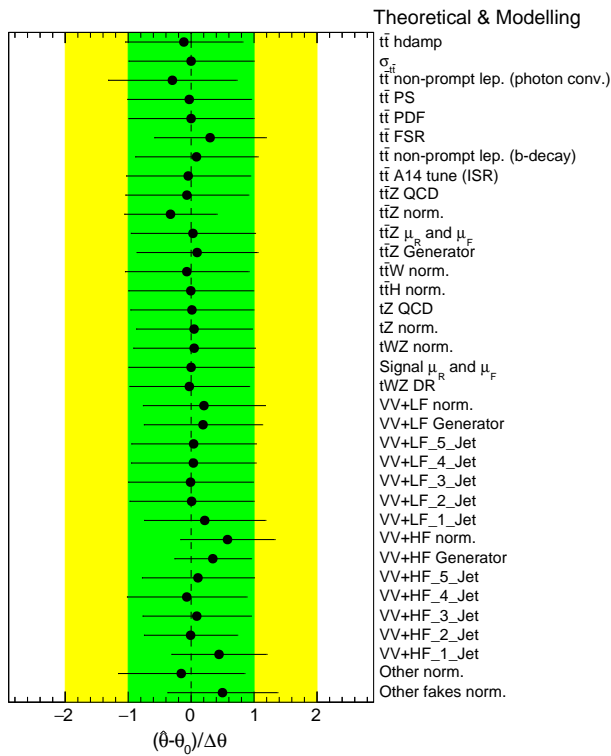


Figure 8.3 – Pulls and constraints of the theoretical and modeling nuisance parameters for the S+B tZc fit in SRs+CRs with realistic Asimov.

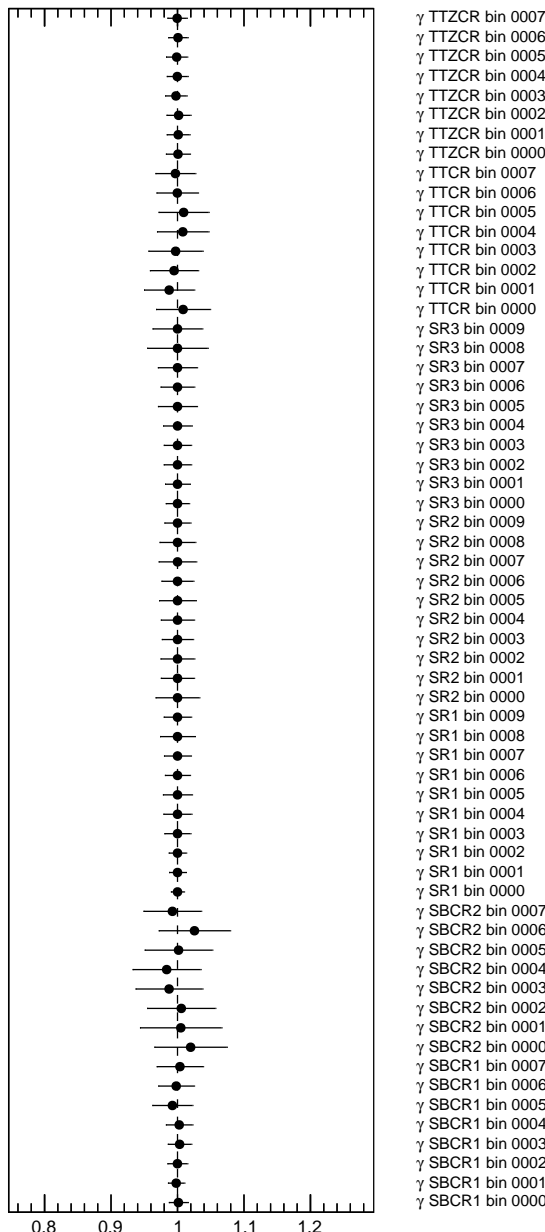


Figure 8.4 – Gamma parameters for the S+B tZc fit in SRs+CRs with realistic Asimov.

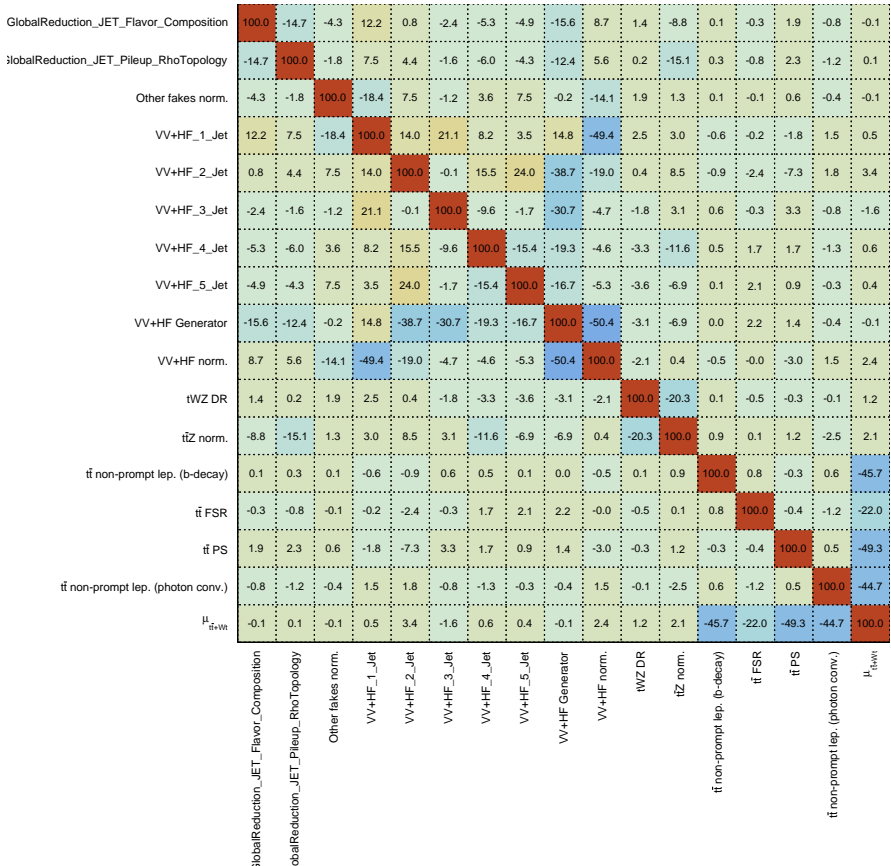


Figure 8.5 – Correlation matrix of the nuisance parameters for the $S+B$ $t\bar{Z}c$ fit in SRs+CRs with realistic Asimov.

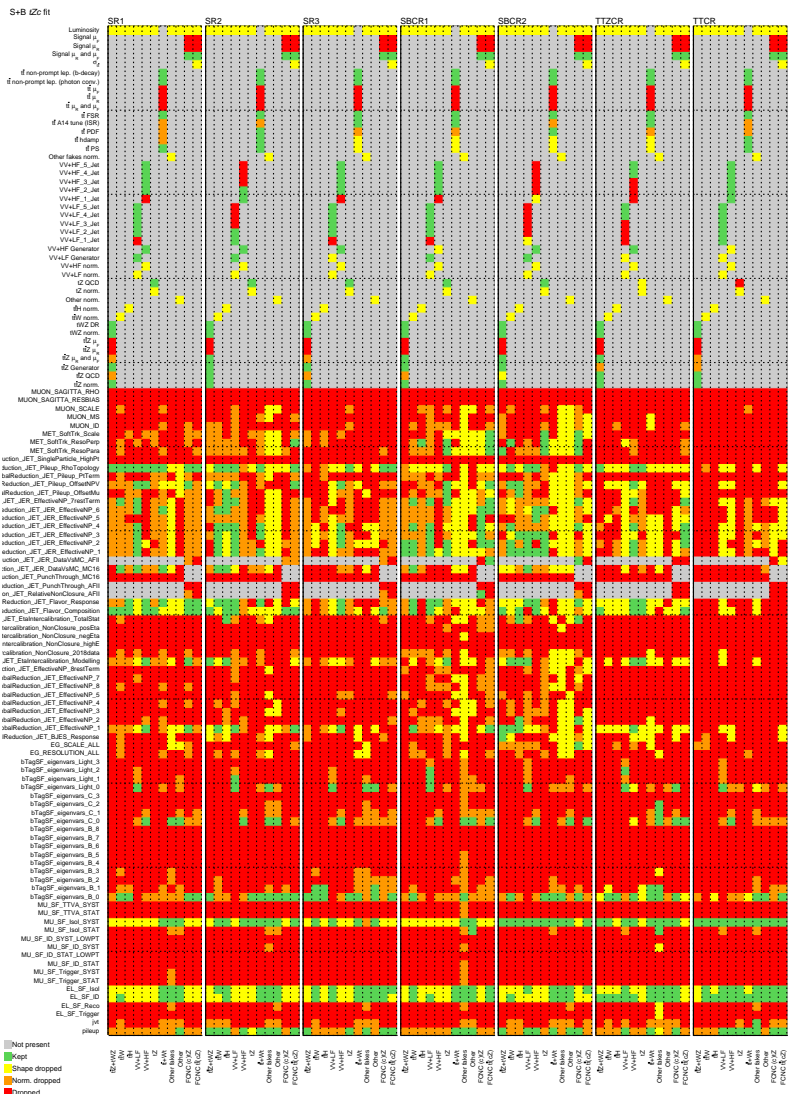


Figure 8.6 – Pruning of the nuisance parameters for the S+B tZc fit in SRs+CRs with realistic Asimov.

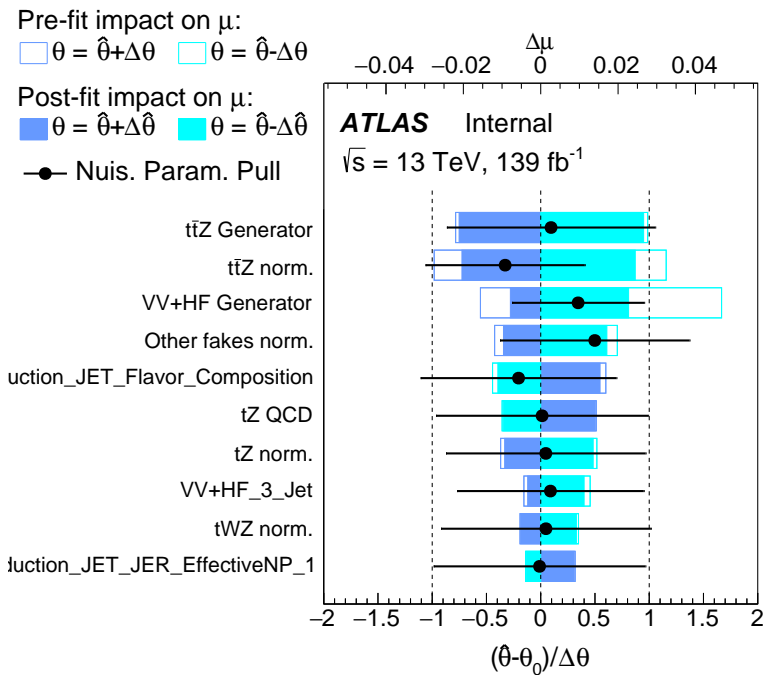


Figure 8.7 – Ranking of the nuisance parameters for the S+B tZc fit in SRs+CRs with realistic Asimov.

	SR1	SR2	SR3	Side-band CR1	Side-band CR2	t̄Z CR	t̄t CR
t̄Z +tWZ	168 ± 22	33 ± 7	82 ± 11	88 ± 12	9.1 ± 2.1	164 ± 22	14.8 ± 1.9
t̄W	5.8 ± 1.0	3.3 ± 0.6	2.04 ± 0.35	4.3 ± 0.7	2.5 ± 0.5	2.3 ± 0.5	27 ± 4
t̄H	6.1 ± 1.0	0.88 ± 0.18	2.6 ± 0.4	2.3 ± 0.4	0.36 ± 0.07	5.4 ± 0.9	13.8 ± 2.1
V V + LF	28 ± 17	35 ± 13	2.9 ± 2.0	25 ± 15	18 ± 7	0.20 ± 0.22	0.40 ± 0.21
V V + HF	140 ± 100	160 ± 70	30 ± 22	130 ± 80	69 ± 28	13 ± 11	2.3 ± 1.4
tZq	47 ± 7	110 ± 18	13.8 ± 2.3	20 ± 4	9.9 ± 1.7	14.6 ± 2.9	0.90 ± 0.15
t̄t +Wt	21 ± 4	32 ± 11	3.7 ± 1.0	10 ± 4	9.1 ± 2.7	3.0 ± 1.2	102 ± 24
Other fakes	10 ± 11	12 ± 12	1.4 ± 1.6	3 ± 5	10 ± 11	0.00 ± 0.06	0.12 ± 0.14
Other	2.5 ± 1.5	3.8 ± 2.8	0.48 ± 0.25	2.2 ± 1.6	0.8 ± 2.6	1.1 ± 0.5	2.9 ± 1.5
FCNC (c)t̄Z	3.24 ± 0.26	11.8 ± 0.6	1.21 ± 0.09	1.06 ± 0.12	0.83 ± 0.09	0.24 ± 0.04	0.083 ± 0.012
FCNC t̄t (cZ)	57 ± 5	17.7 ± 1.9	21.9 ± 1.6	4.2 ± 0.6	1.9 ± 0.4	3.7 ± 0.5	0.37 ± 0.07
Total background	430 ± 110	390 ± 80	139 ± 25	280 ± 80	130 ± 32	203 ± 27	164 ± 25
Data	488	452	150	331	169	197	156
Data / Bkg.	1.13 ± 0.28	1.17 ± 0.24	1.08 ± 0.21	1.18 ± 0.35	1.30 ± 0.34	0.97 ± 0.14	0.95 ± 0.16

Table 8.3 – Pre-fit event yields in the S+B tZc fit in SRs+CRs with realistic Asimov. The error includes both statistical and systematic uncertainties.

	SR1tZc	SR2tZc	SR3tZc	Side-band CR1tZc	Side-band CR2	t̄Z CR	t̄t CR
t̄Z +tWZ	163 ± 14	34 ± 6	79 ± 7	85 ± 9	9.3 ± 1.9	157 ± 13	14.4 ± 1.3
t̄W	5.7 ± 0.9	3.4 ± 0.6	2.01 ± 0.32	4.2 ± 0.7	2.5 ± 0.5	2.2 ± 0.4	26 ± 4
t̄H	6.1 ± 0.9	0.90 ± 0.17	2.6 ± 0.4	2.3 ± 0.4	0.37 ± 0.07	5.3 ± 0.8	13.8 ± 2.1
V V + LF	32 ± 18	39 ± 14	3.3 ± 2.1	29 ± 16	21 ± 8	0.24 ± 0.23	0.40 ± 0.18
V V + HF	198 ± 32	212 ± 29	43 ± 7	172 ± 25	94 ± 16	18 ± 6	3.3 ± 0.5
tZq	46 ± 7	112 ± 16	13.9 ± 2.1	19.6 ± 3.3	10.1 ± 1.6	14.4 ± 2.5	0.91 ± 0.12
t̄t +Wt	18 ± 4	30 ± 7	3.2 ± 0.7	9.5 ± 2.8	8.6 ± 1.7	2.5 ± 0.8	95 ± 13
Other fakes	15 ± 11	17 ± 13	2.1 ± 1.7	5 ± 5	18 ± 15	0.005 ± 0.009	0.18 ± 0.13
Other	2.2 ± 1.2	3.7 ± 2.5	0.44 ± 0.23	1.8 ± 1.2	0.2 ± 0.8	1.0 ± 0.5	2.7 ± 1.4
FCNC (c)t̄Z	0.0 ± 0.6	0.0 ± 2.1	0.00 ± 0.21	0.00 ± 0.18	0.00 ± 0.15	0.00 ± 0.04	0.000 ± 0.014
FCNC t̄t (cZ)	0 ± 10	0.1 ± 3.1	0 ± 4	0.0 ± 0.7	0.01 ± 0.33	0.0 ± 0.6	0.00 ± 0.06
Total background	487 ± 21	452 ± 20	150 ± 7	328 ± 17	165 ± 13	201 ± 12	157 ± 12
Data	488	452	150	331	169	197	156
Data / Bkg.	1.00 ± 0.04	1.00 ± 0.04	1.00 ± 0.05	1.01 ± 0.05	1.02 ± 0.08	0.98 ± 0.06	0.99 ± 0.08

Table 8.4 – Post-fit event yields in the S+B tZc fit in SRs+CRs with realistic Asimov. The error includes both statistical and systematic uncertainties.

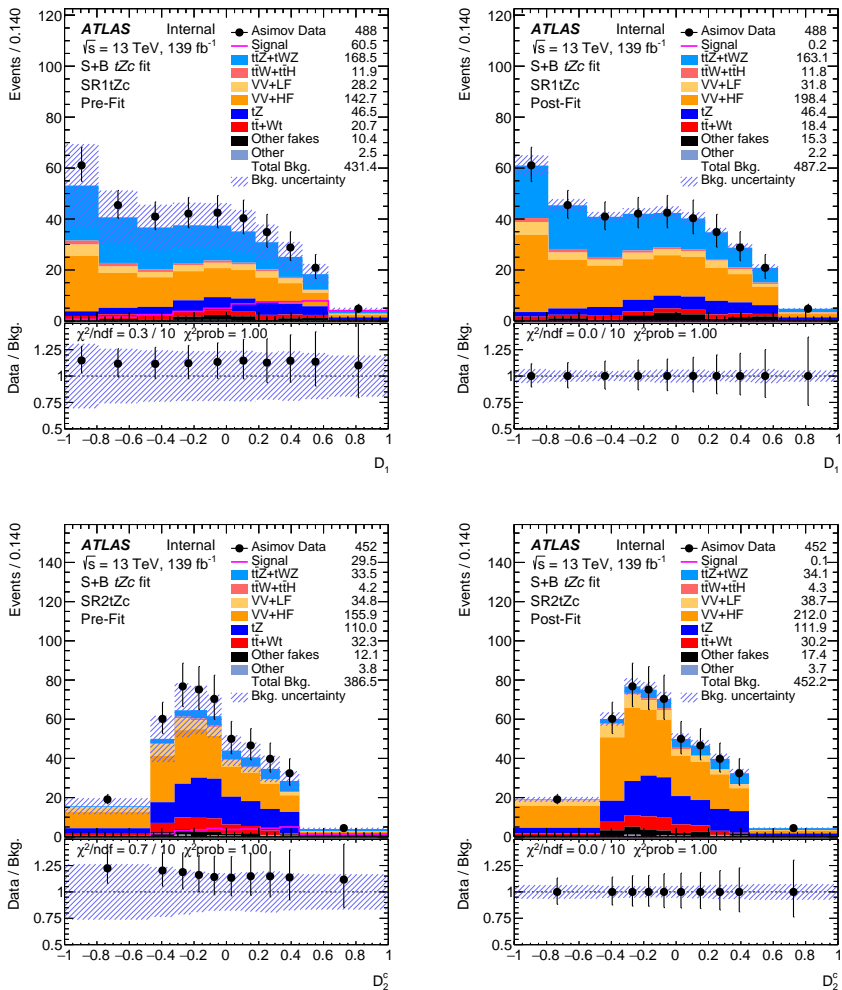


Figure 8.8 – Pre-fit (left) and post-fit (right) BDTG output distributions in SR1 and SR2 for the S+B tZc fit in SRs+CRs with realistic Asimov. The uncertainty band includes both statistical and systematic uncertainties.

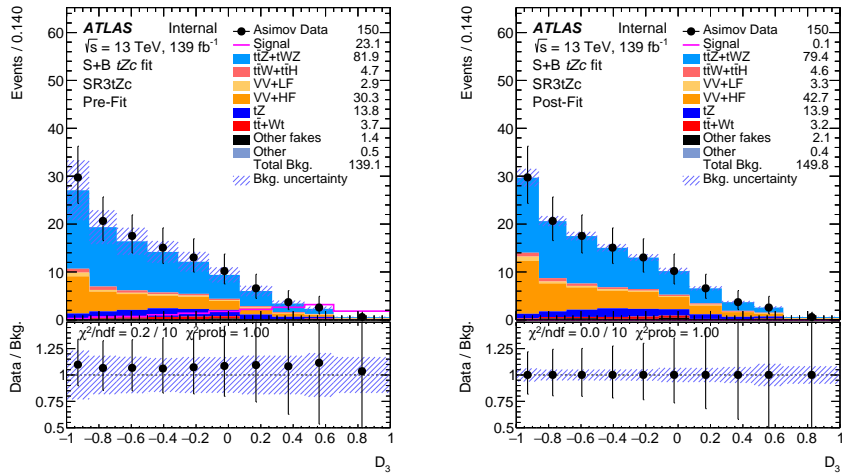


Figure 8.9 – Pre-fit (left) and post-fit (right) leading lepton p_T distributions in SR3 for the S+B $t\bar{Z}c$ fit in SRs+CRs with realistic Asimov. The uncertainty band includes both statistical and systematic uncertainties.

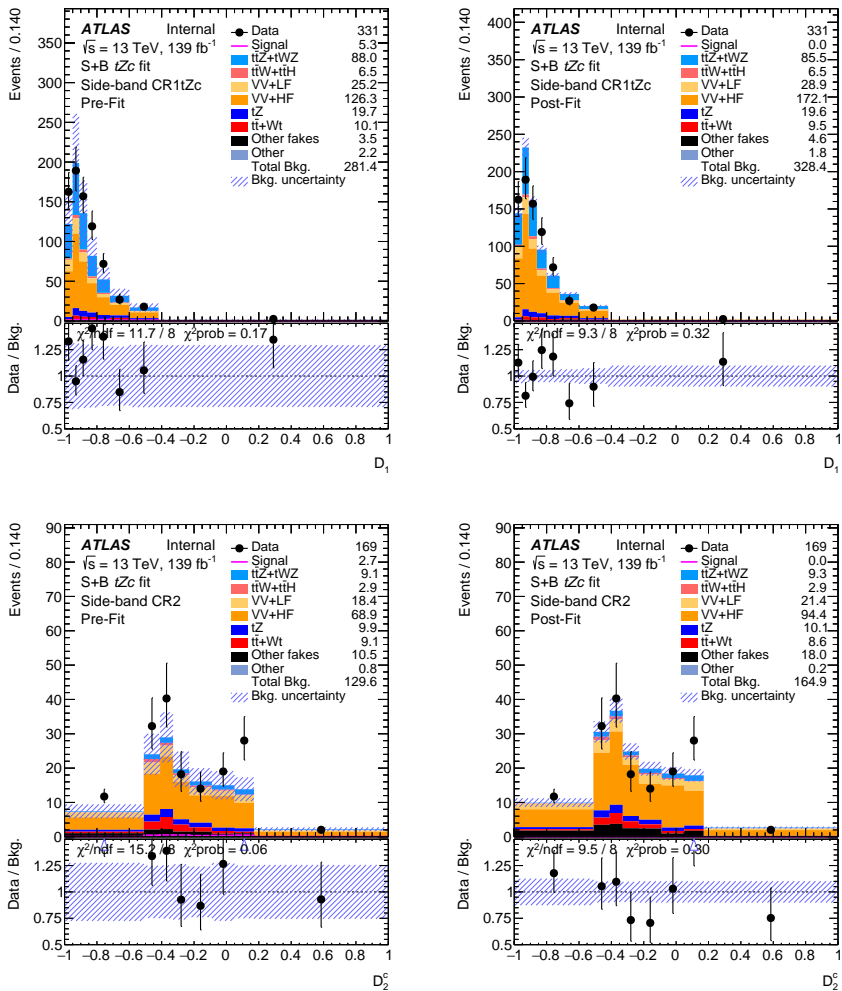


Figure 8.10 – Pre-fit (left) and post-fit (right) BDTG output distributions in the side-band CRs for the S+B tZc fit in SRs+CRs with realistic Asimov. The uncertainty band includes both statistical and systematic uncertainties.

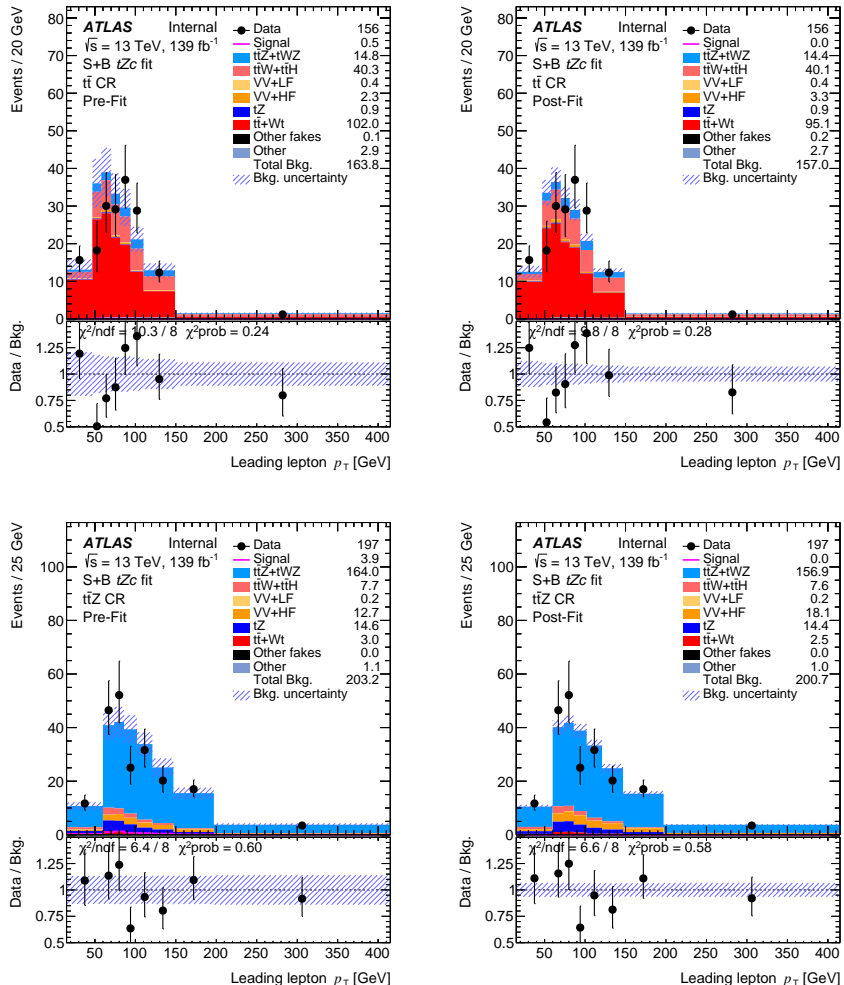


Figure 8.11 – Pre-fit (left) and post-fit (right) leading lepton p_T distributions in the $t\bar{t}$ and $t\bar{t}Z$ CRs for the S+B $t\bar{t}Z$ fit in SRs+CRs with realistic Asimov. The uncertainty band includes both statistical and systematic uncertainties.

8.5 Results

From the fits described in this chapter, in particular the signal+background fits in SRs+CRs with the realistic Asimov datasets in Section 8.4, expected limits on the branching ratios of $t \rightarrow Zc$ are extracted.

In Table 8.5 is also possible to estimate the impact of the c-tagging using $DL1r_c$ or SMT (presented in Chapter 6) on the analysis comparing the results without using none of these techniques (called 'Baseline').

The improvement obtained using SMT is around 2%, while using $DL1r_c$ is around 10%.

Expected limits on BR $t \rightarrow Zc$		
Baseline $[\times 10^{-5}]$	Using SMT $[\times 10^{-5}]$	Using $DL1r_c$
10.67	10.43	9.55

Table 8.5 – Expected limits on the branching ratios of $t \rightarrow Zc$. Results using $DL1r_c$, SMT and none of them are reported to estimate the impact of these techniques on the analysis.

The expected limits, together with statistical only limits and the expected limits from the previous ATLAS analysis [83], are reported in table 8.6.

The overall impact of systematics on the expected limit is 22%.

The limit from the previous analysis is improved by a factor of 2.3 for the tZc coupling.

Limits	-1σ	Expected	$+1\sigma$
BR $t \rightarrow Zc$ [83]	2.2×10^{-4}	3.2×10^{-4}	4.6×10^{-4}
BR $t \rightarrow Zc$ (stat. only)	5.3×10^{-5}	7.4×10^{-5}	10.5×10^{-5}
BR $t \rightarrow Zc$	6.9×10^{-5}	9.6×10^{-5}	13.8×10^{-5}

Table 8.6 – Expected limits on the branching ratios of $t \rightarrow Zc$. Expected limit from [83] is also included for reference.

CHAPTER 9

Conclusions

APPENDIX A

Monte Carlo samples

This appendix summarises the MC datasets used in this analysis.

Table A.1 shows the nominal signal samples produced in fast simulation, for mc16a, mc16d and mc16e.

Table A.2 shows the nominal background samples produced in full simulation, for mc16a, mc16d and mc16e.

Table A.3 shows the samples used for systematic uncertainty evaluation, which are produced in fast simulation, for mc16a, mc16d and mc16e.

MC samples are normalised using the cross-sections and k-factors from the XSection-MC16-13TeV.data¹ file taken from the TopDataPreparation² on 22.06.2020.

In this file, the tZq SM cross-section is increased by 15% according to the theoretical calculations update [155].

Signal samples

mc16_13TeV.412143.aMcAtNloPythia8EvtGen_TopFCNC_ctZLH_tt_3l.deriv.DAOD_TOPQ1.e7718_a875_r9364/r10201/r10724_p3956
mc16_13TeV.412141.aMcAtNloPythia8EvtGen_TopFCNC_ctZLH_tZ_3l.deriv.DAOD_TOPQ1.e7718_a875_r9364/r10201/r10724_p3956
mc16_13TeV.412146.aMcAtNloPythia8EvtGen_TopFCNC_ctZLH_tt_3l_SMTFilter.deriv.DAOD_TOPQ1.e7718_a875_r9364/r10201/r10724_p3956

Table A.1 – Overview of the signal simulated samples (Fast Simulation).

¹<https://gitlab.cern.ch/adurglis/tqZAnalysis/-/blob/master/share/XSection-MC16-13TeV.data>

²[/cvmfs/atlas.cern.ch/repo/sw/database/GroupData/dev/AnalysisTop/TopDataPreparation/](https://cvmfs.atlas.cern.ch/repo/sw/database/GroupData/dev/AnalysisTop/TopDataPreparation/)

t̄tV

```
mc16_13TeV.410155.aMcAtNloPythia8EvtGen_MEN30NNLO_A14N23LO_ttW.deriv.DAOD_TOPQ1.e5070_s3126_r9364/r10201/r10724_p4166
mc16_13TeV.410218.aMcAtNloPythia8EvtGen_MEN30NNLO_A14N23LO_ttee.deriv.DAOD_TOPQ1.e5070_s3126_r9364/r10201/r10724_p4166
mc16_13TeV.410219.aMcAtNloPythia8EvtGen_MEN30NNLO_A14N23LO_ttumu.muriv.DAOD_TOPQ1.e5070_s3126_r9364/r10201/r10724_p4166
mc16_13TeV.410220.aMcAtNloPythia8EvtGen_MEN30NNLO_A14N23LO_tttautau.deriv.DAOD_TOPQ1.e5070_s3126_r9364/r10201/r10724_p4166
mc16_13TeV.410156.aMcAtNloPythia8EvtGen_MEN30NNLO_A14N23LO_ttZnumu.deriv.DAOD_TOPQ1.e5070_s3126_r9364/r10201/r10724_p4166
mc16_13TeV.410157.aMcAtNloPythia8EvtGen_MEN30NNLO_A14N23LO_ttZqq.deriv.DAOD_TOPQ1.e5070_s3126_r9364/r10201/r10724_p4166
```

Diboson

```
mc16_13TeV.345705.Sherpa_222_NNPDF30NNLO_gglIII_0M4I130.deriv.DAOD_TOPQ1.e6213_s3126_r9364/r10201/r10724_p4164
mc16_13TeV.345706.Sherpa_222_NNPDF30NNLO_gglIII_130M41.deriv.DAOD_TOPQ1.e6213_s3126_r9364/r10201/r10724_p4164
mc16_13TeV.364283.Sherpa_222_NNPDF30NNLO_IIIijj_EW6.deriv.DAOD_TOPQ1.e6055_s3126_r9364/r10201/r10724_p4029
mc16_13TeV.364284.Sherpa_222_NNPDF30NNLO_IIIvjj_EW6.deriv.DAOD_TOPQ1.e6055_s3126_r9364/r10201/r10724_p4164
mc16_13TeV.364250.Sherpa_222_NNPDF30NNLO_III.deriv.DAOD_TOPQ1.e5894_s3126_r9364/r10201/r10724_p4164
mc16_13TeV.364253.Sherpa_222_NNPDF30NNLO_IIIv.deriv.DAOD_TOPQ1.e5916_s3126_r9364/r10201/r10724_p4164
mc16_13TeV.364254.Sherpa_222_NNPDF30NNLO_IIvv.deriv.DAOD_TOPQ1.e5916_s3126_r9364/r10201/r10724_p4029
mc16_13TeV.345723.Sherpa_222_NNPDF30NNLO_gglvZZ.deriv.DAOD_TOPQ1.e6213_s3126_r9364/r10201/r10724_p4029
mc16_13TeV.363356.Sherpa_221_NNPDF30NNLO_ZqqZll.deriv.DAOD_TOPQ1.e5525_s3126_r9364/r10201/r10724_p4029
mc16_13TeV.363358.Sherpa_221_NNPDF30NNLO_WqqZll.deriv.DAOD_TOPQ1.e5525_s3126_r9364/r10201/r10724_p4164
```

tqZ SM

```
mc16_13TeV.412063.aMcAtNloPythia8EvtGen_tlq_NNPDF30_nf4_A14.deriv.DAOD_TOPQ1.e7054_s3126_r9364/r10201/r10724_p4062
```

tWZ

```
mc16_13TeV.410408.aMcAtNloPythia8EvtGen_tWZ_Ztoll_minDR1.deriv.DAOD_TOPQ1.e6423_s3126_r9364/r10201/r10724_p4174
```

tH

```
mc16_13TeV.346345.PhPy8EG_A14NNPDF23_NNPDF30ME_ttH125_dilep.deriv.DAOD_TOPQ1.e7148_s3126_r9364/r10201/r10724_p4031
mc16_13TeV.346344.PhPy8EG_A14NNPDF23_NNPDF30ME_ttH125_semilep.deriv.DAOD_TOPQ1.e7148_s3126_r9364/r10201/r10724_p4031
mc16_13TeV.346343.PhPy8EG_A14NNPDF23_NNPDF30ME_ttH125_allhad.deriv.DAOD_TOPQ1.e7148_s3126_r9364/r10201/r10724_p4031
```

tt

```
mc16_13TeV.410472.PhPy8EG_A14_ttbar_hdamp258p75_dil.deriv.DAOD_TOPQ1.e6348_s3126_r9364/r10201/r10724_p4166
```

tW

```
mc16_13TeV.410648.PowhegPythia8EvtGen_A14_Wt_DR_dilepton_top.deriv.DAOD_TOPQ1.e6615_s3126_r9364/r10201/r10724_p4031
mc16_13TeV.410649.PowhegPythia8EvtGen_A14_Wt_DR_dilepton_antitop.deriv.DAOD_TOPQ1.e6615_s3126_r9364/r10201/r10724_p4031
```

Z+jets

```
mc16_13TeV.361106.PowhegPythia8EvtGen_AZNLOCTEQ6L1_Zee.deriv.DAOD_TOPQ1.e3601_s3126_r9364/r10201/r10724_p4029
mc16_13TeV.361107.PowhegPythia8EvtGen_AZNLOCTEQ6L1_Zmmumu.deriv.DAOD_TOPQ1.e3601_s3126_r9364/r10201/r10724_p4029
mc16_13TeV.361108.PowhegPythia8EvtGen_AZNLOCTEQ6L1_Ztautau.deriv.DAOD_TOPQ1.e3601_s3126_r9364/r10201/r10724_p4029
```

Four tops

```
mc16_13TeV.412043.aMcAtNloPythia8EvtGen_A14NNPDF31_SM4topsNLO.deriv.DAOD_TOPQ1.e7101_a875_r9364/r10201/r10724_p4031
```

Three tops

```
mc16_13TeV.304014.MadGraphPythia8EvtGen_A14NNPDF23_3top_SM.deriv.DAOD_TOPQ1.e4324_s3126_r9364/r10201/r10724_p4166
```

V H

```
mc16_13TeV.342284.Pythia8EvtGen_A14NNPDF23LO_WH125_inc.deriv.DAOD_TOPQ1.e4246_s3126_r9364/r10201/r10724_p4164
```

```
mc16_13TeV.342285.Pythia8EvtGen_A14NNPDF23LO_ZH125_inc.deriv.DAOD_TOPQ1.e4246_s3126_r9364/r10201/r10724_p4172
```

ttWW

```
mc16_13TeV.410081.MadGraphPythia8EvtGen_A14NNPDF23_ttbarWW.deriv.DAOD_TOPQ1.e4111_s3126_r9364/r10201/r10724_p4166
```

Triboson

```
mc16_13TeV.364242.Sherpa_222_NNPDF30NNLO_WWW_3l3v_EW6.deriv.DAOD_TOPQ1.e5887_s3126_r9364/r10201/r10724_p4164
mc16_13TeV.364243.Sherpa_222_NNPDF30NNLO_WWZ_4l2v_EW6.deriv.DAOD_TOPQ1.e5887_s3126_r9364/r10201/r10724_p4164
mc16_13TeV.364245.Sherpa_222_NNPDF30NNLO_WZZ_5l1v_EW6.deriv.DAOD_TOPQ1.e5887_s3126_r9364/r10201/r10724_p4164
mc16_13TeV.364246.Sherpa_222_NNPDF30NNLO_WZZ_3l3v_EW6.deriv.DAOD_TOPQ1.e5887_s3126_r9364/r10201/r10724_p4164
mc16_13TeV.364247.Sherpa_222_NNPDF30NNLO_WZZ_6l0v_EW6.deriv.DAOD_TOPQ1.e5887_s3126_r9364/r10201/r10724_p4164
mc16_13TeV.364248.Sherpa_222_NNPDF30NNLO_WZZ_4l2v_EW6.deriv.DAOD_TOPQ1.e5887_s3126_r9364/r10201/r10724_p4164
```

Table A.2 – Overview of the background simulated samples.

t̄tZ Generator systematics

mc16_13TeV.410142.Sherpa_NNPDF30NNLO_ttll_mll5.deriv.DAOD_TOPQ1.e4686_s3126_r9364/r10201/r10724_p4031

t̄tZ A14 variation

mc16_13TeV.410370.aMcAtNloPythia8EvtGen_MEN30NLO_A14Var3UpN23LO_ttee.deriv.DAOD_TOPQ1.e6113_s3126_r9364/r10201/r10724_p4062
 mc16_13TeV.410371.aMcAtNloPythia8EvtGen_MEN30NLO_A14Var3DownN23LO_ttee.deriv.DAOD_TOPQ1.e6113_s3126_r9364/r10201/r10724_p4062
 mc16_13TeV.410372.aMcAtNloPythia8EvtGen_MEN30NLO_A14Var3UpN23LO_ttmumu.deriv.DAOD_TOPQ1.e6125_s3126_r9364/r10201/r10724_p4062
 mc16_13TeV.410373.aMcAtNloPythia8EvtGen_MEN30NLO_A14Var3DownN23LO_ttmumu.deriv.DAOD_TOPQ1.e6113_s3126_r9364/r10201/r10724_p4062
 mc16_13TeV.410374.aMcAtNloPythia8EvtGen_MEN30NLO_A14Var3UpN23LO_tttautau.deriv.DAOD_TOPQ1.e6113_s3126_r9364/r10201/r10724_p4062
 mc16_13TeV.410375.aMcAtNloPythia8EvtGen_MEN30NLO_A14Var3DownN23LO_tttautau.deriv.DAOD_TOPQ1.e6113_s3126_r9364/r10201/r10724_p4062

Diboson Generator systematics

mc16_13TeV.361601.PowhegPy8EG_CT10nloME_AZNLOCTEQ6L1_WZl1ll_mll4.deriv.DAOD_TOPQ1.e4475_s3126_r9364/r10201/r10724_p4060
 mc16_13TeV.361603.PowhegPy8EG_CT10nloME_AZNLOCTEQ6L1_ZZl1ll_mll4.deriv.DAOD_TOPQ1.e4475_s3126_r9364/r10201/r10724_p4060

t̄Z SM A14 variation

mc16_13TeV.412064.aMcAtNloPythia8EvtGen_llq_NNPDF30_nf4_A14.deriv.DAOD_TOPQ1.e7054_a875_r9364/r10201/r10724_p4062
 mc16_13TeV.412065.aMcAtNloPythia8EvtGen_llq_NNPDF30_nf4_A14.deriv.DAOD_TOPQ1.e7054_a875_r9364/r10201/r10724_p4062

tWZ Diagram Removal systematics

mc16_13TeV.412119.aMcAtNloPythia8EvtGen_tWZ_Ztoll_DR2.deriv.DAOD_TOPQ1.e7518_s3126_r9364/r10201/r10724_p4166

t̄t Parton Shower systematics

mc16_13TeV.411234.PowhegHerwig7EvtGen_tt_hdamp258p75_713_dil.deriv.DAOD_TOPQ1.e7580_a875_r9364/r10201/r10724_p4031

t̄t hdamp variation

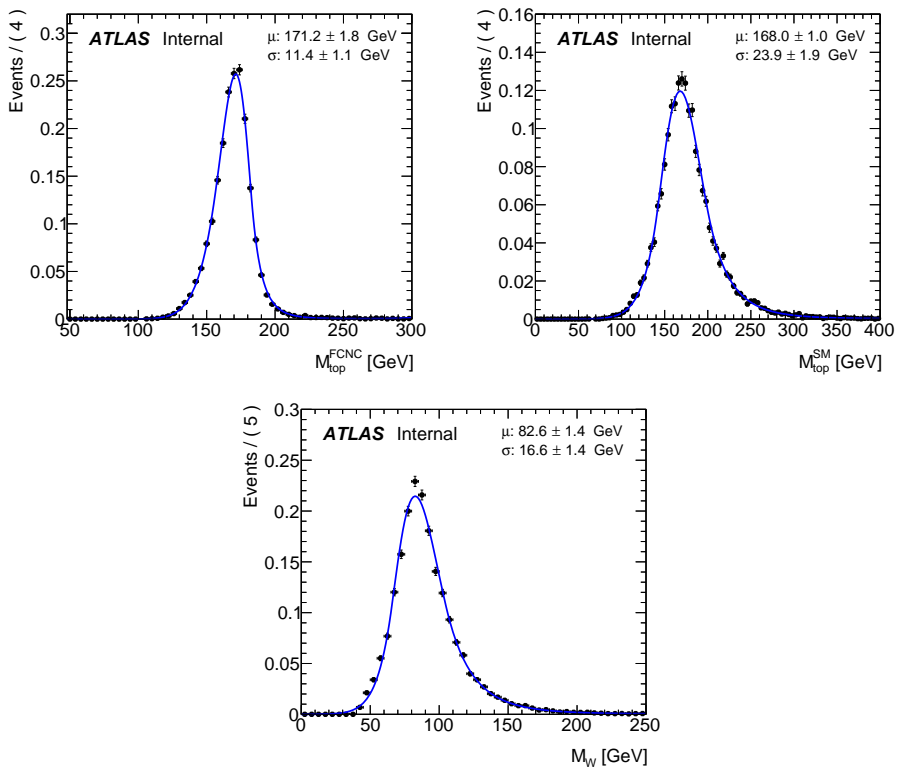
mc16_13TeV.410482.PhPy8EG_A14_ttbar_hdamp517p5_dil.deriv.DAOD_TOPQ1.e6454_a875_r9364/r10201/r10724_p4031

Table A.3 – List of systematics MC samples.

APPENDIX B

Mass Resolution

The signal events are reconstructed using a χ^2 minimisation as it is described in Section 6.1. The central value for the masses and the widths in eq. (6.1) are taken from the simulated FCNC $t\bar{t}$ decay signal samples. The values are extracted from the Bukin fits [143] to the masses of the top quarks and W boson reconstructed by matching the true generated q - and b -quarks to the reconstructed jets within the $\Delta R < 0.4$, assuming the missing transverse momentum to be the neutrino transverse momentum, and setting the longitudinal momentum of the neutrino to the p_z of the true generated particle. These represent the optimal resolution of the reconstructed t-quarks and W boson masses in the FCNC $t\bar{t}$ decay signal events. These fits are shown in fig. B.1 along with the mean values and standard deviations.

**Figure B.1**

APPENDIX C

Charm tagging using DL1r

The DL1r tagger gives the probability a jet is a b -jet, p_b , c -jet, p_c , or light jet, p_{light} . Using these probabilities the discriminant variable can be constructed to discriminate a jet of type i from jets of types j and k :

$$\text{DL1r}_i = \ln \frac{p_i}{f_j \cdot p_j + (1 - f_j) \cdot p_k}, \quad (\text{C.1})$$

where the f_j parameter controls whether jets of type i are to be primarily discriminated from jets of type j or type k . In the specific case of c -tagging the discriminant becomes:

$$\text{DL1r}_c = \ln \frac{p_c}{f_b \cdot p_b + (1 - f_b) \cdot p_{light}}. \quad (\text{C.2})$$

A value of DL1r_c must be chosen to cut on to decide whether a jet is a tagged as a c -jet or not. Therefore, there are two parameters which must be chosen, the value of f_b and the cut value, to have an optimal performance.

In order to determine the best values for f_b and DL1r_c cut, events are selected using the SR1 selection described in Section 7.1, excluding the FCNC top mass requirement. So, the selection is: 3 leptons, Z boson mass window, at least 2 jets with exactly one being b -tagged. Then, several values for f_b and DL1r_c cut were considered and for each of them events are split into two categories, c -tagged events ($=1$ c -tag) and c -tag veto events. The c -tagging is applied on jets that fail the b -tagging requirement. For each combination of f_b and DL1r_c cut values, the S/\sqrt{B} values were calculated in both c -tagged and c -tag veto events. The optimal values for f_b and DL1r_c cut would be the ones that give highest value of S/\sqrt{B} combined in quadrature from c -tagged and c -tag veto events. Figure C.1 presents the S/\sqrt{B} values for different f_b and DL1r_c cut values in c -tagged and c -tag veto events, while combined S/\sqrt{B} values are presented in fig. C.2. As the fig. C.2 suggests, the optimal c -tagging working point (WP) would be at 0.6 for f_b and 1.84 for DL1r_c cut, which gives highest value of 3.42 for combined S/\sqrt{B} . However, the optimal c -tagging working point must be calibrated, which is not trivial. Alternatively, the c -tagging working point ($f_b = 0.28$, DL1r_c cut= 1.32) being calibrated in the $t\bar{c}$ +MET SUSY analysis [68]

is used in this analysis.

Chapter C summarises the performance of the considered c -tagging working points.

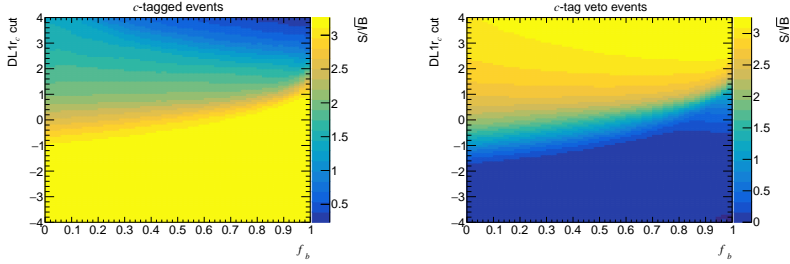


Figure C.1 – The S/\sqrt{B} values for different f_b and DL1r_c cut values in c -tagged (left) and c -tag veto (right) events.

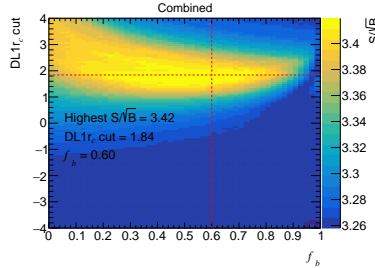


Figure C.2 – The S/\sqrt{B} values combined in quadrature from c -tagged and c -tag veto events for different f_b and DL1r_c cut values. The vertical and horizontal dashed lines indicate the f_b and DL1r_c cut values which give highest S/\sqrt{B} value.

	$f_b = 0.28$	DL1r_c cut	S/\sqrt{B}	$\text{BR}(t \rightarrow Zc)$ limit
Optimal WP	0.6	1.84	3.42	9.5×10^{-5}
$tc+\text{MET SUSY WP}$	0.28	1.32	3.39	9.7×10^{-5}

Table C.1 – Combined S/\sqrt{B} values from c -tagged and c -tag veto events, with optimal c -tagging working point and with the one used in $tc+\text{MET}$ analysis [68]. Extracted expected $\text{BR}(t \rightarrow Zc)$ limits are also shown.

APPENDIX D

BDT optimization

This section describes the study of input variables and hyper-parameters optimisation for the BDT discriminants presented in Section 6.3.

The k -fold cross-validation method with $k = 5$ is used to define the final set of input variables and determine the optimal values for BDT hyper-parameters. The total set of MC events is split into 5 folds with approximately equal sizes, using the pseudo-random numbers. Four of folds are used as a training set, and the remaining one as a validation set. Separate BDT is trained and evaluated for each fold considered as the validation fold. The performance across the validation folds is averaged to estimate the expected performance of the BDT with the considered input variables and hyper-parameters.

Many input variables are considered to train the BDT, then the ones that do not have significant impact on the BDT performance are removed since they could introduce instability in the BDT output when considering systematic uncertainties. The strategy is to remove variables that have relatively low values of separation and strong correlations with other variables, without significant loss of the BDT performance. Table D.1 shows the values for configuration options of the BDT method used for this study. They are chosen to counteract overtraining.

Option	Value for D_3
NTrees	800
MinNodeSize	2%
BoostType	Grad
Shrinkage	0.05
UseBaggedBoost	True
BaggedSampleFraction	0.6
nCuts	200
MaxDepth	2
NegWeightTreatment	IgnoreNegWeightsInTraining

Table D.1 – Used values for configuration options of the TMVA method Boosted Decision Trees [145].

D.1 Input variables

The initial (full) set of input variables considered for the D_3 discriminant in SR3 are presented in Table D.2. It includes invariant mass of the reconstructed objects as well as transverse momentum, pseudorapidity, ΔR between them in (η, ϕ) plane and other variables related to soft muons. Separation values are presented in the same table. Input variables that have separation value below 0.02 are removed and correlations among the remaining variables can be seen in Figure D.1. The $\chi^2_{t\bar{t}}$ and $m_{\ell\nu}$ variables have high correlation with $m_{q\ell\ell}$ and $m_{b\ell\nu}$, respectively, and lower separation value, so that they are removed as well as $\frac{\mu^{soft} topoetcone40}{\mu^{soft} ID p_T}$ which is highly correlated

with $\frac{\mu^{soft} ID p_T}{SMT jet Sum p_T Trk}$ and having lower separation value. Also $\Delta R(q, Z)$ and p_T^b are removed since it is highly correlated with $m_{q\ell\ell}$ and lower separation value.

The final set of input variables are presented in Table D.3.

With the full set of input variables, the BDT output score distributions in each fold for the signal and background samples are presented in Figure D.2 and Figure D.3, respectively, while for the final (reduced) set of input variables – in Figure D.4 and Figure D.5.

The ROC integral, averaged over the validation folds, for the BDT trained with the full set of input variables is 0.8595 with RMS of 0.0030, while for the BDT with final set of input variables: 0.8207 with RMS of 0.0037. Figure D.6 shows the $S_{\text{eff}}/\sqrt{B_{\text{eff}}}$ value averaged over the validation folds as a function of the cut on the BDT output score, with full set and final set of input variables. The maximum value of $S_{\text{eff}}/\sqrt{B_{\text{eff}}}$ is 2.263 with RMS of 3.881 for the full set of input variables, while 1.539 with RMS of 0.037 for the final set of input variables.

Results show that after the selection of some variables, the BDT performance is more stable, at the price of loosing $\sim 5\%$ of separation power as can be seen comparing the ROC integrals.

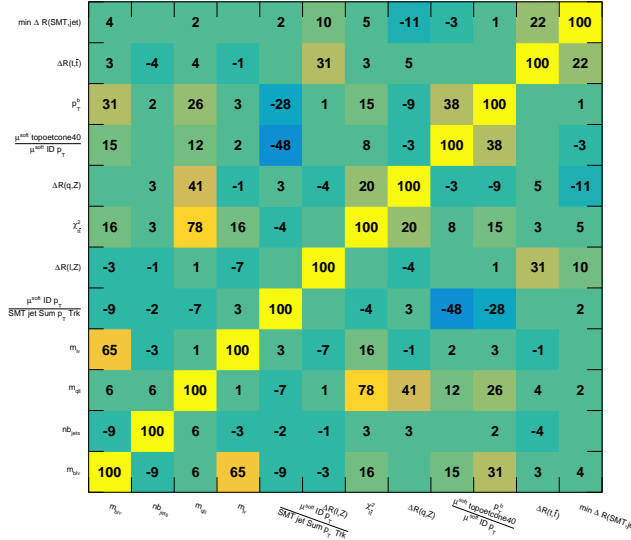
Table D.2 – Initial (full) set of input variables considered in the training of the GBDT in SR3 to built the D_3 discriminant for tZc couplings search. Variables are ordered by the separation $\langle s^2 \rangle$ value.

Variable	$\langle s^2 \rangle$	Definition
$m_{b\ell\nu}$	0.1717	SM top-quark candidate mass
$N b\text{ jets}$	0.08218	Number of b-jets tagged with DL1r
$m_{q\ell\ell}$	0.07019	FCNC top-quark candidate mass
$m_{\ell\nu}$	0.05106	W boson candidate mass
$\frac{\mu^{\text{soft}} ID p_T}{SMT \text{ jet Sum} p_T \text{ Trk}}$	0.03357	Ratio between the soft muon ID pT and pT sum of tracks
$\Delta R(\ell, Z)$	0.03141	ΔR between W boson lepton and Z boson candidates
χ^2	0.02737	χ^2 from the kinematic fit under the $t\bar{t}$ decay signal hypothesis
$\Delta R(q, Z)$	0.0262	ΔR between c -quark and Z boson candidates
$\frac{\mu^{\text{soft topocone40}}}{\mu^{\text{soft}} ID p_T}$	0.02614	Ratio between the soft muon topocone40 and soft muon pT
p_T^b	0.02566	b -quark candidate transverse momentum
$\Delta R(t_{SM}, t_{FCNC})$	0.02508	ΔR between SM and FCNC top-quark candidates
$\Delta R(SMT, \text{nearestJet})$	0.02286	ΔR between SMT-jet and its nearest jet
$N \text{ jets}$	0.01499	Number of jets
$SMT \text{ jet Num Trk}$	0.01495	SMT-jet Number of tracks
$p_T^{\ell 1}$	0.01319	Leading lepton p_T
$\frac{\mu^{\text{soft EnergyLoss}}}{\mu^{\text{soft}} p_T}$	0.01308	Ratio between the soft muon energy loss and soft muon pT
p_T^q	0.01258	c -quark candidate transverse momentum
$SMT \text{ jet Trk Width}$	0.01165	SMT-jet track width
$\Delta R(b, Z)$	0.01037	ΔR between b -quark and Z boson candidates
p_T^Z	0.008122	Z boson candidate transverse momentum
$\frac{\mu^{\text{soft topocone40}}}{SMT \text{ jet } p_T}$	0.0075	Ratio between the soft muon topocone40 and SMT-jet pT
$SMT \text{ jet EMF}$	0.006978	SMT-jet Electromagnetic Fraction
$\Delta R(\mu^{\text{soft}}, Z)$	0.006596	ΔR between soft muon and Z boson candidates
$p_T^{\ell 2}$	0.006018	Sub-leading lepton p_T
$SMT \text{ jet Width}$	0.005493	SMT-jet width
η^b	0.004975	b -quark candidate pseudorapidity
η^q	0.004738	c -quark candidate pseudorapidity
p_T^W	0.003908	W boson candidate transverse momentum
$p_T^{\ell 3}$	0.00314	Third lepton p_T
$\eta^{\ell 1}$	0.002857	Leading lepton η
$\eta^{\ell 2}$	0.001557	Sub-leading lepton η
$\eta^{\ell 3}$	0.001484	Third lepton η
$SMT \text{ jet Charge}$	0.0004037	SMT-jet charge

Table D.3 – Final set of input variables considered in the training of the GBDT in SR3 to built the D_3 discriminant. Variables are ordered by the separation $\langle s^2 \rangle$ value.

Variable	$\langle s^2 \rangle$	Definition
$m_{b\ell\nu}$	0.1717	SM top-quark candidate mass
$N b\text{ jets}$	0.08218	Number of b-jets tagged with DL1r
$m_{q\ell\ell}$	0.07019	FCNC top-quark candidate mass
$\frac{\mu^{\text{soft}} ID p_T}{SMT \text{ jet Sum} p_T \text{ Trk}}$	0.03357	Ratio between the soft muon ID pT and pT sum of tracks
$\Delta R(\ell, Z)$	0.03141	ΔR between W boson lepton and Z boson candidates
$\Delta R(t_{SM}, t_{FCNC})$	0.02508	ΔR between SM and FCNC top-quark candidates
$\Delta R(\mu^{\text{soft}}, Z)$	0.006596	ΔR between soft muon and Z boson candidates

Signal SR3



Background SR3

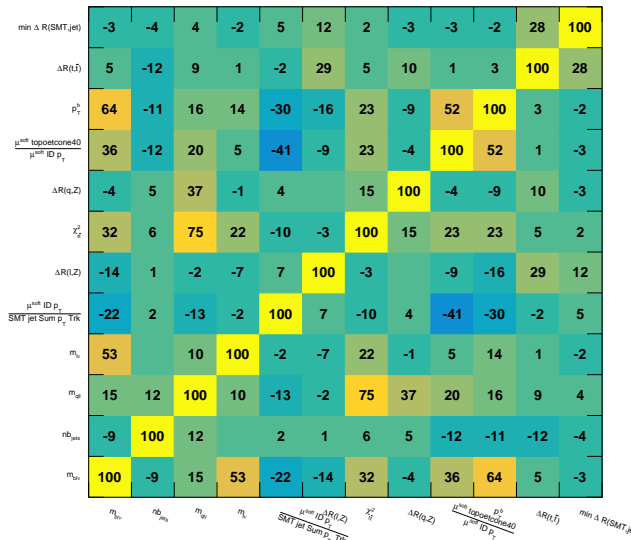


Figure D.1 – Correlation matrix of the input variables from signal (top) and background (bottom) samples considered in the training of the GBDT in SR3 to built the D_3 discriminant for tZc coupling search.

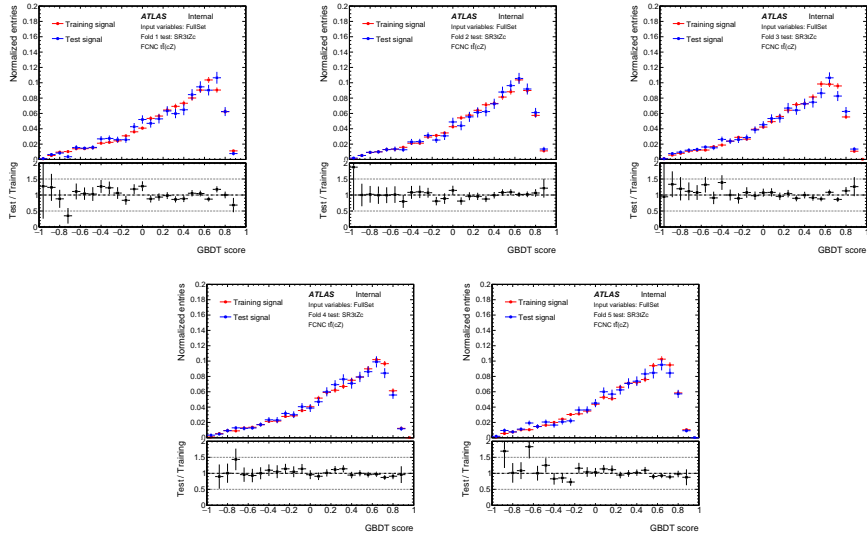


Figure D.2 – The FCNC $t\bar{t}$ decay signal GBDT output score distribution for each of five GBDTs trained in SR3 for the D_3 discriminant. Initial (full) set of input variables is used in the training. Comparing results between training and test samples.

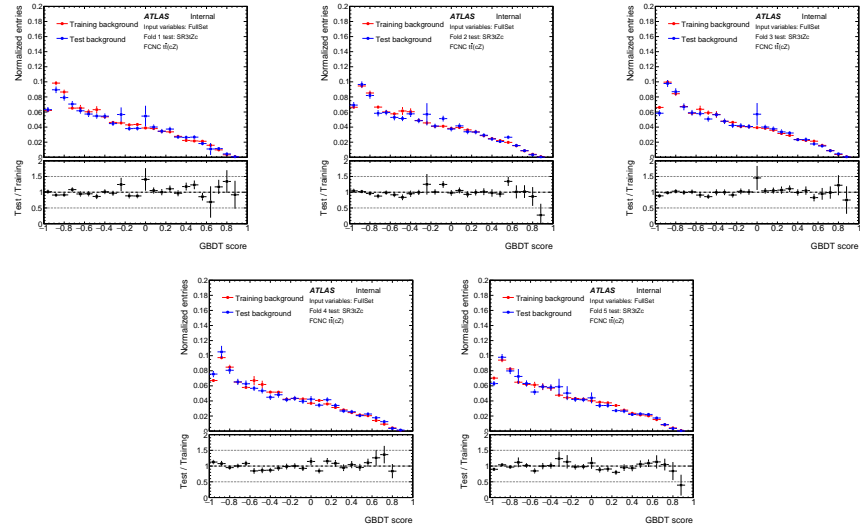


Figure D.3 – The background GBDT output score distribution for each of five GBDTs trained in SR3 for the D_3 discriminant. Initial (full) set of input variables is used in the training. Comparing results between training and test samples.

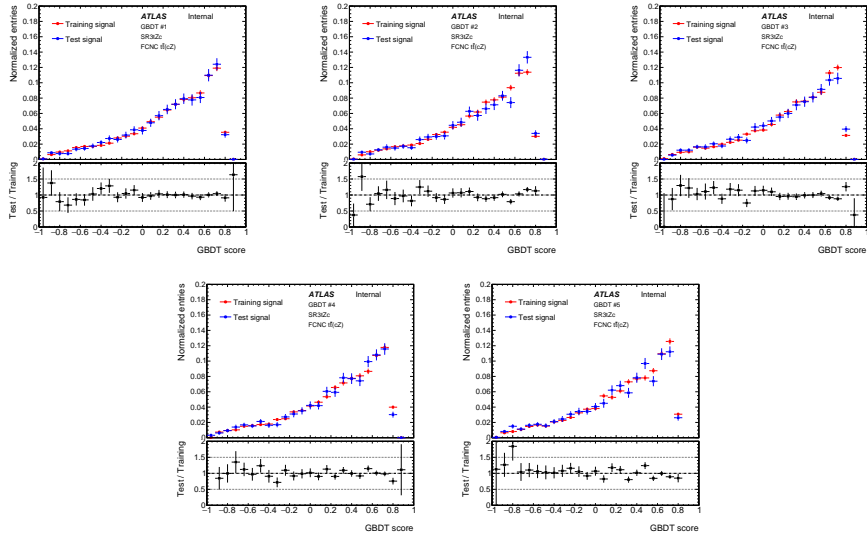


Figure D.4 – The FCNC $t\bar{t}$ decay signal GBDT output score distribution for each of five GBDTs trained in SR3 for the D_3 discriminant. Final set of input variables is used in the training. Comparing results between training and test samples.

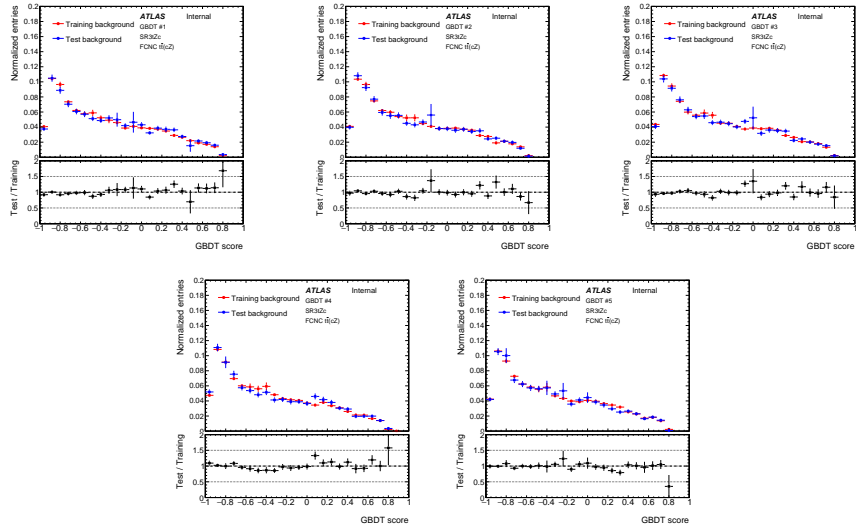


Figure D.5 – The background GBDT output score distribution for each of five GBDTs trained in SR3 for the D_3 discriminant. Final set of input variables is used in the training. Comparing results between training and test samples.

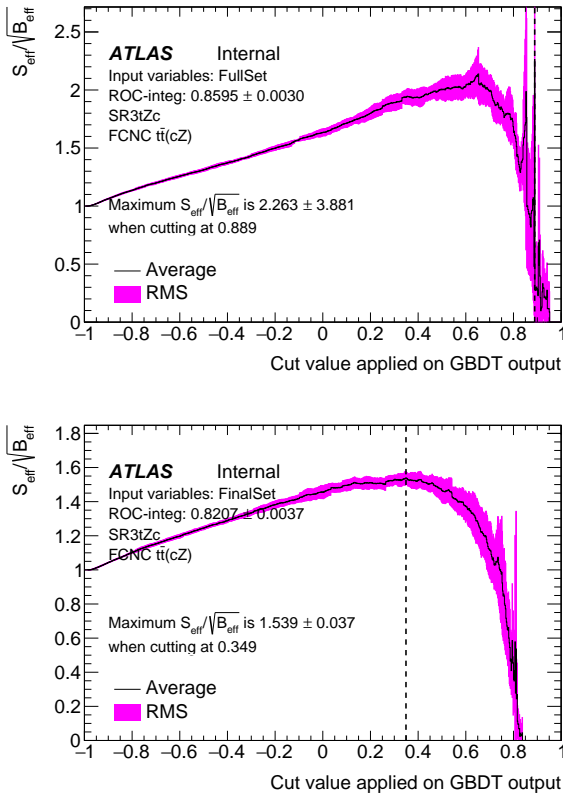


Figure D.6 – The $S_{\text{eff}}/\sqrt{B_{\text{eff}}}$ value averaged over the validation folds as a function of the cut on the BDT output score with full set (up) and final set (down) of input variables in the SR3.

D.2 Hyper-parameters optimisation

Once the final set of input variables are defined, the BDT hyper-parameters optimisation is performed. The following BDT paremeters [145] and values are considered with total of 144 combination: NTrees=[400,600,800,1000], minNodSize=[2.0,4.0,6.0], shrinkage=[0.025,0.05,0.1], maxDepth=[1,2,4]. Figure D.7 presents the maximum value of $S_{\text{eff}}/\sqrt{B_{\text{eff}}}$ by cutting the BDT output score, and the ROC integral, averaged over the validation folds, as a function of BDT hyper-parameters combination.

The difference between highest and lowest values of ROC integral with the different BDT hyper-parameters combinations is $\sim 2\%$. These result indicate that the BDT performance is stable and not much can be improved with the hyper-parameters.

The average ROC integral (0.8207 with RMS of 0.0037) obtained with the reference BDT parameters (see table D.1) is almost identical to the highest value of ROC integral (0.8255 with RMS of 0.0028) obtained from the hyper-parameters optimisation.

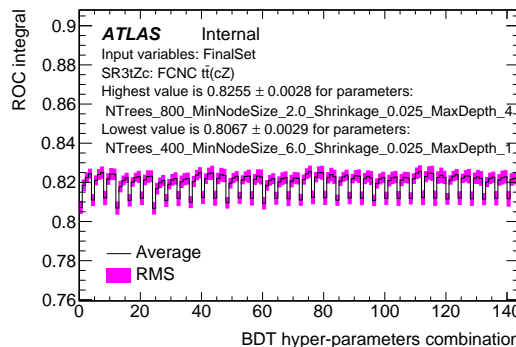


Figure D.7 – ROC integral, averaged over the validation folds, as a function of BDT hyper-parameters combination in the SR3. The highest and lowest values of $S_{\text{eff}}/\sqrt{B_{\text{eff}}}$ and ROC integral are presented on the plots as well as the corresponding BDT parameters values.

APPENDIX E

Kinematic distributions in the Signal Regions

This appendix shows some kinematic distributions in the Signal Regions:

- SR1tZc (Section [E.1](#));
- SR2tZc (Section [E.2](#));
- SR3tZc using DL1r_c (Section [E.3](#));

E.1 SR1tZc

Figures E.1 and E.2 show the distributions of kinematic variables for events selected in the SR1tZc.

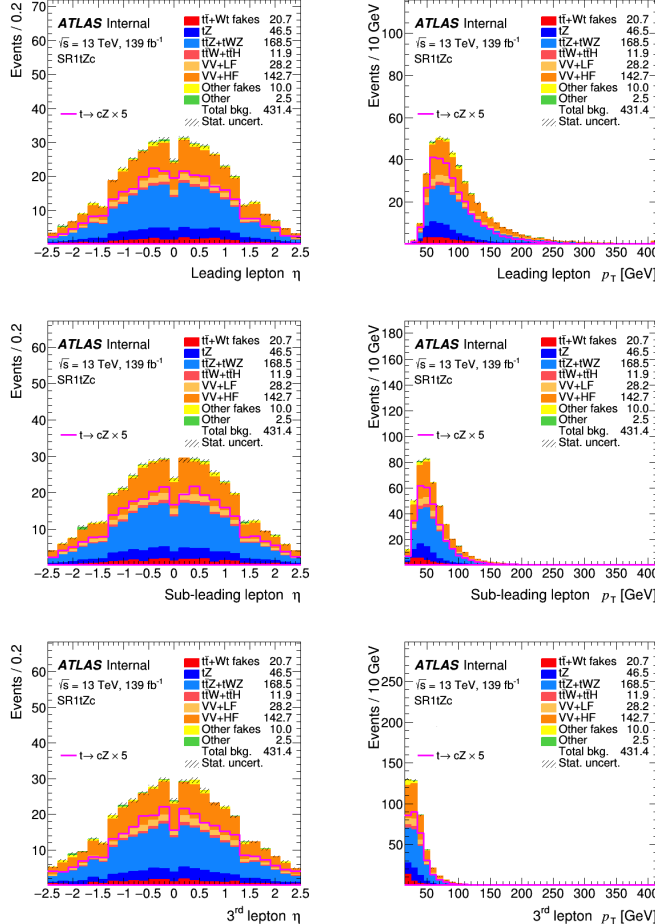


Figure E.1 – Pre-fit distributions of kinematic variables of leptons for events selected in the SR1tZc. The uncertainty band includes only the statistical uncertainty. These distributions are blinded, following the blinding strategy.

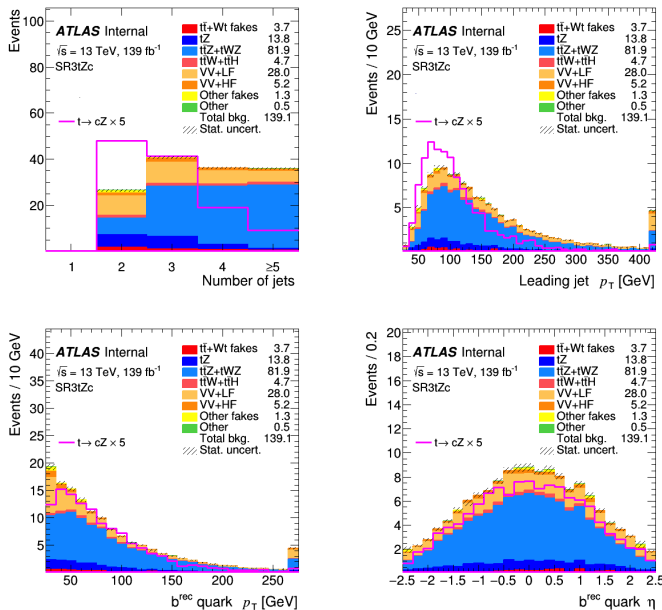


Figure E.2 – Pre-fit distributions of kinematic variables of jets for events selected in the SR1tZc. The uncertainty band includes only the statistical uncertainty. These distributions are blinded, following the blinding strategy.

E.2 SR2tZc

Figures E.3 and E.4 show the distributions of kinematic variables for events selected in the SR1tZc.

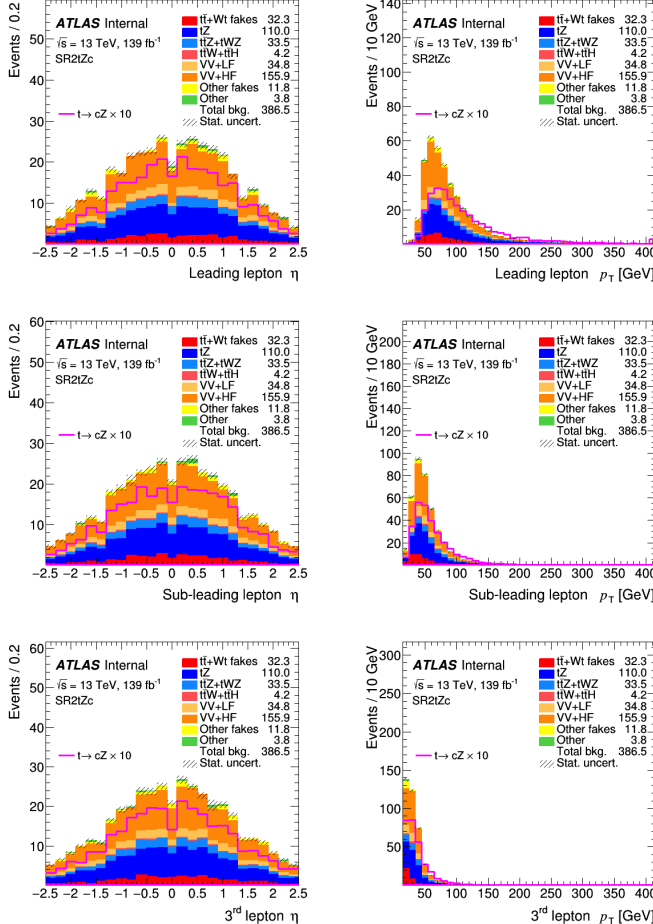


Figure E.3 – Pre-fit distributions of kinematic variables of leptons for events selected in the SR2tZc. The uncertainty band includes only the statistical uncertainty. These distributions are blinded, following the blinding strategy.

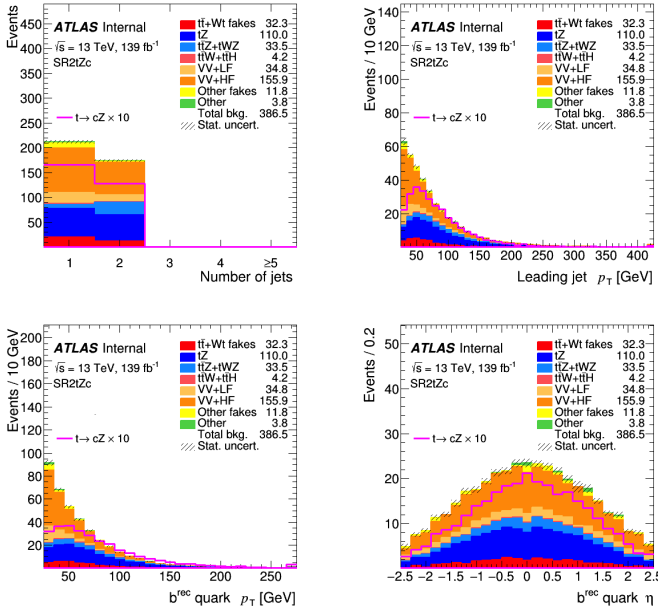


Figure E.4 – Pre-fit distributions of kinematic variables of jets for events selected in the SR2tZc. The uncertainty band includes only the statistical uncertainty. These distributions are blinded, following the blinding strategy.

E.3 SR3tZc

Figures E.5 and E.6 show the distributions of kinematic variables for events selected in the SR3tZc.

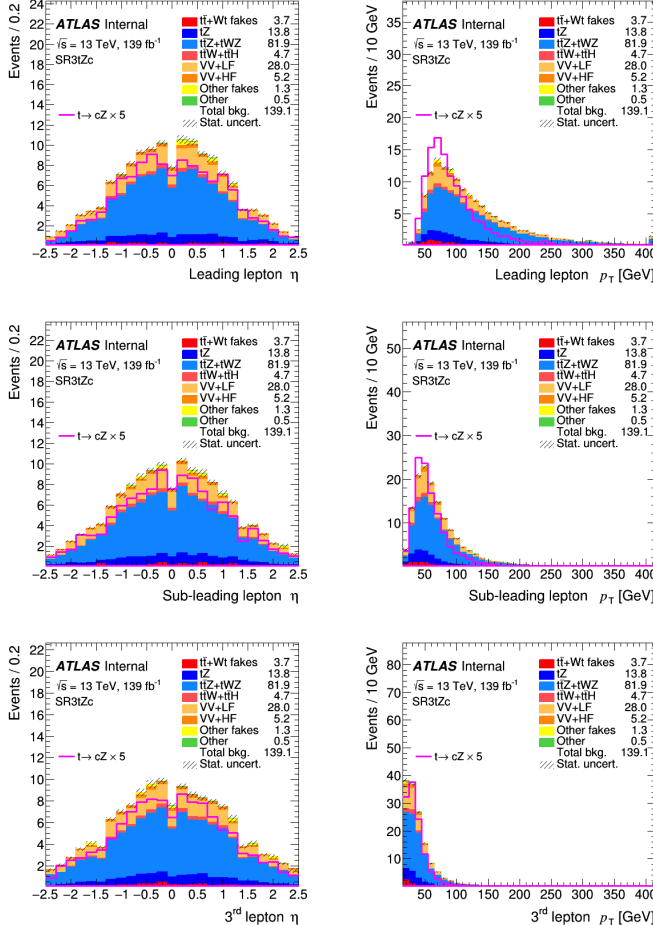


Figure E.5 – Pre-fit distributions of kinematic variables of leptons for events selected in the SR3tZc. The uncertainty band includes only the statistical uncertainty. These distributions are blinded, following the blinding strategy.

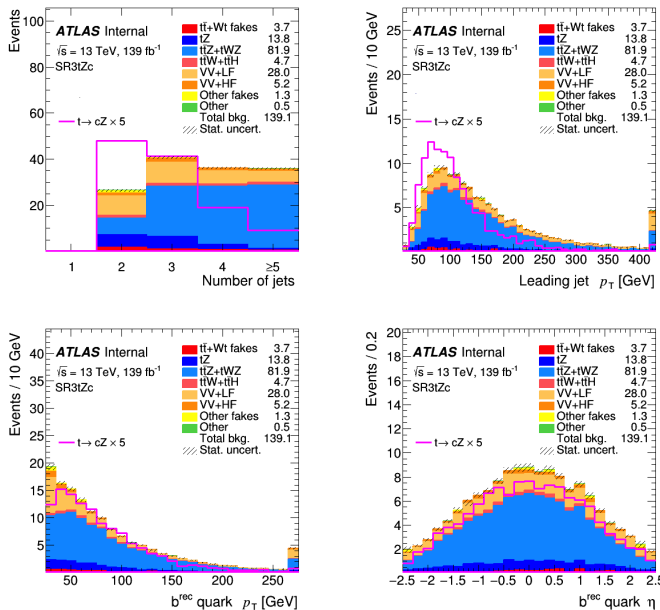


Figure E.6 – Pre-fit distributions of kinematic variables of jets for events selected in the SR3tZc. The uncertainty band includes only the statistical uncertainty. These distributions are blinded, following the blinding strategy.

APPENDIX F

Kinematic distributions in the Control Regions

This appendix shows some kinematic distributions in the Control Regions:

- $t\bar{t}$ CR (Section [F.1](#));
- $t\bar{t}Z$ CR (Section [F.2](#));
- Side-band CR1 (Section [F.3](#));
- Side-band CR2 (Section [F.4](#));

F.1 $t\bar{t}$ CR

Figures F.1 and F.2 show the distributions of kinematic variables for events selected in the $t\bar{t}$ CR region.

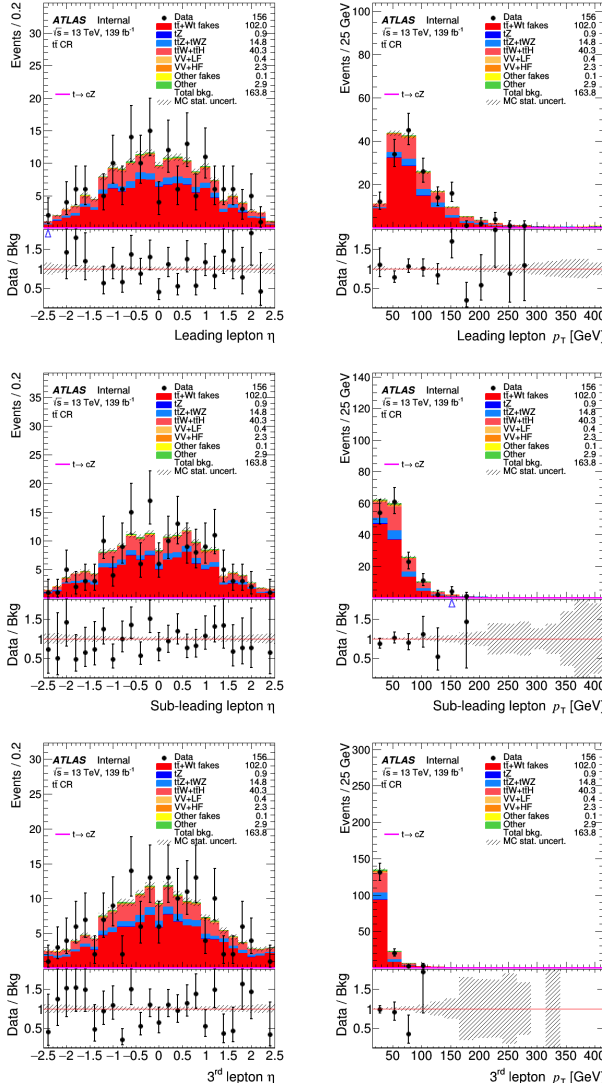


Figure F.1 – Pre-fit distributions of kinematic variables of leptons for events selected in the $t\bar{t}$ CR. The uncertainty band includes only the statistical uncertainty.

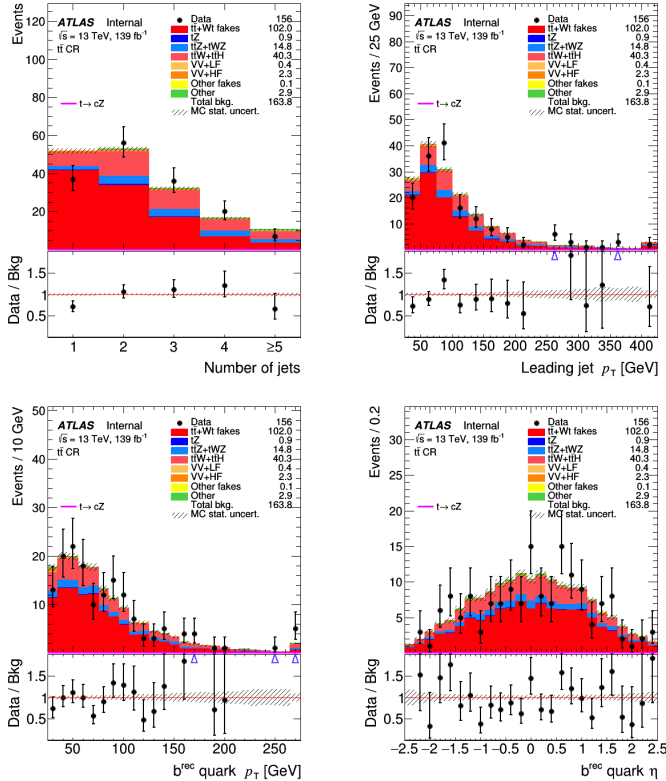


Figure F.2 – Pre-fit distributions of kinematic variables of jets for events selected in the $t\bar{t}$ CR. The uncertainty band includes only the statistical uncertainty.

F.2 $t\bar{t}Z$ CR

Figures F.3 and F.4 show the distributions of kinematic variables for events selected in the $t\bar{t}Z$ CR region.

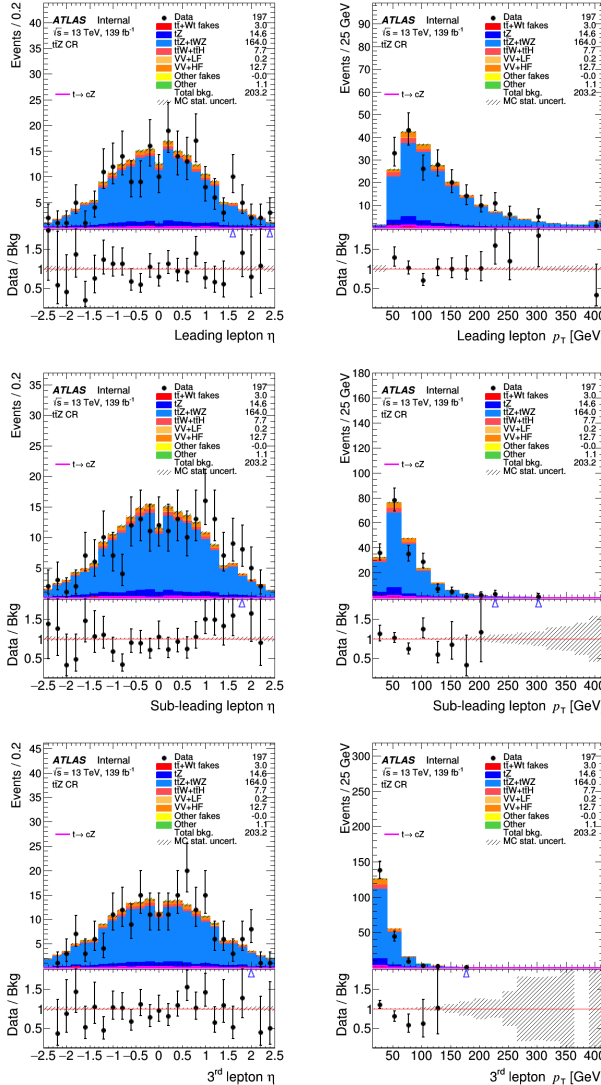


Figure F.3 – Pre-fit distributions of kinematic variables of leptons for events selected in the $t\bar{t}Z$ CR. The uncertainty band includes only the statistical uncertainty.

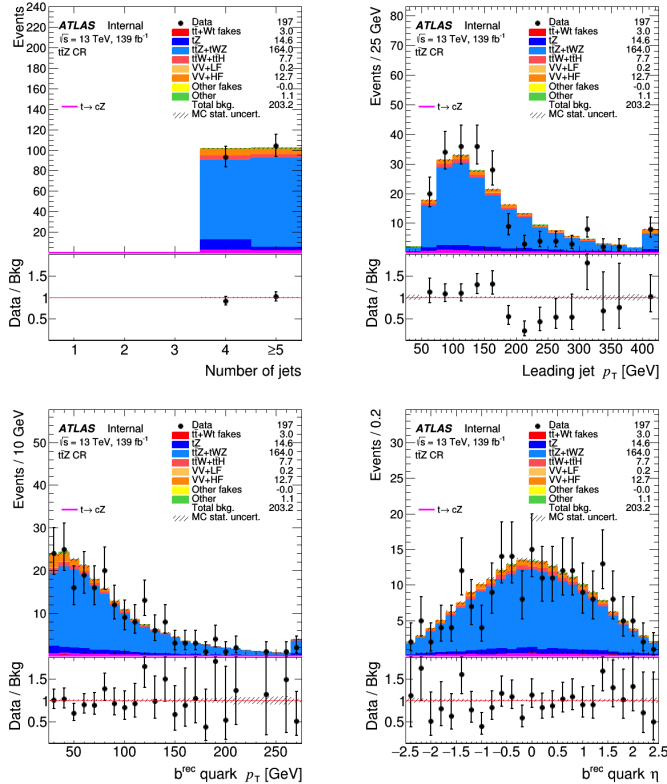


Figure F.4 – Pre-fit distributions of kinematic variables of jets for events selected in the t \bar{t} Z CR. The uncertainty band includes only the statistical uncertainty.

F.3 Side-band CR1

Figures F.5 and F.6 show the distributions of kinematic variables for events selected in the side-band CR1 region.

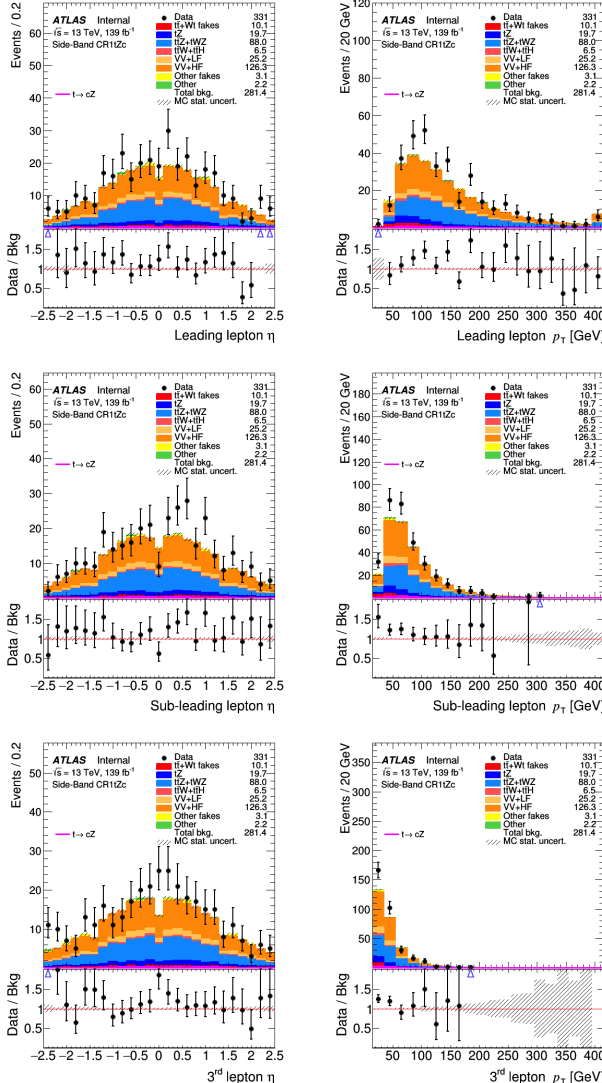


Figure F.5 – Pre-fit distributions of kinematic variables of leptons for events selected in the side-band CR1 region. The uncertainty band includes only the statistical uncertainty.

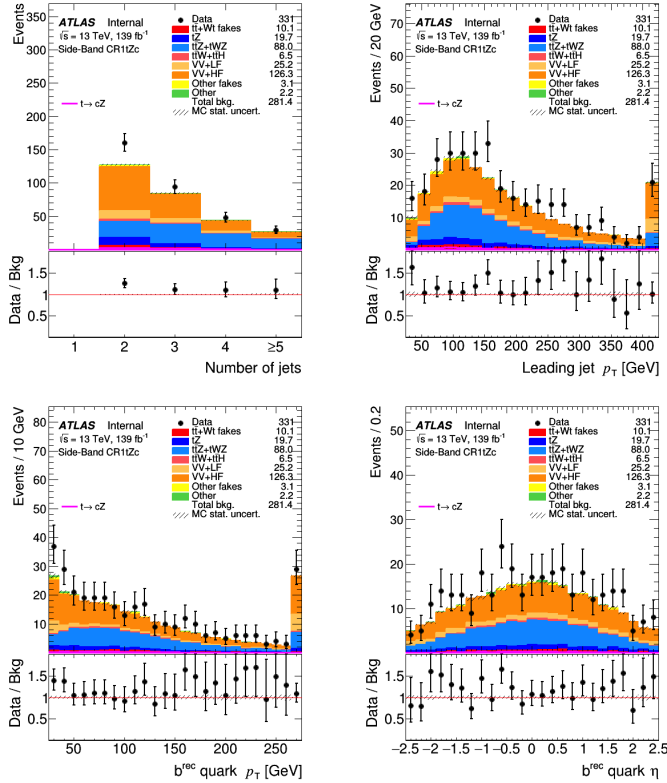


Figure F.6 – Pre-fit distributions of kinematic variables of jets for events selected in the side-band CR1 region. The uncertainty band includes only the statistical uncertainty.

F.4 Side-band CR2

Figures F.7 and F.8 show the distributions of kinematic variables for events selected in the side-band CR2 region.

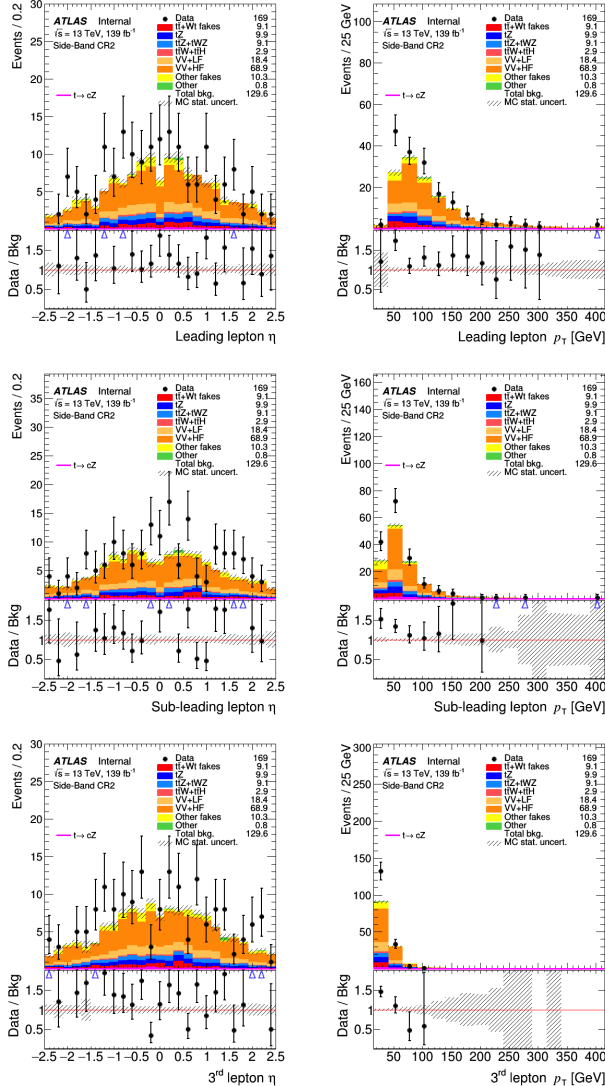


Figure F.7 – Pre-fit distributions of kinematic variables of leptons for events selected in the side-band CR2 region. The uncertainty band includes only the statistical uncertainty.

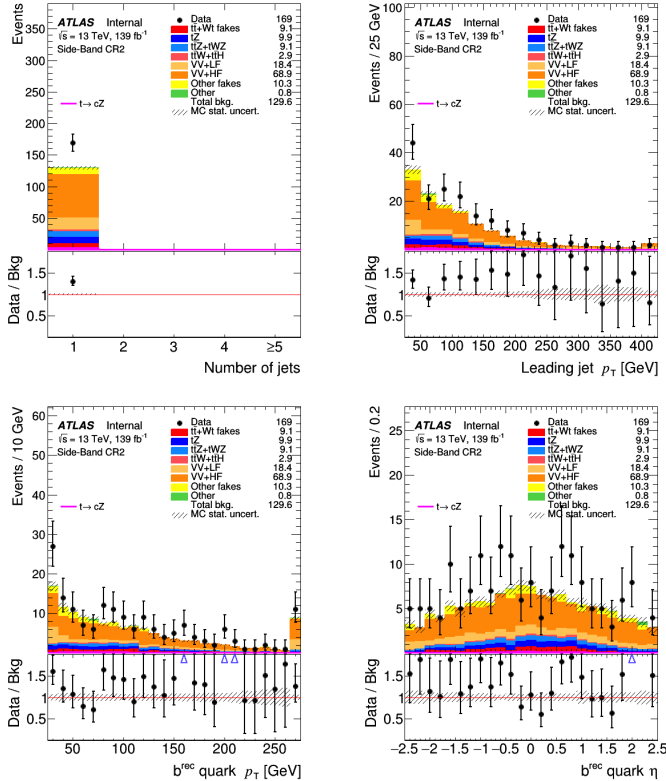


Figure F.8 – Pre-fit distributions of kinematic variables of jets for events selected in the side-band CR2 region. The uncertainty band includes only the statistical uncertainty.

APPENDIX G

Background only fit in CRs

To check the background modeling and extract realistic background normalisations, a CRs-only background-only fit using real data in CRs is performed.

A summary of plots shown in the following:

- The value of the post-fit normalisation parameters of the free floating background is shown in fig. G.1.
- The pull distributions of the all nuisance parameters can be seen in Figures G.2 and G.3 and Figure G.4.
- The list of the systematic shapes that are dropped from the fit for each sample and for each region is shown in Figure G.5.
- Event yields pre- and post-fit are shown in Tables G.1 and G.2.
- Pre-fit and post-fit distributions of the fitted distributions in the various regions are shown in Figures G.6 and G.7.

As shown in fig. G.1, the $t\bar{t}$ scale factor is 0.93 ± 0.25 , compatible with unity. Also, the $VV + HF$ normalisation is pulled up (fig. G.3), driven by the prediction being lower than data in the side-band CRs (tables G.1 and G.2). Since this fit uses real data in CRs, some pulls and constraints of the NPs are expected. For the NPs for the instrumental uncertainties, no significant pulls nor constraints are present (fig. G.2), while some NPs for the modeling uncertainties can be seen (fig. G.3), in particular for the $t\bar{t}$ and diboson backgrounds. After the fit, there is an overall good agreement between data and the prediction, as it can be seen in the post-fit event yields (table G.2) and in the distribution of the fitted variables in the CRs (figs. G.6 and G.7).

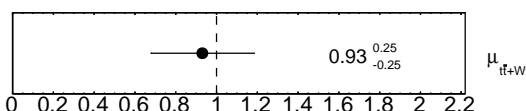


Figure G.1 – Normalisation factors for the B-only tZc fit in CRs.

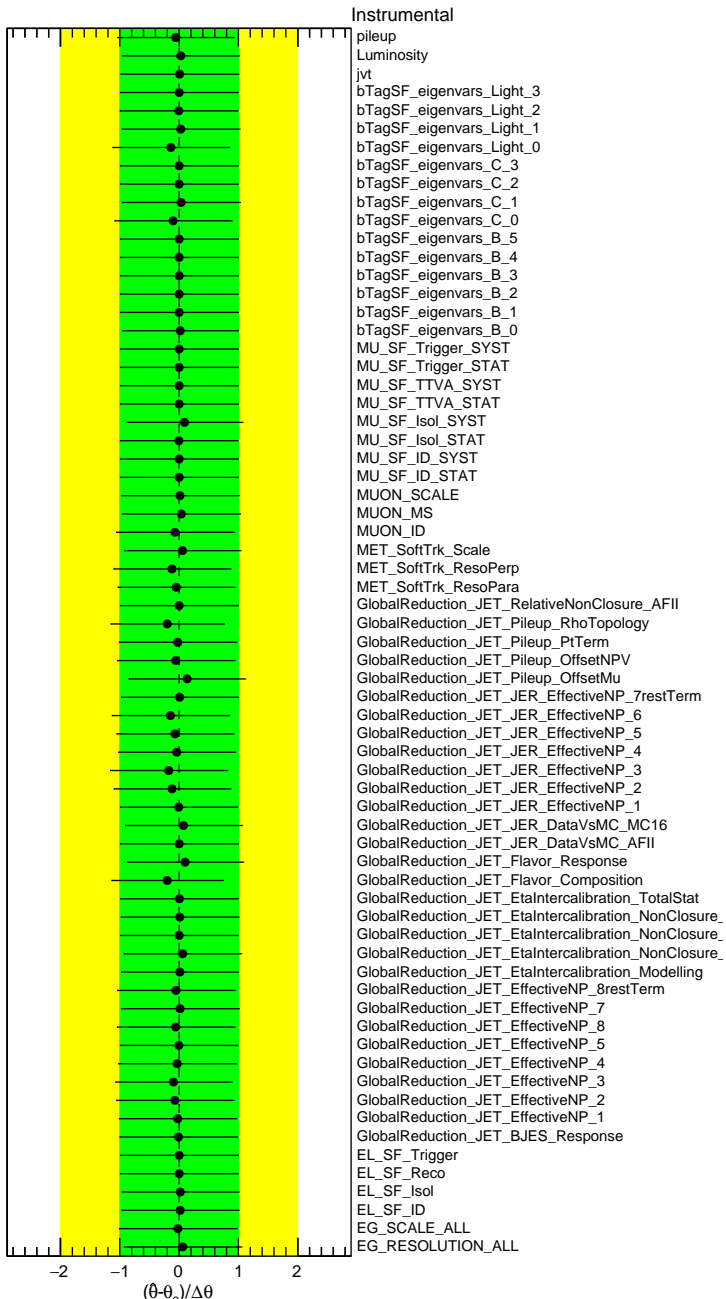


Figure G.2 – Pulls and constraints of the instrumental nuisance parameters for the B-only tZc fit in CRs.

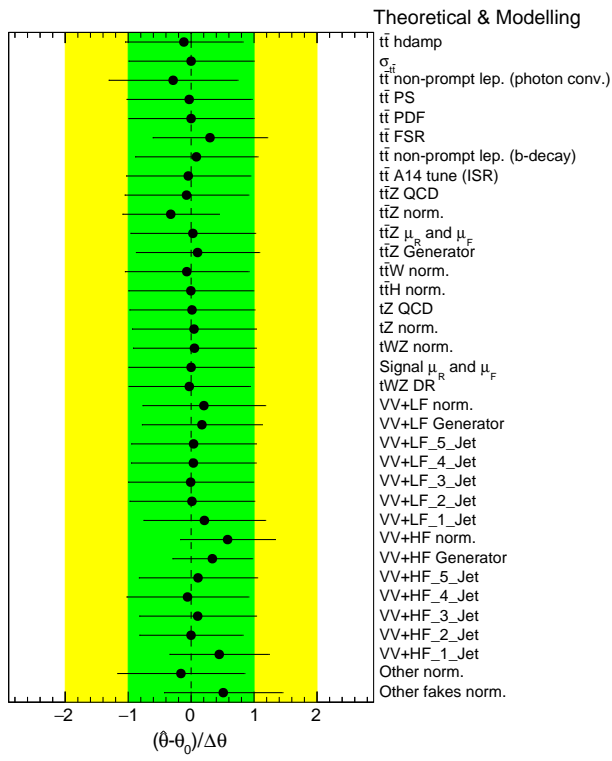


Figure G.3 – Pulls and constraints of the theoretical and modeling nuisance parameters for the B-only tZc fit in CRs.

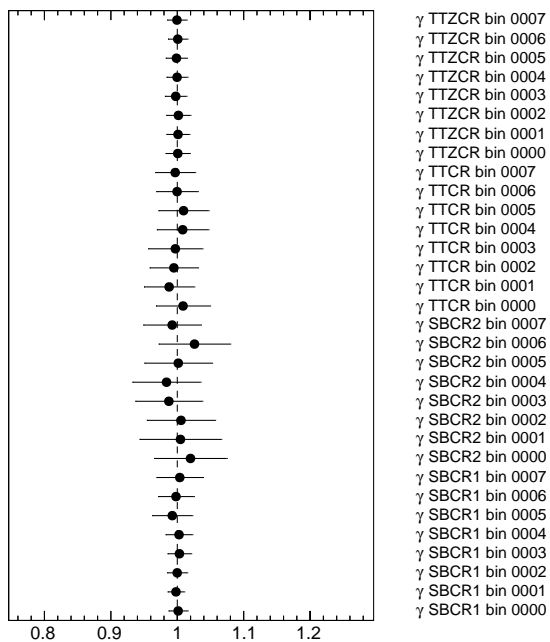


Figure G.4 – Gamma parameters for the B-only tZc fit in CRs.

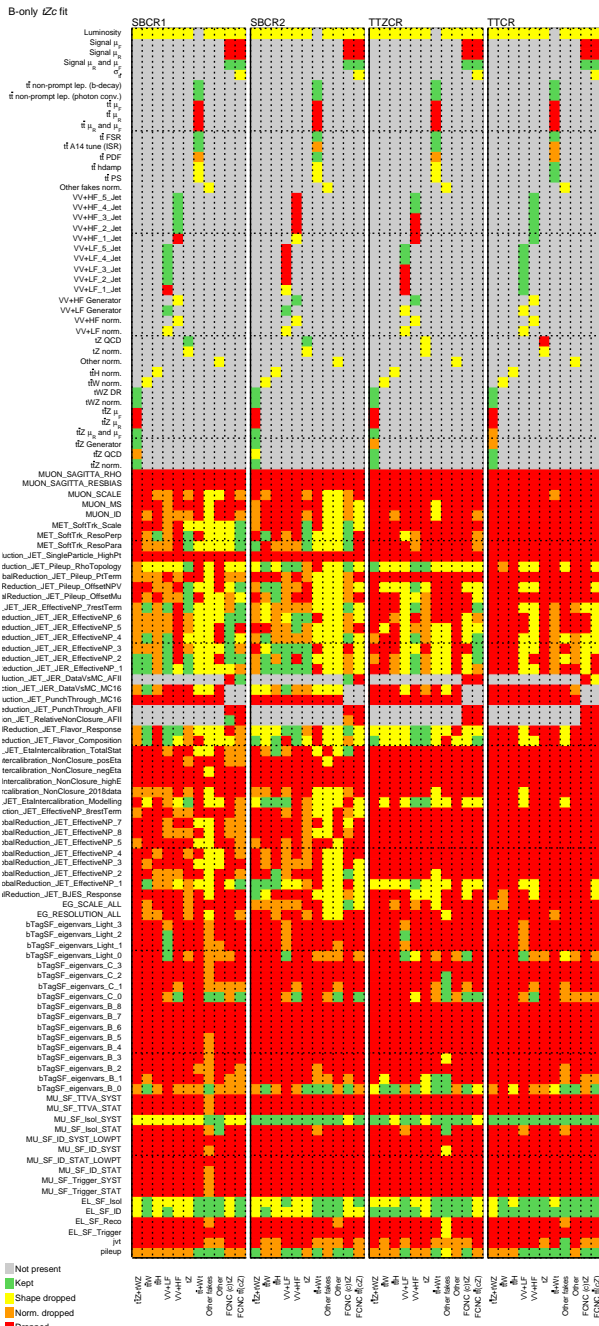


Figure G.5 – Pruning of the nuisance parameters for the B-only tZc fit in CRs.

	Side-band CR1	Side-band CR2	t̄Z CR	t̄t CR
t̄Z +tWZ	88 ± 12	9.1 ± 2.1	164 ± 22	14.8 ± 1.9
t̄tW	4.3 ± 0.7	2.5 ± 0.5	2.3 ± 0.5	27 ± 4
t̄tH	2.3 ± 0.4	0.36 ± 0.07	5.4 ± 0.9	13.8 ± 2.1
VV + LF	25 ± 15	18 ± 7	0.20 ± 0.22	0.40 ± 0.21
VV + HF	130 ± 80	69 ± 28	13 ± 11	2.3 ± 1.4
tZq	20 ± 4	9.9 ± 1.7	14.6 ± 2.9	0.90 ± 0.15
t̄t +Wt	10 ± 4	9.1 ± 2.7	3.0 ± 1.2	102 ± 24
Other fakes	3 ± 5	10 ± 11	0.00 ± 0.06	0.12 ± 0.14
Other	2.2 ± 1.6	0.8 ± 2.6	1.1 ± 0.5	2.9 ± 1.5
Total background	280 ± 80	130 ± 32	203 ± 27	164 ± 25
Data	331	169	197	156
Data / Bkg.	1.18 ± 0.35	1.30 ± 0.34	0.97 ± 0.14	0.95 ± 0.16

Table G.1 – Pre-fit event yields in the CRs for the B-only fit for the tZc coupling extraction. The error includes both statistical and systematic uncertainties.

	Side-band CR1	Side-band CR2	t̄Z CR	t̄t CR
t̄Z +tWZ	86 ± 10	9.3 ± 2.1	157 ± 13	14.4 ± 1.4
t̄tW	4.2 ± 0.7	2.5 ± 0.5	2.2 ± 0.4	26 ± 4
t̄tH	2.3 ± 0.4	0.37 ± 0.07	5.3 ± 0.8	13.8 ± 2.1
VV + LF	29 ± 16	21 ± 8	0.23 ± 0.23	0.40 ± 0.19
VV + HF	172 ± 28	94 ± 18	18 ± 7	3.3 ± 0.6
tZq	20 ± 4	10.1 ± 1.7	14.4 ± 2.7	0.91 ± 0.13
t̄t +Wt	9.4 ± 2.9	8.6 ± 1.7	2.5 ± 0.8	95 ± 13
Other fakes	5 ± 5	18 ± 16	0.006 ± 0.009	0.18 ± 0.15
Other	1.8 ± 1.2	0.3 ± 0.9	1.0 ± 0.5	2.7 ± 1.4
Total background	329 ± 20	165 ± 14	201 ± 13	157 ± 12
Data	331	169	197	156
Data / Bkg.	1.01 ± 0.06	1.02 ± 0.09	0.98 ± 0.06	0.99 ± 0.08

Table G.2 – Post-fit event yields in the CRs for the B-only fit for the tZc coupling extraction. The error includes both statistical and systematic uncertainties.

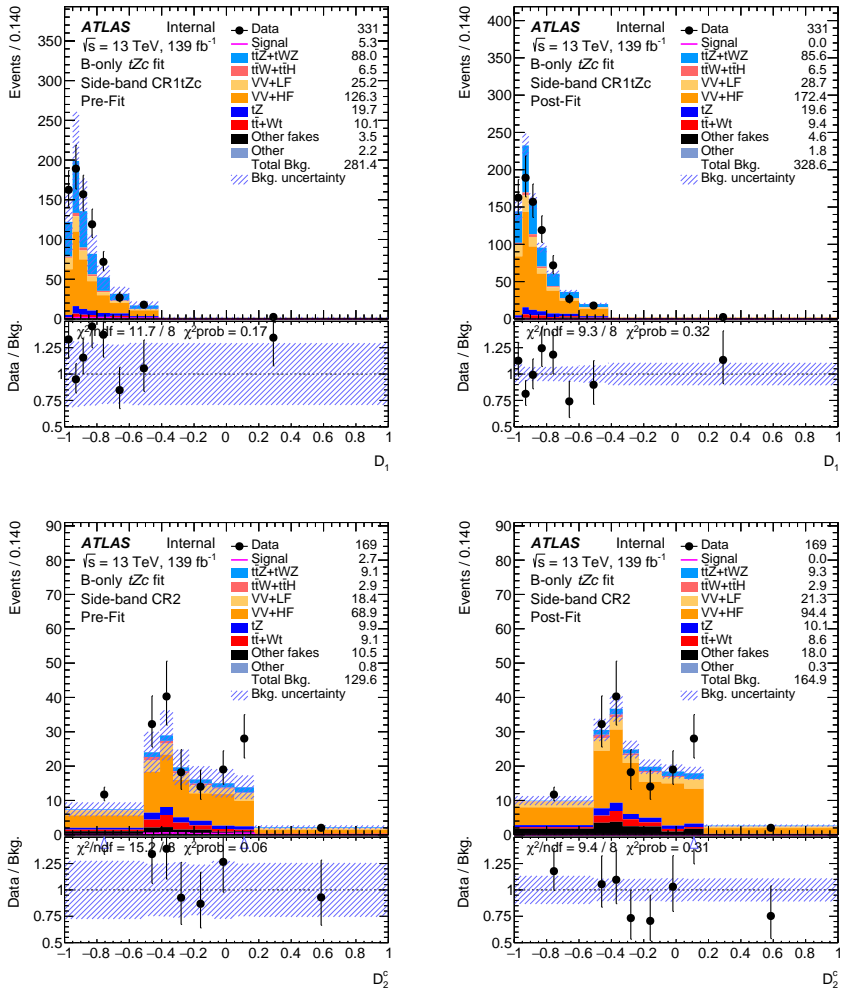


Figure G.6 – Pre-fit (left) and post-fit (right) BDTG output distributions in the side-band CRs for the B-only $t\bar{Z}c$ fit in CRs. The uncertainty band includes both statistical and systematic uncertainties.

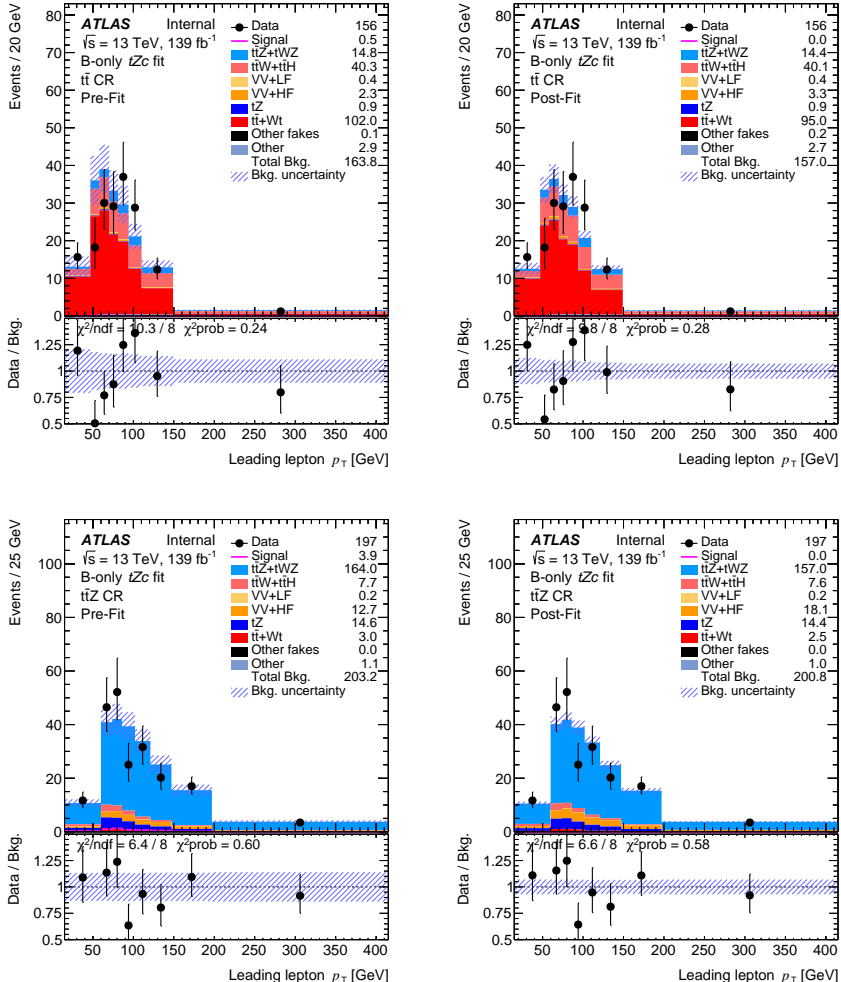


Figure G.7 – Pre-fit (left) and post-fit (right) leading lepton p_T distributions in the $t\bar{t}$ and tZ CRs for the B-only tZc fit in CRs. The uncertainty band includes both statistical and systematic uncertainties.

References

- [1] E. Fermi, *Il Nuovo Cimento* (1934) **11**, 1 (2008).
- [2] F. L. Wilson, *Am.J.Phys* **36**, 1150 (1968).
- [3] C. S. Wu, E. Ambler, R. W. Hayward, D. D. Hoppes, and R. P. Hudson, *Phys. Rev.* **105**, 1413 (1957).
- [4] P. Renton, *Electroweak Interactions: An Introduction to the Physics of Quarks and Leptons* (1990).
- [5] S. L. Glashow, J. Iliopoulos, and L. Maiani, *Phys. Rev. D* **2**, 1285 (1970).
- [6] J. Aguilar-Saavedra, “Top flavour-changing neutral interactions: theoretical expectations and experimental detection,” (2004), arXiv:hep-ph/0409342 [hep-ph].
- [7] N. Cabibbo, *Meeting of the Italian School of Physics and Weak Interactions Bologna, Italy, April 26-28, 1984*, *Phys. Rev. Lett.* **10**, 531 (1963).
- [8] M. Kobayashi and T. Maskawa, *Progress of Theoretical Physics* **49**, 652 (1973).
- [9] Z. Ligeti, *Int. J. Mod. Phys. A* **20**, 5105 (2005), arXiv:hep-ph/0408267 [hep-ph].
- [10] F. Abe *et al.* (CDF Collaboration), *Phys. Rev. Lett.* **74**, 2626 (1995).
- [11] S. Abachi *et al.* (D0 Collaboration), *Phys. Rev. Lett.* **74**, 2632 (1995).
- [12] R. Aaij *et al.* (LHCb Collaboration), *Phys. Rev. Lett.* **115**, 112001 (2015).
- [13] M. Tanabashi *et al.* (Particle Data Group), *Phys. Rev. D* **98**, 030001 (2018).
- [14] W. Bernreuther, *J. Phys. G* **35**, 083001 (2008), arXiv:0805.1333 [hep-ph].
- [15] D0 Collaboration website, “Useful Diagrams of Top Signals and Backgrounds,” .
- [16] G. Aad *et al.* (ATLAS), *Phys. Lett. B* **716**, 1 (2012), arXiv:1207.7214 [hep-ex].
- [17] F. Zwicky, *General Relativity and Gravitation* **41**, 207 (2009).

- [18] N. Aghanim *et al.* (Planck), (2018), arXiv:1807.06209 [astro-ph.CO] .
- [19] J. A. Aguilar-Saavedra, Acta Phys. Polon. **B35**, 2695 (2004), arXiv:hep-ph/0409342 [hep-ph] .
- [20] J. A. Aguilar-Saavedra, Phys. Rev. **D67**, 035003 (2003), arXiv:hep-ph/0210112 [hep-ph] .
- [21] D. Atwood, L. Reina, and A. Soni, Phys. Rev. D **55**, 3156 (1997).
- [22] J. J. Cao, G. Eilam, M. Frank, K. Hikasa, G. L. Liu, I. Turan, and J. M. Yang, Phys. Rev. D **75**, 075021 (2007).
- [23] J. M. Yang, B.-L. Young, and X. Zhang, Phys. Rev. D **58**, 055001 (1998).
- [24] K. Agashe, G. Perez, and A. Soni, Phys. Rev. D **75**, 015002 (2007).
- [25] P. Hung, Y.-X. Lin, C. S. Nugroho, and T.-C. Yuan, Nuclear Physics B **927**, 166 (2018).
- [26] K. Agashe *et al.* (Top Quark Working Group) (2013) arXiv:1311.2028 [hep-ph] .
- [27] V. D. Barger, M. S. Berger, and R. J. N. Phillips, Phys. Rev. **D52**, 1663 (1995), arXiv:hep-ph/9503204 [hep-ph] .
- [28] Z. Maki, M. Nakagawa, and S. Sakata, Prog. Theor. Phys. **28**, 870 (1962).
- [29] G. C. Branco, P. M. Ferreira, L. Lavoura, M. N. Rebelo, M. Sher, and J. P. Silva, Phys. Rept. **516**, 1 (2012), arXiv:1106.0034 [hep-ph] .
- [30] G. Couture, C. Hamzaoui, and H. König, Phys. Rev. D **52**, 1713 (1995).
- [31] L. Evans and P. Bryant, Journal of Instrumentation **3**, S08001 (2008).
- [32] E. Mobs, “The CERN accelerator complex - August 2018. Complexe des accélérateurs du CERN,” .
- [33] “LHC public plots,” ATLAS Twiki.
- [34] G. Aad *et al.* (ATLAS), JINST **3**, S08003 (2008).
- [35] The ATLAS collaboration, *ATLAS magnet system: Technical Design Report* (1997).
- [36] The ATLAS collaboration, *ATLAS liquid argon calorimeter: Technical Design Report* (1996).
- [37] The ATLAS collaboration, *ATLAS muon spectrometer : Technical Design Report* (1997).
- [38] The ATLAS collaboration, *ATLAS high-level trigger, data acquisition and controls: Technical Design Report* (2003).
- [39] “LHC upgrades and operation,” CERN Website.
- [40] *Technical Design Report for the Phase-II Upgrade of the ATLAS Muon Spectrometer*, Tech. Rep. CERN-LHCC-2017-017. ATLAS-TDR-026 (CERN, Geneva, 2017).
- [41] T. Kawamoto, S. Vlachos, L. Pontecorvo, J. Dubbert, G. Mikenberg, P. Iengo, C. Dallapiccola, C. Amelung, L. Levinson, R. Richter, and D. Lellouch, *New Small Wheel Technical Design Report*, Tech. Rep. CERN-LHCC-2013-006. ATLAS-TDR-020 (2013) aTLAS New Small Wheel Technical Design Report.
- [42] G. Aielli, C. Amelung, D. Boscherini, R. Cardarelli, M. Corradi, L. Han, V. Izzo, O. Kortner, H. Kroha, D. Levin, L. Massa, L. Paolozzi, R. Santonico, and R. Vari (ATLAS Collaboration), *The ATLAS BIS78 Project*, Tech. Rep. ATL-MUON-INT-2016-002 (CERN, Geneva, 2016).

- [43] ATLAS Collaboration (ATLAS), *muTrigNt_write code*, Tech. Rep.
- [44] ATLAS Collaboration (ATLAS), *Muon Upgrade Studies Twiki*, Tech. Rep.
- [45] L.Marcoccia, *Phase II Upgrade : High-eta tagger + RPC (Muon Week)*, Tech. Rep. (2018).
- [46] L. Marcoccia, *Efficiency studies on emulated RPC for the Phase-II Upgrade of the ATLAS Muon Spectrometer*, Tech. Rep. ATL-COM-MUON-2019-060 (CERN, Geneva, 2019).
- [47] B. Andersson, G. Gustafson, G. Ingelman, and T. Sjöstrand, *Physics Reports* **97**, 31 (1983).
- [48] G. Marchesini and B. Webber, *Nuclear Physics B* **238**, 1 (1984).
- [49] T. Sjöstrand, S. Mrenna, and P. Skands, *Journal of High Energy Physics* **2006**, 026 (2006).
- [50] M. Bähr, S. Gieseke, M. A. Gigg, D. Grellscheid, K. Hamilton, O. Latunde-Dada, S. Plätzer, P. Richardson, M. H. Seymour, A. Sherstnev, and B. R. Webber, *The European Physical Journal C* **58**, 639 (2008).
- [51] S. Agostinelli *et al.* (GEANT4), *Nucl. Instrum. Meth. A* **506**, 250 (2003).
- [52] E. Richter-Was, D. Froidevaux, and L. Poggioli, *ATLFAST 2.0 a fast simulation package for ATLAS*, Tech. Rep. ATL-PHYS-98-131 (CERN, Geneva, 1998).
- [53] ATLAS Collaboration, “Electron identification measurements in ATLAS using $\sqrt{s} = 13$ TeV data with 50 ns bunch spacing,” ATL-PHYS-PUB-2015-041 (2015).
- [54] ATLAS Collaboration, “Electron and photon energy calibration with the ATLAS detector using data collected in 2015 at $\sqrt{s} = 13$ TeV,” ATL-PHYS-PUB-2016-015 (2016).
- [55] ATLAS Collaboration, “Electron efficiency measurements with the ATLAS detector using the 2015 LHC proton–proton collision data,” ATLAS-CONF-2016-024 (2016).
- [56] ATLAS Collaboration, *Eur. Phys. J. C* **79**, 639 (2019), arXiv:1902.04655 [hep-ex].
- [57] ATLAS Collaboration, *Eur. Phys. J. C* **76**, 292 (2016), arXiv:1603.05598 [hep-ex].
- [58] *Muon Combined Performance in Run 2 (25 ns runs)*, Tech. Rep. ATL-COM-MUON-2015-093 (Geneva, 2015).
- [59] *Calibration of the Soft Muon Tagger in Run-2 data*, Tech. Rep. ATL-COM-PHYS-2017-1110 (CERN, Geneva, 2017) updates to be expected.
- [60] ATLAS Collaboration, *Eur. Phys. J. C* **77**, 466 (2017), arXiv:1703.10485 [hep-ex].
- [61] ATLAS Collaboration, “Tagging and suppression of pileup jets with the ATLAS detector,” ATLAS-CONF-2014-018 (2014).
- [62] *Optimisation and performance studies of the ATLAS b-tagging algorithms for the 2017-18 LHC run*, Tech. Rep. ATL-PHYS-PUB-2017-013 (CERN, Geneva, 2017).
- [63] G. Aad *et al.* (ATLAS), *Eur. Phys. J. C* **79**, 970 (2019), arXiv:1907.05120 [hep-ex].
- [64] F. Chollet *et al.*, “Keras,” <https://keras.io>.
- [65] T. T. D. Team *et al.*, “Theano: A python framework for fast computation of mathematical expressions,” (2016), arXiv:1605.02688 [cs.SC].

- [66] D. P. Kingma and J. Ba, “Adam: A method for stochastic optimization,” (2017), arXiv:1412.6980 [cs.LG].
- [67] I. J. Goodfellow, D. Warde-Farley, M. Mirza, A. Courville, and Y. Bengio, “Maxout networks,” (2013), arXiv:1302.4389 [stat.ML].
- [68] ATLAS Collaboration, “tc+MET: charm tagger definition,” .
- [69] G. Aad *et al.* (ATLAS), Eur. Phys. J. C **77**, 241 (2017), arXiv:1609.09324 [hep-ex].
- [70] A. Collaboration, The European Physical Journal C **77**, 241 (2017).
- [71] ATLAS Collaboration, Eur. Phys. J. C **72**, 1844 (2012), arXiv:1108.5602 [hep-ex].
- [72] ATLAS Collaboration, Eur. Phys. J. C **77**, 241 (2017), arXiv:1609.09324 [hep-ex].
- [73] ATLAS Collaboration, “Performance of missing transverse momentum reconstruction with the ATLAS detector in the first proton–proton collisions at $\sqrt{s} = 13$ TeV,” ATL-PHYS-PUB-2015-027 (2015).
- [74] D. Adams *et al.*, *Recommendations of the Physics Objects and Analysis Harmonisation Study Groups 2014*, Tech. Rep. ATL-PHYS-INT-2014-018 (CERN, Geneva, 2014).
- [75] “Associationutils,” <https://svnweb.cern.ch>.
- [76] C. Patrignani *et al.* (ParticleDataGroup), Phys. Rev. D **98**, 030001, 1898 p (2018).
- [77] A. Heister *et al.* (ALEPH), Phys. Lett. B **543**, 173 (2002), arXiv:hep-ex/0206070 [hep-ex].
- [78] J. Abdallah *et al.* (DELPHI), Phys. Lett. B **590**, 21 (2004), arXiv:hep-ex/0404014 [hep-ex].
- [79] G. Abbiendi *et al.* (OPAL), Phys. Lett. B **521**, 181 (2001), arXiv:hep-ex/0110009 [hep-ex].
- [80] P. Achard *et al.* (L3), Phys. Lett. B **549**, 290 (2002), arXiv:hep-ex/0210041 [hep-ex].
- [81] H. Abramowicz *et al.* (ZEUS), Phys. Lett. B **708**, 27 (2012), arXiv:1111.3901 [hep-ex].
- [82] D0 Collaboration (D0), Phys. Lett. B **701**, 313 (2011), arXiv:1103.4574 [hep-ex].
- [83] ATLAS Collaboration, JHEP **07**, 176 (2018), arXiv:1803.09923 [hep-ex].
- [84] CMS Collaboration (CMS), Phys. Rev. Lett. **112**, 171802 (2014), arXiv:1312.4194 [hep-ex].
- [85] CMS Collaboration, JHEP **07**, 003 (2017), arXiv:1702.01404 [hep-ex].
- [86] M. Barros *et al.*, Eur. Phys. J. Plus **135**, 339 (2020).
- [87] TopWG Blinding Guidelines, “<https://twiki.cern.ch>,” .
- [88] TOPQ derivations, “<https://twiki.cern.ch>,” .
- [89] ATLAS Collaboration, Eur. Phys. J. C **77**, 317 (2017), arXiv:1611.09661 [hep-ex].
- [90] ATLAS Collaboration, “2015 start-up trigger menu and initial performance assessment of the ATLAS trigger using Run-2 data,” ATL-DAQ-PUB-2016-001 (2016).
- [91] ATLAS Collaboration, “Trigger Menu in 2016,” ATL-DAQ-PUB-2017-001 (2017).
- [92] ATLAS Collaboration, “Trigger Menu in 2017,” ATL-DAQ-PUB-2018-002 (2018).

- [93] J. Alwall, R. Frederix, S. Frixione, V. Hirschi, F. Maltoni, O. Mattelaer, H. S. Shao, T. Stelzer, P. Torrielli, and M. Zaro, *JHEP* **07**, 079 (2014), arXiv:1405.0301 [hep-ph].
- [94] T. Sjostrand, S. Mrenna, and P. Z. Skands, *Comput. Phys. Commun.* **178**, 852 (2008), arXiv:0710.3820 [hep-ph].
- [95] P. Z. Skands, *Phys. Rev.* **D82**, 074018 (2010), arXiv:1005.3457 [hep-ph].
- [96] A. Alloul, N. D. Christensen, C. Degrande, C. Duhr, and B. Fuks, *Comput. Phys. Commun.* **185**, 2250 (2014), arXiv:1310.1921 [hep-ph].
- [97] C. Degrande, F. Maltoni, J. Wang, and C. Zhang, *Phys. Rev.* **D91**, 034024 (2015), arXiv:1412.5594 [hep-ph].
- [98] G. Durieux, F. Maltoni, and C. Zhang, *Phys. Rev.* **D91**, 074017 (2015), arXiv:1412.7166 [hep-ph].
- [99] M. Beneke, P. Falgari, S. Klein, and C. Schwinn, *Nucl. Phys. B* **855**, 695 (2012), arXiv:1109.1536 [hep-ph].
- [100] M. Cacciari, M. Czakon, M. Mangano, A. Mitov, and P. Nason, *Phys. Lett. B* **710**, 612 (2012), arXiv:1111.5869 [hep-ph].
- [101] P. Bärnreuther, M. Czakon, and A. Mitov, *Phys. Rev. Lett.* **109**, 132001 (2012), arXiv:1204.5201 [hep-ph].
- [102] M. Czakon and A. Mitov, *JHEP* **12**, 054 (2012), arXiv:1207.0236 [hep-ph].
- [103] M. Czakon and A. Mitov, *JHEP* **01**, 080 (2013), arXiv:1210.6832 [hep-ph].
- [104] M. Czakon, P. Fiedler, and A. Mitov, *Phys. Rev. Lett.* **110**, 252004 (2013), arXiv:1303.6254 [hep-ph].
- [105] M. Czakon and A. Mitov, *Comput. Phys. Commun.* **185**, 2930 (2014), arXiv:1112.5675 [hep-ph].
- [106] M. Botje *et al.*, (2011), arXiv:1101.0538 [hep-ph].
- [107] A. D. Martin, W. J. Stirling, R. S. Thorne, and G. Watt, *Eur. Phys. J. C* **63**, 189 (2009), arXiv:0901.0002 [hep-ph].
- [108] A. D. Martin, W. Stirling, R. Thorne, and G. Watt, *Eur. Phys. J. C* **64**, 653 (2009), arXiv:0905.3531 [hep-ph].
- [109] H.-L. Lai, M. Guzzi, J. Huston, Z. Li, P. M. Nadolsky, *et al.*, *Phys. Rev.* **D82**, 074024 (2010), arXiv:1007.2241 [hep-ph].
- [110] J. Gao, M. Guzzi, J. Huston, H.-L. Lai, Z. Li, *et al.*, *Phys. Rev. D* **89**, 033009 (2014), arXiv:1302.6246 [hep-ph].
- [111] R. D. Ball *et al.*, *Nucl. Phys. B* **867**, 244 (2013), arXiv:1207.1303 [hep-ph].
- [112] S. Frixione, P. Nason, and G. Ridolfi, *JHEP* **09**, 126 (2007), arXiv:0707.3088 [hep-ph].
- [113] P. Nason, *JHEP* **11**, 040 (2004), arXiv:hep-ph/0409146.
- [114] S. Frixione, P. Nason, and C. Oleari, *JHEP* **0711**, 070 (2007), arXiv:0709.2092 [hep-ph].
- [115] S. Alioli, P. Nason, C. Oleari, and E. Re, *JHEP* **06**, 043 (2010), arXiv:1002.2581 [hep-ph].
- [116] NNPDF Collaboration, R.D. Ball et al. (NNPDF), *JHEP* **04**, 040 (2015), arXiv:1410.8849 [hep-ph].

- [117] ATLAS Collaboration, “Studies on top-quark Monte Carlo modelling for Top2016,” ATL-PHYS-PUB-2016-020 (2016).
- [118] T. Sjöstrand, S. Ask, J. R. Christiansen, R. Corke, N. Desai, P. Ilten, S. Mrenna, S. Prestel, C. O. Rasmussen, and P. Z. Skands, *Comput. Phys. Commun.* **191**, 159 (2015), arXiv:1410.3012 [hep-ph].
- [119] ATLAS Collaboration, “ATLAS Pythia 8 tunes to 7 TeV data,” ATL-PHYS-PUB-2014-021 (2014).
- [120] D. J. Lange, *Nucl. Instrum. Meth. A* **462**, 152 (2001).
- [121] M. Bahr *et al.*, *Eur. Phys. J. C* **58**, 639 (2008), arXiv:0803.0883 [hep-ph].
- [122] J. Bellm *et al.*, *Eur. Phys. J. C* **76**, 196 (2016), arXiv:1512.01178 [hep-ph].
- [123] L. Harland-Lang, A. Martin, P. Motylinski, and R. Thorne, *Eur. Phys. J. C* **75**, 204 (2015), arXiv:1412.3989 [hep-ph].
- [124] E. Bothmann *et al.*, (2019), arXiv:1905.09127 [hep-ph].
- [125] S. Catani, F. Krauss, R. Kuhn, and B. R. Webber, *JHEP* **11**, 063 (2001), arXiv:hep-ph/0109231.
- [126] S. Höche, F. Krauss, S. Schumann, and F. Siegert, *JHEP* **05**, 053 (2009), arXiv:0903.1219 [hep-ph].
- [127] E. Re, *Eur. Phys. J. C* **71**, 1547 (2011), arXiv:1009.2450 [hep-ph].
- [128] S. Frixione, E. Laenen, P. Motylinski, B. R. Webber, and C. D. White, *JHEP* **07**, 029 (2008), arXiv:0805.3067 [hep-ph].
- [129] T. Gleisberg and S. Höche, *JHEP* **12**, 039 (2008), arXiv:0808.3674 [hep-ph].
- [130] S. Schumann and F. Krauss, *JHEP* **03**, 038 (2008), arXiv:0709.1027 [hep-ph].
- [131] S. Höche, F. Krauss, M. Schönherr, and F. Siegert, *JHEP* **09**, 049 (2012), arXiv:1111.1220 [hep-ph].
- [132] S. Höche, F. Krauss, M. Schönherr, and F. Siegert, *JHEP* **04**, 027 (2013), arXiv:1207.5030 [hep-ph].
- [133] F. Cascioli, P. Maierhofer, and S. Pozzorini, *Phys. Rev. Lett.* **108**, 111601 (2012), arXiv:1111.5206 [hep-ph].
- [134] A. Denner, S. Dittmaier, and L. Hofer, *Comput. Phys. Commun.* **212**, 220 (2017), arXiv:1604.06792 [hep-ph].
- [135] P. Nason and G. Zanderighi, *Eur. Phys. J. C* **74**, 2702 (2014), arXiv:1311.1365 [hep-ph].
- [136] ATLAS Collaboration, *JHEP* **09**, 145 (2014), arXiv:1406.3660 [hep-ex].
- [137] J. Pumplin, D. Stump, J. Huston, H. Lai, P. M. Nadolsky, *et al.*, *JHEP* **0207**, 012 (2002), arXiv:hep-ph/0201195 [hep-ph].
- [138] S. Alioli, P. Nason, C. Oleari, and E. Re, *JHEP* **07**, 060 (2008), arXiv:0805.4802 [hep-ph].
- [139] P. Golonka and Z. Was, *Eur. Phys. J. C* **45**, 97 (2006), arXiv:hep-ph/0506026.
- [140] N. Davidson, T. Przedzinski, and Z. Was, *Comput. Phys. Commun.* **199**, 86 (2016), arXiv:1011.0937 [hep-ph].
- [141] D. J. Lange, *Proceedings, 7th International Conference on B physics at hadron machines (BEAUTY 2000): Maagan, Israel, September 13–18, 2000*, *Nucl. Instrum. Meth. A* **462**, 152 (2001).

-
- [142] H. B. Hartanto, B. Jäger, L. Reina, and D. Wackerlo, *Phys. Rev. D* **91**, 094003 (2015), [arXiv:1501.04498 \[hep-ph\]](https://arxiv.org/abs/1501.04498) .
 - [143] A. D. Bukin, “Fitting function for asymmetric peaks,” (2007), [arXiv:0711.4449 \[physics.data-an\]](https://arxiv.org/abs/0711.4449) .
 - [144] J. Friedman, “Stochastic gradient boosting,” (2002), 367 pp.
 - [145] A. Hoecker *et al.*, “TMVA - Toolkit for Multivariate Data Analysis,” (2007), [arXiv:physics/0703039 \[physics.data-an\]](https://arxiv.org/abs/physics/0703039) .
 - [146] ATLAS Collaboration, *Eur. Phys. J. C* **74**, 3071 (2014), [arXiv:1407.5063 \[hep-ex\]](https://arxiv.org/abs/1407.5063) .
 - [147] ATLAS Collaboration, *Phys. Rev. D* **96**, 072002 (2017), [arXiv:1703.09665 \[hep-ex\]](https://arxiv.org/abs/1703.09665) .
 - [148] ATLAS Collaboration, “Calibration of the performance of b -tagging for c and light-flavour jets in the 2012 ATLAS data,” ATLAS-CONF-2014-046 (2014).
 - [149] ATLAS Collaboration, “Calibration of b -tagging using dileptonic top pair events in a combinatorial likelihood approach with the ATLAS experiment,” ATLAS-CONF-2014-004 (2014).
 - [150] ATLAS Collaboration, *Eur. Phys. J. C* **79**, 535 (2019), [arXiv:1902.05759 \[hep-ex\]](https://arxiv.org/abs/1902.05759) .
 - [151] ATLAS Collaboration, *Eur. Phys. J. C* **76**, 653 (2016), [arXiv:1608.03953 \[hep-ex\]](https://arxiv.org/abs/1608.03953) .
 - [152] “Trex fitter,” <https://twiki.cern.ch/twiki/bin/viewauth/AtlasProtected/TtHFitter>.
 - [153] W. Verkerke and D. P. Kirkby, eConf **C0303241**, MOLT007 (2003), [arXiv:physics/0306116 \[physics\]](https://arxiv.org/abs/physics/0306116) .
 - [154] L. Moneta, K. Belasco, K. S. Cranmer, S. Kreiss, A. Lazzaro, *et al.*, PoS **ACAT2010**, 057 (2010), [arXiv:1009.1003 \[physics.data-an\]](https://arxiv.org/abs/1009.1003) .
 - [155] ATLAS Collaboration, (2020), [arXiv:2002.07546 \[hep-ex\]](https://arxiv.org/abs/2002.07546) .